The bioreduction and biorecovery of critical metals by *Geobacter sulfurreducens*

A thesis submitted to the University of Manchester for the degree of Doctor of Philosophy in the Faculty of Science and Engineering

2022

Jinxin Xie

School of Natural Sciences

Department of Earth and Environmental Sciences

Content

List of Figures

List of Tables

COVID-19 Impact Statement

My PhD program started in 07/2018 and planned to finish by the end of 07/2021. However, because COVID-19 cased a national lockdown, our labs were closed from 03/2020 to 09/2020 which seriously affected my PhD program. At that moment, I had nearly finished my first Ce experiments and was waiting for the characterisation of the Ce bioreduction products. During the national lockdown, I could only do data analysis of my Ce experiments and work on a literature review of Sb and PGM projects from China. After the labs reopened, the new laboratory arrangements and management policies also seriously influenced my projects. I could not have access to the lab outside restrictive core hours or conduct long-term monitoring experiments, as I did before the lockdown. In addition, due to the requirements of the government's quarantine policy, the uses of equipment were also limited (such as XRD, ICP-MS,TEM and XPS), and it usually took us several times longer to apply for equipment and wait for test results than before the lockdown. The most serious concerns to external services included restricted access to XAS facilities. Since the release of national lockdown, we have submitted two applications for the Ce and Sb experiments which were rejected by the Diamond Light Source due to heavy backlogs. As the application period is every six months, it proved impossible for me to apply for XAS successfully during my PhD study. The unpredictable outbreak of COVID-19 has resulted in the delay of my entire PhD process but I have overcome most of the difficulties and reached here.

List of Abbreviations

AST	Accelerated stress test
BE	Binding energy
CB	Carbon black
CEC	Council of European Communities
CV	Cyclic voltammetry
DEES	Department of Earth and Environmental Sciences
DMRB	dissimilatory metal-reducing bacteria
ECSA	Electrochemical surface area
EDS	Energy Dispersive X-ray Spectroscopy
EXAFS	Extended X-ray Absorption Fine-Structure
HAADF	High angle annular dark field
ICDD	International Centre for Diffraction Data
ICP-AES	Inductively-Coupled Plasma Atomic-Emission Spectroscopy
ICP-MS	Inductively coupled plasma mass spectrometry
LBTs	lanthanide-binding tags
LSV	Linear sweep voltammetry
MIIT	Ministry of Industry and Information Technology
NBAF	Nutrient Broth Acetate-Fumarate
OD_{600}	Optical Density at 600nm
Oh	Octahedral coordination (subscripted)
ORR	Oxygen reduction reaction
PGM	Platinum group metal
ppb	Parts per billion
ppm	Parts per million
REE	rare earth element
SEM	Scanning Electron Microscopy
SHE	Standard hydrogen electrode
STEM	Scanning Transmission Electron Microscopy
Td	Tetrahedral coordination
TEM	Transmission Electron Microscopy
USEPA	United State Environmental Protection Agency
XANES	X-ray Absorption Near-Edge Structure
XAS	X-ray absorption spectrum
XMCD	X-ray magnetic circular dichroism
XPS	X-ray photoelectron spectroscopy
XRD	X-ray Diffraction

Abstract

Much attention has been focused on the influence of biogeochemical processes on the fate of metals and metallic minerals in the environment, and potential use of microorganisms to reduce and recovery critical metals from wastes. This thesis presents research into the bioreduction processes of Ce bearing ferrihydrite and Sb adsorbed ferrihydrite by the dissimilatory metal-reducing bacterium *Geobacter sulfurreducens*. The characterization of post reduction solid materials were performed by XRD, XPS, XMCD, XAS and TEM. Low contents of Ce and Sb had a neglectable impact on the bioreduction of ferrihydrite to biomagnetite. With increasing contents of Ce and Sb, the proportion of magnetite in secondary formed Fe minerals gradually decreased (and was not detected at 2% Ce/Sb or above), while goethite, an intermediate product of the bioreduction of ferrihydrite, became the primary Fe mineral type detected. During Fe(III) bioreduction process, no Ce or Sb was released, suggesting the fixation of Ce and Sb by Fe minerals during biological redox cycling in the natural environment. Applications of the biominerals formed were also explored, and the 0.5% Ce bearing magnetite nanoparticles were incorporated into carbon black supported Pt catalysts, which improved the duration of the catalyst, and can therefore reduce the use of platinum in this application. Finally experiments were also conducted which quantified the feasibility of using *Geobacter sulfurreducens* for PGM reduction and nanoparticle formation. Soluble Pd(II), Pt(IV), Rh(III) and Ru(III), and also mixes of Pd(II)-Pt(IV), Pd(II)-Rh(III) and Pd(II)-Ru(III), were all tested to determine if zero valent metallic nanoparticles could be formed. Nano-scale Pd(0), Pt(0) and Rh(0) particles were formed via bioreduction, but Ru(III) was not reduced, but still precipitated on the surface of bacterial cells. The sizes, morphology, distributions and crystal structures of nanoparticles were all characterised using a range of imaging and spectroscopy techniques. The location of most of the PGM nanoparticles was on the surface of *G. sulfurreducens* and sizes ranged from 2.6-3.8nm. Compared to the monometallic PGMs, the size of the bimetallic PdPt and PdRh alloys was smaller and were also more evenly distributed on the surface of the cell. Monometallic Pd(0) and bimetallic PdPt alloy nanoparticles showed the highest catalytic performances for the reduction of 4-NP, which were 3-30 times better than other nanoparticles. These results in this studies highlight the abilities of *G. sulfurreducens* to bioreduce and biorecover a wide range of metal and metalloid nanoparticles, often making potentially useful functional nanomaterials as end products.

Declaration

No portion of the work referred to in the thesis has been submitted in support of an application for another degree or qualification of this or any other university or other institute of learning.

Copy right statement

i. The author of this thesis (including any appendices and/or schedules to this thesis) owns certain copyright or related rights in it (the "Copyright") and s/he has given The University of Manchester certain rights to use such Copyright, including for administrative purposes

ii. Copies of this thesis, either in full or in extracts and whether in hard or electronic copy, may be made only in accordance with the Copyright, Designs and Patents Act 1988 (as amended) and regulations issued under it or, where appropriate, in accordance with licensing agreements which the University has from time to time. This page must form part of any such copies made.

iii. The ownership of certain Copyright, patents, designs, trademarks and other intellectual property (the "Intellectual Property") and any reproductions of copyright works in the thesis, for example graphs and tables ("Reproductions"), which may be described in this thesis, may not be owned by the author and may be owned by third parties. Such Intellectual Property and Reproductions cannot and must not be made available for use without the prior written permission of the owner(s) of the relevant Intellectual Property and/or Reproductions.

iv. Further information on the conditions under which disclosure, publication and commercialisation of this thesis, the Copyright and any Intellectual Property and/or Reproductions described in it may take place is available in the University IP Policy (see http://documents.manchester.ac.uk/DocuInfo.aspx?DocID=24420), in any relevant Thesis restriction declarations deposited in the University Library, The University Library's regulations (see http://www.library.manchester.ac.uk/about/regulations/)andin The University's policy on Presentation of Theses

Acknowledgements

At first, I would like to thank my academic supervisors Jon Lloyd, Vicky Coker and Brian O'Driscoll. They developed my interest in scientific research and helped me throughout, giving me suggestions and supporting me to complete my PhD project.

I would like to thank to Dr. Sul Mulroy who taught me how to conduct standardized experiments when I first started my doctoral experiment and gave me a lot of advice for my first experiment.

I would like to thank to everyone who help me with my PhD project, especially: Dr. John Waters who help me with XRD analysis for hundreds samples, Dr Abby Ragazzon-Smith and Mr Paul R. Lythgoe who help me to run ICP-MS and ICP-AES samples. I also would like to thank to Dr. Ben F. Spencer for his help with XPS analysis, Dr. Rongsheng Cai and Christopher Egan Morriss for TEM analysis.

I would like to thank to everyone in the geomicrobiology group at the University of Manchester. Everyone is very kind and helpful to me in the past four years. I'm so proud to be one of the geomicrobiology group.

I am very grateful to my friends in UK for their company in daily life which makes

my life interesting and unforgettable, especially Yunhao Sun, Jianuo Chen, MIngxue Wei, Dongxu Chen, Zhaoqi Ji, and Kejing Zhang.

I am especially grateful to my families. Their continuous support and understanding have been the cornerstone of my doctoral study. I love you all, my grandparents, my parents, my sister and brother-in-law. I have to thank my grandmother in particular. I was brought up by my grandparents, who have always loved me and supported me with all their strength. My grandmother passed away in my first year of PhD, and I'm sorry I wasn't with her in her final moments. So I would like to dedicate this thesis to my grandma. I hope she can always be proud of me!

About the Author

The author graduated from the Suzhou University of Science and Technology with a bachelor's degree in Environmental Engineering in 2016 and a MSc degree from the University of Manchester in Pollution and Environmental Control in 2017. Before starting his PhD in 2018, he worked as a teaching assistant at Suzhou University of Science and Technology for six months.

Chapter 1: Introduction and Thesis Structure

1.1 Project context and research aims

Environmental pollution has been an important issue for decades, and addressing heavy metal contamination of soil and water is one of the most serious challenges in environmental science (Hu et al., 2014; Priya et al., 2014; Yang et al., 2016). Metal or metalloid-bearing wastes can be roughly divided into two categories; those from natural sources and those from anthropogenic activities. Comparing these two categories, anthropogenic activities are generally considered as the more significant in terms of levels of pollution (Gadd, 2010). With the rapid development of industrialisation and urbanisation, anthropogenic activities discharge large amounts of waste containing metal ions into the environment every year; these activities include mining, metallurgical operations and cement production (Nancharaiah et al., 2016). Metal contamination has become a serious environmental issue for the following reasons. First, compared with some organic pollutants that can be broken down into harmless substances, metal contaminants are not biodegradable (Priya et al., 2014). Second, metal and some metalloid contaminants can have a negative influence on the health of human populations and associated ecosystems. Elements with significant biological toxicity include the metalloids antimony and arsenic, as toxic heavy metals such as zinc, cadmium, mercury, copper, cobalt and nickel (Schmitt et al., 2007; Ternjej et al., 2013; Yi and Hai, 2005). The latter pollutants can negatively

impact human health by increasing the rates of cancers and the cause of specific sicknesses such as Minamata disease (Hg) and arsenic poisoning (As). Through the growth of the plants in contaminated land, metal contaminants in the soil and water can be accumulated in high concentrations and can then enter the food chain, becoming a significant hazard to all human populations (Lu et al., 2012; Pergent and Pergent-Martini, 1999).

Although metal and metalloid pollution has become a serious environmental problem worldwide, some critical and scarce metals are precious resources which are important raw materials for the production of high technology products. These metals and metalloids include gold, antimony, platinum group metals (PGM) and rare earth elements (REE). The supply risk can hinder economic development and thus affect the quality of life in societies (Commission, 2020; ENTR, 2014). Valuable metal and metalloid resources are currently decreasing in availability because of the heavy demands of rapidly expanding “E-tech” production processes. In addition, another reason for the supply risk in most countries is the uneven distribution of most metal and metalloid minerals. Some mineral-rich countries still face shortages of some metal and metalloid minerals (Girtan et al., 2021). Figure 1.1 shows the criticality assessment results of raw materials from European Commission (2020). Thirty materials have been identified as critical, and metals and metalloid elements dominate this number. The supply risk of REEs are highest

in all of the critical material, while antimony and the PGM also have high value and high levels of supply risk.

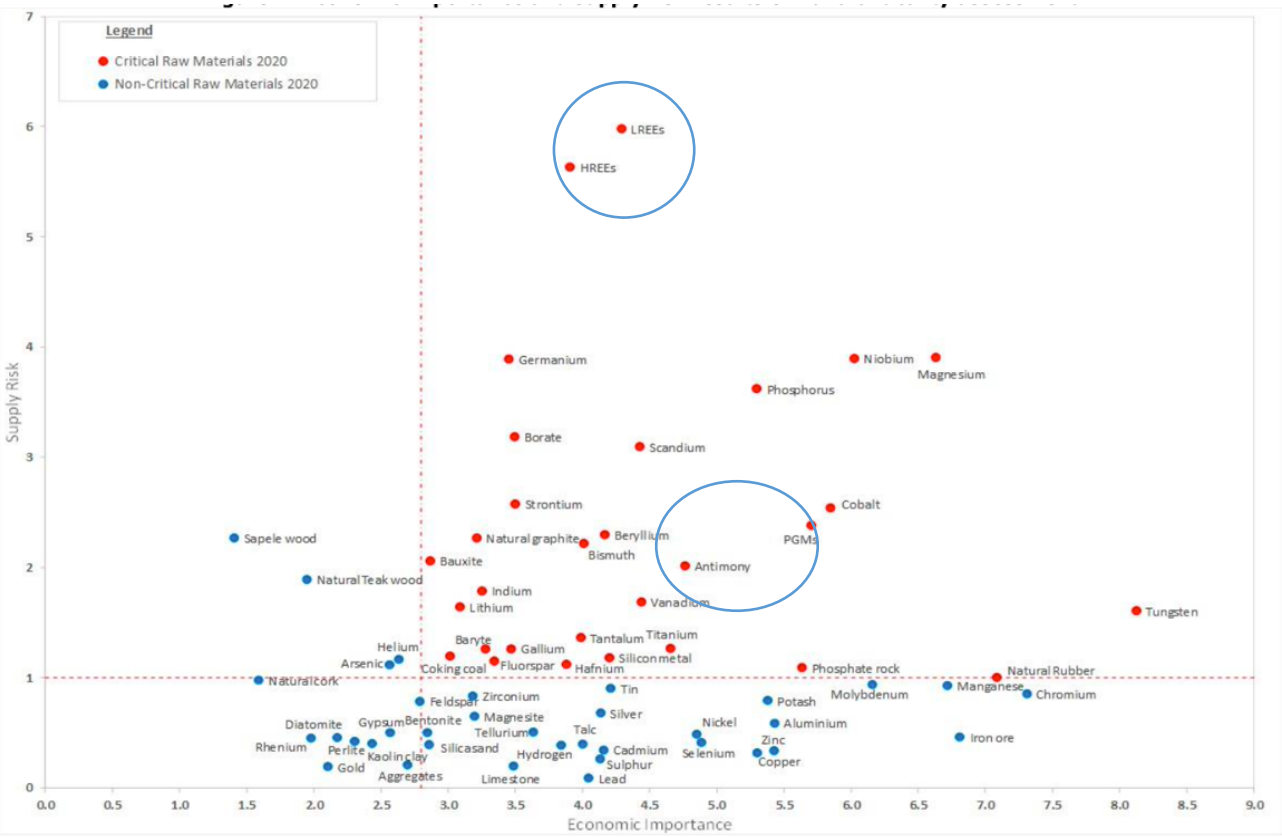

Figure 1.1 Economic importance and supply risk results of 2020 criticality assessment (EU, 2020)

Microbial activities can influence the valance state of some metal ions, affecting the mobility and availability of metal ions in the natural environment (Alvarez and Illman, 2005). For these reasons, the bioreduction and biorecovery of valuable metals from metal and metalloid contaminated wastes is an emerging and important research topic for promoting sustainable development, environmental protection and optimal resource utilisation within the “circular economy”(Işıldar et al., 2017).

The aims of the research in this thesis are focused on the following points:

1. To research the interaction between Fe(III) mineral bioreduction and cerium (or antimony) materials in the experimental systems
2. To test if microbiological systems (using *Geobacter sulfurreducens* biological reduction experiments in an anaerobic water system) can be used in the bioremediation and bio-recovery of waste metals and metalloids.
3. To investigate the range of applications of any recovered metallic nanoparticles, including as fuel cell catalysts and the catalytic conversion of organic substrates (remediation and fine chemical synthesis).

1.2 Thesis structure

This research thesis consists of 7 chapters, as follows:

Chapter 1 Introduction: this chapter sets out the project context, research aims, thesis structure and author contributions of this research thesis.

Chapter 2 Literature review: this chapter presents the scientific background knowledge including the exploitation and output situation of target e-tech metals and metalloids (Au, Ce, Sb and the PGM), potential environmental problems associated with these elements, existing bio-recovery and bioreduction technologies for these e-tech elements, as well as general information for

Geobacter sulfurreducens and the bioreduction and bioremediation cases of *Geobacter sulfurreducens.*

Chapter 3 Methodology: detailed information of experimental arrangements and procedures, and detailed principle of instrument are provided in this chapter.

Chapter 4 Research Chapter One: a manuscript titled ”Bioreduction of cerium-bearing ferrihydrite; a new route to carbon-black supported platinum catalysts” is presented in this chapter. *Geobacter sulfurreducens* was incubated and used to reduce synthesized Ce-bearing ferrihydrite. The solubility of Ce and Fe was monitored by ICP-AES and Ferrozine assay. XRD and XMCD were used to identify the end-point bioreduction products. The morphology, size and distribution of the bioreduction products was detected by TEM. The formed biomagnetite doped with 0.5% Ce was added into electrodes as catalysts to achieve better durability.

Chapter 5 Research Chapter Two: this chapter presents a manuscript entitled “Microbial reduction of antimony(V)-bearing ferrihydrite by *Geobacter sulfurreducens*”. This study focuses on the bioreduction of Sb(V)-adsorbed ferrihydrite by *Geobacter sulfurreducens.* The fate of Sb during the bioreduction process was investigated by XPS. The inhibitory effect of Sb on the biotransformation of Fe minerals was also researched, and the secondary Fe

minerals formed were analysed by XRD and TEM in this study.

Chapter 6 Research Chapter Three: “The bioreduction of Platinum group metals (PGM) by *Geobacter sulfurreducens* and the application for catalytic reduction of 4-nitrophenol”. This study focuses on biological recovery experiments of PGM using direct enzymatic reduction by *Geobacter sulfurreducens* in anaerobic system. The PGM nanoparticles generated were characterised by both XRD and XPS. Morphology and spatial distribution information for the PGM nanoparticles was elucidated by TEM and is also included in this chapter. The catalytic performance of PGM nanoparticles was evaluated through the reduction of 4-NP by $NaBH_4$.

Chapter 7: Conclusion and future work: the main findings of all of the above chapters are synthesised in this chapter. The possibilities for future research directions associated with these three projects are also discussed here.

1.3 Author contributions to primary research-focused chapters (4, 5, 6)

Chapter 4: Bioreduction of cerium-bearing ferrihydrite; a new route to carbon-black supported platinum catalysts

Jinxin Xie: principal author, experiments design, experiments works and data analysis

ZiYu Zhao: catalysts experiments works and relevant data analysis

Victoria S. Coker: supervisor, concept development and manuscript review

Brian O'Driscoll: supervisor, concept development and manuscript review

Rongsheng Cai: TEM data collection and relevant data analysis

Jonathan R. Lloyd*: principal supervisor, concept development and manuscript review

Chapter 5: Microbial reduction of antimony(V)-bearing ferrihydrite by *Geobacter sulfurreducens*

Jinxin Xie: principal author, experiments design, experiments works and data analysis

Victoria S. Coker: supervisor, concept development and manuscript review

Brian O'Driscoll: supervisor, concept development and manuscript review

Rongsheng Cai: TEM data collection and relevant data analysis

Jonathan R. Lloyd*: principal supervisor, concept development and manuscript review

Chapter 6: The bioreduction of Platinum group metals(PGMs) by *Geobacter sulfurreducens* and the application for catalytic reduction of 4-nitrophenol

Jinxin Xie: principal author, experiments design, experiments works and data analysis

Victoria S. Coker: supervisor, concept development and manuscript review

Brian O'Driscoll: supervisor, concept development and manuscript review

Christopher Egan Morriss: TEM data collection, catalyst experiments works and relevant data analysis

Jonathan R. Lloyd*: principal supervisor, concept development and manuscript review

Chapter 2: Literature review

2.1 Introduction to target e-tech metals; REE, Sb , Au and PGM

2.1.1 Rare earth elements (REE)

Rare earth elements (REE) include the lanthanides (atomic number 57-71), yttrium (Y 39), and scandium (Sc 21). Depending on their atomic weight, they can be divided into the light rare earth elements (around 57-64) and heavy rare earth elements (65-71) (Brisson et al., 2016; Fernandez, 2017; Liu, 2016). Table 2.1 summarises the crustal concentrations, resources and production tonnage of the REE (Haque et al., 2014). The REE are widely used in modern industrial manufacturing, in products such as magnets, battery alloys, fluid cracking catalysts, ceramics and glass additives. Compared with the other REE, cerium and lanthanum are used more widely in the aforementioned industries. Although the REE are very important industrial elements, the reserve abundance is not abundant and the relative distributions of REE resources are uneven in different countries. According to the reviews of Goodenough et al. (2016), Fernandez (2017) and US Geological Service (USGS), REE reserves worldwide are estimated to be around 130 million tons, with China, Vietnam and Brazil hosting the highest shares at around 37%, 18% and 18%, respectively, followed by Russia, India, Australia, Greenland and the USA (around 10%, 6%, 3%, 1% and 1%, respectively) (Fernandez, 2017; Ferreira and Critelli, 2022; Goodenough et al., 2016; USGS, 2020). In the REE global market, at least 85% of REE are produced by China (Paulick and Machacek,

2017), but in recent years, the REE supply risk has increased because the Chinese government has reduced the export quotas of the REE and cracked down on illegal REE mining in China.

Table 2.1 Natural (bulk) crustal concentrations, resources and production tonnage for the REE (adapted from (Haque et al., 2014).

Elements	Crustal Abundance in ppm	Resources tonnes	Production tonnes/annum
Lanthanum (La)	32	22600000	12500
Cerium (Ce)	68	31700000	24000
Praseodymium (Pr)	9.5	4,800,000	2400
Neodymium (Nd)	38	16700000	7300
Promethium (Pm)	--	--	--
Samarium (Sm)	7.9	2900000	700
Europium (Eu)	2.1	244333	400
Gadolinium (Gd)	7.7	3622143	400
Terbium (Tb)	1.1	566104	10
Dysprosium (Dy)	6	2980000	100
Holmium (Hm)	1.4	--	10
Erbium (Er)	3.8	1850000	500
Thulium (Th)	0.48	334255	50
Ytterbium (Yt)	3.3	1900000	50
Lutetium (Lu)	--	395000	--

Yttrium (Y)	30	9000000	8900
Scandium (Sc)	22	--	0.4-1.6

Ore deposits of the REE may be associated with uranium/thorium mineralization, so the extraction processes for the REE may lead to pollution of the environment by radioactive elements (Hurst, 2010; Liu, 2016). In addition, according to the research of Hayes-Labruto et al. (2013), during the production of one tonne of REE, around 60000 m^3 waste gases (including HCl), 200 m^3 acidic waste waters and around 1 ton of radioactive wastes may potentially be generated (Hayes-Labruto et al., 2013). Thus, Liu (2016) highlights the paradox that some REE products are being used to build a clean, smart, low-carbon and climate-resilient future while simultaneously causing environmental damage. For example, in China, REE mining has caused serious water pollution in the Pearl River Basin, severely affecting local agriculture and fisheries. Moreover, in Baotou City which hosts large REE reserves, cancer cases have been reported in local villages, attributed to buried toxic (radioactive) mining wastes (Liu et al., 2016).

Although mining of the REE can motivate economic growth in a short time, the cost of remediating the contaminated area can be very high. According to reports of Ministry of Industry and Information Technology of People's Republic China (MIIT) for Ganzhou City (which only accounts for around 8.6% of China's total REE quota), the costs to clean up the polluted REE mines through existing

technologies will be around RMB 38 billion (around £4.3 billion; MIIT, 2012; in Liu et al., 2016). Due to these factors, bioremediation technologies (such as bio-adsorption and bio-accumulation) for REE-contamination could substantially reduce the economic pressures exerted by the need for pollution treatment.

2.1.2 Antimony

Antimony (Sb) is located in group 15 of the Periodic Table, close to arsenic (As), so previous research has considered that these two elements have relatively similar characteristics (Filella et al., 2002a; Filella et al., 2002b; Filella et al., 2007; Li et al., 2016; Terry et al., 2015). Antimony (Sb) is a metalloid element used widely in the production of flame retardants, textiles, papers, adhesives, tires, brake linings and plastics (Wang et al., 2013). Similar to many other metals and metalloids, the main source of antimony is mining (Li et al., 2016) and according to data published in 2017, the global reserves of antimony total around 1300000 tons. China, Bolivia, Mexico, Russia, South Africa, and Tajikistan are the major owners of these antimony sources. However, nearly 90% of Sb is supplied by China (Anderson, 2019). Although Sb is distributed widely in water and soils, the concentrations of antimony are low (normally less than 1 μg/L) under natural conditions. However, high concentrations of free antimony ions discharged by human activities can be harmful to the environment and human health (Filella et al., 2002a). Similar to arsenic, antimony is not an

essential element for life (Flower and Goering, 1991). Its bioavailability and toxicity depends on its chemical form and oxidation state: with the toxicity of Sb(III)> Sb(V) > organoantimonials (Cao et al., 2020; Gebel, 1997; Wilson et al., 2010).

Organic and inorganic Sb are both found in soil systems, but Sb(III) and Sb(IV) are more common (Du et al., 2020; Filella et al., 2002a; Ilgen et al., 2014). The solubility and speciation of Sb are affected by soil pH, organic matter contents and soil mineralogy (Guo et al., 2014; Pierart et al., 2015; Wilson et al., 2010). It is easy for plants to take up the Sb from the soil, although Sb is not an essential element for plant growth, potentially leading to an bioaccumulation of Sb in plant material (Feng et al., 2013; He et al., 2012). The bioaccumulation of Sb in edible plants may lead to Sb entering the food chain, which in turn can result in the enrichment of antimony in the bodies of animals and humans (Pierart et al., 2015). Long-term exposure to high Sb levels can cause health problems which are similar to the impacts of arsenic; for instance, free Sb ions can cause lesions on the lungs and heart (Terry et al., 2015). Aside from the bioaccumulation of Sb in plants, animals and humans, the distribution and enrichment of Sb can also be controlled by microorganisms in the environment, usually associated with biological redox processes(Li et al., 2016).

With rapid industrialisation, the environmental impacts of antimony pollution

have attracted increasing attention around the world. Antimony and its compounds are now considered as pollutants by the US Environmental Protection Agency (USEPA) and the Council of European Communities (CEC). In addition, according to the CEC, Chinese standards of surface water and USEPA, the maximum concentration of Sb allowed in drinking water is 5-6 μg/L (EU, 1998; Li et al., 2016; Rakshit et al., 2011; Terry et al., 2015; USEPA, 1999; Yousefi et al., 2010). Due to the overexploitation of antimony during mining in the southwest of China, Sb contamination has led to serious environmental issues. According to the report of Li et al. (2016), the Sb concentrations in water, sediment and soil in the contaminated areas are around 29.4 mg/L, 1163 mg/kg and 2 mg/kg, respectively, seriously exceeding the allowable limits (1μg/L, 0.800 - 3.00 mg/ kg and 0.57 mg/ kg, respectively). The biogeochemistry of arsenic, including redox transformations between As (III) and As (V), have been well researched. Because of its similar chemical character to As, redox cycling of antimony by bacteria is possible, but the relevant literature is still limited so this process remains comparatively poorly understood.

2.1.3 Gold (Au)

Since ancient times, gold has been considered a high value commodity used in both jewellery and as currency. Until now, around 50% of gold production has been associated with the jewellery sector, but is presently used increasingly more in “the industrial age”, in different fields, including electronics, photonics,

catalysis and sensing (Sathishkumar et al., 2010). The average concentration of gold in the Earth's crust is very low, but demand continues to increase (Bosch and Pradkhan, 2015; Rana et al., 2020; Zhu et al., 2016). In order to meet this demand, new gold mines are continually being discovered and mined. However, both large- and small-scale gold mines can discharge significant quantities of toxic materials into local water bodies and soils during mining processes, including mercury, cyanide and arsenic (Akpalu and Normanyo, 2017). Thus, gold recycling is also attracting increasing attention in order to minimise the release of these primary contaminants to the environment. Many wastes, such as industrial leachates, eluates from activated carbon and e-wastes, often contain appreciable gold concentrations. However, traditional gold recovery methods are high-cost and not eco-friendly, so it is essential to find economic and clean methods to recovery gold from the waste (Deplanche and Macaskie, 2008; Wang et al., 2022).

2.1.4 Platinum group metals (PGM)

The platinum group elements (PGE) include platinum (Pt), palladium (Pd), rhodium (Rh), ruthenium (Ru), iridium (Ir) and osmium (Os) (O'Driscoll et al., 2018; Rao and Reddi, 2000; Todand et al., 1995). The economic value of the platinum group metals is very high because platinum group metals are used widely in a wide range of industries, in products such as chemical process catalysts, vehicle catalysts, hydrogen fuel cells, electronic components,

jewellery and as investments. However, the resources and reserves are very limited, so PGM prices are very high (Brenan, 2008; Hughes et al., 2021; Jackson et al., 2007; Kettler, 2003; Ravindra et al., 2004; Vermaak; Xiao and Laplante, 2004).

Most of the PGM are siderophile and chalcophile elements found naturally in mineralised magmatic rocks (O'Driscoll and González-Jiménez, 2016). The elements contained in PGE ores are often reported as '4E' (Pt+Pd+Rh+Au) or '6E' (Pt+Pd+Rh+Ru+Ir+Au) grades (Mudd, 2012; Mudd et al., 2018). South Africa hosts the largest reserves and dominates global PGM production every year (more than 50%) because of their huge resources in the Proterozoic Bushveld Complex, followed by the Palaeozoic Norilsk–Talnakh field in Russia, and other mines in Canada, Zimbabwe and the United States (Mpinga et al., 2015; Mudd, 2012; Mudd et al., 2018; O'Driscoll and González-Jiménez, 2016; Sahu et al., 2021). However, the distribution of PGM ores are very uneven around the world and demand will keep growing for many years due to the global population growth and continued consumption of resources (Reuter et al., 2013). As a result, the supply risk of the PGM keeps increasing and they have been identified as a critical material in many countries (Graedel et al., 2012; Mudd et al., 2018). For example, PGM have been listed as critical raw material in the criticality assessment of the European Commission from 2010 to 2020 (EU 2020). In addition, China is rich in some mineral resources, such

as the REE and antimony, but in terms of the PGM, China's reserves (only around 350 tons) and quality of PGM natural resource deposits are not generous. In China, the Jinchuan Group Company produce 2.5-3 tons PGM every year, accounting for around 90% of total Chinese production. However, total demand for Pt and Pd alone were around 137 tons in 2012, so China imports most of PGM from abroad yearly (Dong et al., 2015).

Certain wasteforms potentially represent PGM-rich resources such as mining leachates (Pd/Pt contained wastewater), mining solid residues, e-waste, anode mud and spent catalyst. When PGM-bearing wastes enter the environment, they may accumulate in the soil and potentially enter the biological food chain, entering plants, animals and the human body (Cinti et al., 2002). In general, in areas close to roads, PGM mines and factories, PGM concentrations in the local environment is relatively high. According to Ek et al.'s research (2004), although the hazards associated with the PGM are not well understood (WHO, 1991), increased use of the PGM in catalysts might increase the risk of environmental and biological accumulation (Ek et al., 2004). On the basis of existing research, PGM ions can accumulate in organs such as the liver and kidney in the human body, and only Pt(II) is capable of combining to protein in human blood. In addition, Pt is a well-known allergen and according to the Environmental Health Criteria for palladium from WHO, Pd is a common allergen, while some Pd salts can cause severe primary skin and eye irritations

(Ek et al., 2004; Melber et al., 2002). Recovery of PGM from wasteforms might therefore not only decrease the potential risk of PGM accumulation in the environment, but may also relieve socioeconomic pressures from the relative scarcity of PGM resources. Compared with existing chemical recovery strategies for the PGM, biorecovery of PGM with microbial systems can potentially offer more environmental friendly route(s) to resource recovery (Karim and Ting, 2021).

2.2 Bioremediation and bio-recovery methods

According to Alvarez et al. (2005), bioremediation was identified as stimulating biological activity to remedy or eliminate contamination in a contaminated water body, aquifer, soil system or natural sediment (Alvarez and Illman, 2005). Plants and microorganisms are most often used in applications including the treatment of heavy metals, the biodegradation of organic pollutants and in ecological restoration. Biosorption, bioleaching and bio-recovery all are bioremediation treatment methods used during heavy metal treatment (Zhu et al., 2016). Compared with other physical and chemical treatment methods, bioremediation may offer cost savings as it can often be applied as an in situ treatment method and the operational costs can also be low (Bento et al., 2005; Kuppusamy et al., 2016). In addition, bioremediation can also offer eco-friendly treatment methods that target organic contaminants and degrade them completely to CO_2 or less toxic intermediates. Meanwhile, some metal and metalloid ions can also

be transformed and immobilised on within the cells or be incorporated into insoluble precipitates through bioremediation processes (Natarajan and Ting, 2015; Ohnuki et al., 2008; Zhu et al., 2016). Biologically-mediated redox transformations and biosorption reactions are key basic reaction principles for many bioremediation processes. However, a limitation of bioremediation approaches can be that they rely on particular environmental conditions, and if they are not suitable, the metabolic capacity of microbes can be weakened. As a consequence of the latter, bioremediation methods may not work well in extreme temperatures, or at high or low pH values), and can be sensitive to redox conditions, the bioavailability of contaminants and the presence of adequate levels of nitrogen, phosphorus, carbon and other nutrients (Alvarez and Illman, 2005; Megharaj et al., 2011; Sterner and Elser, 2017).

Due to many wasteforms containing valuable metals and metalloids, methods of recovery and recycling them has become a popular topic. Physical and chemical recovery approaches have been implemented, such as electrochemical, precipitation, adsorption, ion exchange and hydrometallurgical methods of processing e-wastes. However, although compared with other treatment methods such as pyrometallurgy, landfill, burning in incinerators or exporting to underdeveloped countries, these physical and chemical recovery methods are considered more eco-friendly, albeit still resulting in discharges of polluted water and non-inert waste solids to the environment to cause

secondary pollution (Anthony and Flett, 1994; Le and Lee, 2021; Tesfaye et al., 2017). In addition, most of the physical and chemical recovery methods are considered off site treatments. It is financially reasonable to deal with small volumes of e-waste in this context, but when large volumes of metal-contaminated soil etc need to be treated, the costs associated with off-site treatments are extremely high.

The biorecovery of metals can be considered as a bioremediation method. Compared to traditional physical and chemistry recovery methods, biorecovery of metals can be considered an environmentally-friendly alternative. Plants and microorganisms are both used in biorecovery methods. However, in a biological metal-recovery system, microorganisms are considered the most promising method of biorecovery, because uptake into the plant tissue from contaminated soil/water can be limited, and microorganisms show a stronger potential in bio-recovery systems (Deplanche and Macaskie, 2008). In addition, according to previous studies, many microbes show the ability to reduce soluble valuable metal ions via cellular electron transfer chains (Deplanche and Macaskie, 2008; Lloyd, 2003; Lovley et al., 1993). Furthermore, some microbes are capable of reducing metal ions to form nano-sized metal particles associated with the cell (Foulkes et al., 2016; Macaskie et al., 2010; Zhu et al., 2016) and these products of biorecovery can have directly applications such as in catalytic processes.

2.2.1 Biorecovery of REE

Research on bioremediation or biorecovery of REEs are still relatively limited. Most current research focuses on the distribution of the REEs in various environmental systems. According to the existing literature, bioremediation methods for the REEs mainly focus on biosorption and bioenrichment using microbes or plants(Andres et al., 2003; Giese, 2020). The results of the REEs biosorption for different microorganisms showed that the adsorption capacity of different bacteria varies greatly under different conditions (2 to 1000 μmol/g biomass). Important influencing factors were found to be pH value, variation in REEs ionic species and the nature of the microbial cell wall layers. In general, pH 5 is commonly used in biosorption experiments because it is below the pH value where REEs precipitate. In Andres et al.'s and Giese's reviews, they proposed that carboxylic, phosphate groups, amino, sulfhydryl and hydroxyl groups in the cell wall can combine with some REE cations (Andres et al., 2003; Giese, 2020).

Another study also identified the adsorption ability of rare earth elements by microorganism (Vijayaraghavan et al., 2010). In this study, the adsorption capacity of a marine algae (*Turbinaria conoides)*, for four REEs (La, Ce, Eu, Yb) was evaluated. Initially, the experiment was conducted with 4 samples, and different initial pH values (2-5) were tested. The results showed that pH played an important role in the biosorption process, and the initial pH at 5 is most

suitable for adsorption. At low pH, the concentrations of H^+ and other light metal positive ions in the solution were quite high, and they can bind to carboxyl groups while the REE ions were not be able to compete with H^+ and light metal ions. The adsorption experiment result proved that *Turbinaria conoides* can absorb more La than Ce, Eu, Yb because of the high ionic radius, low atomic mass, and low electronegativity of the former element. The order of removal is La > Ce > Eu > Yb (Vijayaraghavan et al., 2010). Ohnuki et al. (2015) conducted experiments to compare the sorption of Ce by synthetic Mn oxides and *Pseudomonas fluorescens* and analysed the oxidation mechanism of Ce(III) during this process. The results of the latter study showed that both Mn oxides and *Pseudomonas fluorescens* had the ability to sorb Ce ions in the environment. However, the oxidation of Ce(III) was mainly associated with Mn oxides rather than microorganisms. In contrast, Ce(III)-P bearing nano-particles on cell surfaces will inhibit the oxidation of Ce(III) to Ce(IV) (Ohnuki et al., 2015).

In another study, Park et al. (2016) used genetic engineering to overexpress lanthanide-binding tags (LBTs) in the S-layer of *Caulobacter crescent,* which does not have a strong adsorption capacity for the REE without LBTs (Park et al., 2016).

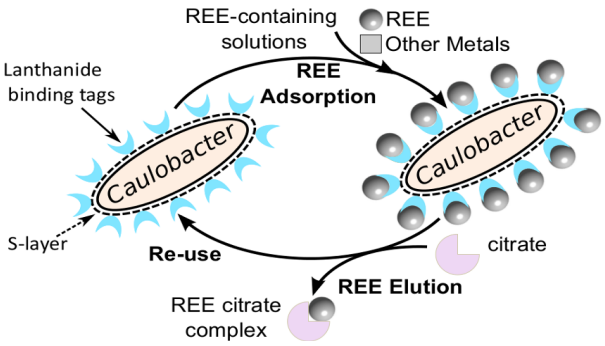

Figure 2.1 The bio-adsorption process of the lanthanide-binding tags (LBT)-displayed strains (Park et al., 2016)

Figure 2.1 presents the recovery process for the REE after binding of the REE ions to LBTs. Citric acid leaching was used to remove the adsorbed metal and recycle the REE, and the LBT-displayed strain could still be used to adsorb the REE after citric acid leaching. According to the experiment results, the adsorption efficiency of the LBT-displayed strain would be affected by some metal ions such as Ca^{2+} and Cu^{2+} (Park et al., 2016). In another research, LBTs were also engineered on the surface of *E coil* which indicated that engineered bacteria can adsorb more REEs than the wild *E. coil*, but the adsorption abilities are affected by pH and metals concentration (Chang et al., 2020). A summary based on the existing literature for REE bioimmobilization were present in table 2.2 which adapted from Nancharaiah et al. (2016). The information shown in Table 2.2 suggests that most research on bioremediation methods for REE has focused on biosorption processes.

Table 2.2 Microbe–Metal Interaction for Immobilization of REE (Nancharaiah et al., 2016)

Rare earth elements			
Metal	Organism	Metal source	bioremediation process
Dy	*Penidiella sp. T9*	$DyCl_3$	Bioaccumulation
	P. aeruginosa	$DyCl_3$	Biosorption
La	*Pseudomonas aeruginosa,Bacillus subtilis, Myxococcus xanthus,Myxococcus smegmatis, E. coli, Pseudomonas sp.*	$La(NO_3)_3$	Biosorption
Nd	*P. aeruginosa*	$NdCl_3$	Biosorption
Sc	*Saccharomyces cerevisiae, Rhizopus arrhizus, Aspergillus terreus*	$ScCl_3$	Biosorption
Eu	*P. aeruginosa, Myxococcus xanthus*	$EuCl_4$	Biosorption
Yb	*M. smegmatis*	$YbCl_5$	Biosorption

2.2.2 The bioremediation of antimony (Sb)

Sb is distributed widely in the water and soil system, but free antimony ions are harmful to the environment and human health. Antimony often exists in natural systems in four oxidation states (V, III, 0, -III), but Sb(III) and Sb(V) are the two more common forms in the natural environment, similar to the occurrence of As (Li et al., 2016; Li et al., 2018). Sb is a chalcophile element so often exists in sulfidic minerals (Dovick et al., 2015). In aqueous systems, antimony speciation depends on the pH and redox potential of the system (Figure 2.2). In neutral aqueous systems, under aerobic conditions, Sb often exists as pentavalent antimonate ($Sb(OH)^{6-}$), and in anaerobic systems, Sb often exists as uncharged

antimonous acid, $Sb(OH)_3$. In addition, compared with Sb(V), Sb(III) is much more mobile (Filella et al., 2002b; Wilson et al., 2010).

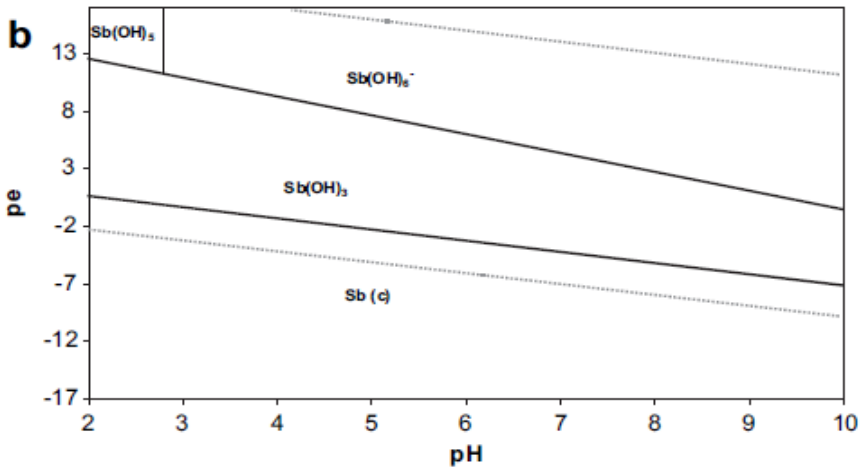

Figure 2.2 The influence of the pe and pH to the form of the Sb (0.1mM) in the system (Wilson et al., 2010)

Sb has similar chemical characteristics to those of As, and bioremediation of antimony through bacterial biological redox cycling is therefore considered possible. Bioreduction of antimonate and bio-oxidation of antimonite is discussed separately (below) and may be important for Sb bioremediation efforts.

The first organism that was shown to reduce Sb(V) was a marine alga, *Sargassum sp*. (Kantin, 1983). In the latter research, three kinds of marine algae (*Ulva sp., Enteromorpha sp., and Sargassum sp.*) were compared, but only *Sargassum sp.* contained ~30% Sb(III), indicating that this algal species is capable of reducing Sb(V) in seawater. According to previous research, Fe(II)-containing minerals can also reduce free Sb(V) ions to Sb(III) via chemical

redox reactions under anaerobic conditions (Li et al., 2016; Mitsunobu et al., 2008). In addition, Kulp et al. (2014) showed that Sb(III) could be absorbed strongly by the iron phase under reducing conditions (Kulp et al., 2014). Similarly, sulfate-reducing bacteria (SRB) have been used for antimony recovery (Wang et al., 2013). In the latter study, the SRB firstly reduce sulfate to sulfide, and then the sulfide formed would reduce the Sb(V), and then form stibnite (Sb_2S_3) in neutral or weakly alkaline solutions (Wang et al., 2013). Another study showed that *Rhizobium* can reduce Sb(V) using hydrogen as the sole electron donor, to precipitate Sb_2O_3 (Lai et al., 2016). In another study, a new strain of *Sinorhizobium* was isolated from the sediment of an antimony oxide-producing factory in Korea (Nguyen and Lee, 2014). Researchers found that this microorganism had the ability to reduce antimonate Sb(V) (Nguyen and Lee, 2014). Although our understanding of the bioreduction of Sb(V) is still limited, the aforementioned studies suggest that the bioreduction of Sb(V) can offer a potential bioremediation and biorecovery route for Sb.

Comparatively little research has been carried out on the microbiological oxidation of antimonite. However, the biooxidation of arsenite has been intensively researched (Zhu et al., 2014), so these reaction pathways can be used as references in the biooxidation of antimonite. Terry (2015) isolated two bacteria (*Hydrogenophaga taeniospiralis* strain IDSBO-1 and *Variovorax paradoxus* strain IDSBO-4) from contaminated lands in stibnite/yellow pine

mining area of Idaho USA and showed that these two bacteria can oxidize Sb(III) to Sb(V). Strain IDSBO-1 uses oxygen to achieve the oxidation of the antimonite whereas with strain IDSBO-4, oxidation proceeds with nitrate. Enrichment experiments were also conducted in this study. Sediment which contained bacteria, yeast extract and Sb(III) solution were added together. The results showed that precipitates comprising 72% mopungite ($NaSb(OH)_6$) and 28% Sb(III)-bearing senarmontite (Sb_2O_3) were produced in this experiment (Terry et al., 2015).

Aside from the bioreduction and biooxidation of Sb, a further bioremediation method has been reported in which high concentrations of soluble Sb(V) were first adsorbed by ferrihydrite and then transformed by Fe(III)-reducing bacteria (*Shewanella putrefaciens)* under anaerobic conditions (Burton et al., 2019). The results show that cryptocrystalline ferrihydrite with adsorbed Sb was converted into goethite, while antimony was not released into solution. This formation process of secondary Fe minerals is considered to be beneficial to the immobilisation of antimony under reducing conditions (Burton et al., 2019).

2.2.3 The bio-recovery of gold (Au)

According to the study of Deplanche and Macaskie (2008), *Escherichia coli* and *Desulfovibrio desulfuricans* were used to recover gold from Au(III)-bearing solutions. Bioreduction was the basis of the whole recovery process in the latter

study, and H_2 acted as the electron donor. The results showed that both strains can reduce aqueous Au(III) ions at pH 7 using 2 mM $HAuCl_4$ solution. In addition, Deplanche and Macaskie (2008) also used real jewellery leachates to test the feasibility of this biorecovery process on actual gold-bearing waste liquor; nearly 100% of Au ions were recovered from acidic leachate (115 ppm of Au(III)). The Au(0) nanoparticle size was smaller at acidic pH (2.0) compared to that obtained at pH 6.0 and 7.0 and 9.0. Most of the recovered gold particles were located on cell surfaces with a small number of intracellular nanoparticles also noted (Deplanche and Macaskie, 2008).

In another study from Singapore, Natarajan and Ting (2015) conducted a biological leaching process to recover gold from electronic scrap materials (ESM) via gold–cyanide complexation, using cyanide produced from pure and mixed cultures of cyanogenic bacteria: *Chromobacterium violaceum, Pseudomonas aeruginosa* and *Pseudomonas fluorescens*. The results indicated that pure cultures of *Chromobacterium violaceum* offered the highest cyanide production and achieved the highest gold recovery levels. A two-step leaching method described below was compared to a spent medium bioleaching protocol in this experiment. For the two-step leaching method, bacteria were first cultured. Then after reaching the maximum bacterial growth (and cyanide) yield, clean solid ESM were added to the solution with bacteria to start the biorecovery process. The method recovered ~11% of the gold in the

ESM.

Another approach focused on using a spent medium bioleaching method. The first step was the same as previously outlined (culture the bacteria to the highest growth yield), but here they removed all cells before adding the ESM to the solution, and the gold-recovery yield increased to 18%. Natarajan and Ting (2015) proposed that in the two-step leaching method, cyanogenic bacteria also converted cyanide to β- cyano-alanine during the mid and late stationary phase, resulting in the decrease the recovery of gold (Natarajan and Ting, 2015). Zhu et al. (2016) also researched biorecovery methods for gold ions and tested catalytic activities for p-nitrophenol degradation of the gold nanoparticles produced. According to the Zhu et al. (2016) study, gold nanoparticles (AuNPs) were recovered using *Shewanella haliotis* with sodium lactate as electron donor. The concentration of biomass, initial gold ions and pH values were considered key controlling factors. Biomass and initial gold ion concentrations influenced the particle size of the products while pH had an influence on recovery efficiency. Under the optimal conditions, around 85% of the AuNPs had a particle size of 10-30 nm. It was found that as the sizes of recovered AuNPs decreased, the rate of p-nitrophenol degradation activity increased (Zhu et al., 2016).

2.2.4 The biorecovery of platinum group metals (PGM)

Several recent studies on the biorecovery of PGM have been published.

Sulfate-reducing bacteria (*D. desulfuricans*) were found to reduce Pd(II) (model solution) to Pd(0), with pyruvate, formate and H_2 acting as electron donors (Lloyd et al., 1998). According to research reported in Murray et al. (2017), a two-step reduction method was chosen because waste leachates in their experiments were always very acidic (pH was around 2), which can inhibit microbial activities (Murray et al., 2017). Other studies have also shown that metallised cells can act as chemical catalysts for the bio-reduction of precious metals in acidic solutions (Creamer et al., 2006). Thus, in the first step of the Murray et al. (2017) experiments, *Escherichia coli* MC 4100 was chosen to reduce Pd(II) or Pt(IV), from artificial solution to nano-particulate cell-bound Pd(0) and Pt(0). These metallised cells were then used to recover PGM ions from model solutions and spent automotive catalyst leachates (which were dissolved by aqua regia). In addition, nanoparticles produced by these processes were tested as new catalysts for the reduction of Cr(IV). The results showed that compared with metal removal rates from lab model solutions, the metal removal rate from the spent automotive catalyst leachates was slower because other contaminants in the leachates inhibited the reduction rate. However, in terms of catalyst efficiency testing for the Cr(IV) reduction experiments, the biofabricated catalyst reduced Cr(IV) to a similar extent as commercial catalysts (around 90%).

A review by Butu et al. (2016) discussed how Halophilic mixed cultures (mainly

containing *Halomonadaceae, Bacillaceae*, and *Idiomarinaceae*) were tested for the biorecovery of platinum (Butu et al., 2016). The halophilic cultures were able to recover over 98% Pt (II) and over 97% Pt (IV) at pH 2, within 3–21 hours in solution (Maes et al., 2016). Other studies (e.g., from Liang and Gadd, 2017) showed that fungi could be used in the biorecovery of metals. Liang and Gadd (2017) did not provide detailed information about whether PGE ores can be recovered by fungi but the potential for fungi in the field of biorecovery of PGM was suggested (via biomineralization and bioprecipitation) (Liang and Gadd, 2017).

More information about the bioremediation of platinum-bearing wastes is summarised in the review of Nancharaiah (2016), concerning the biorecovery of critical and scarce metals (table 2.3).

Table 2.3 Microbe–Metal Interaction for Immobilization of PGM (Nancharaiah et al., 2016)

platinum group metals			
Metal	Organism	Metal source	bioremediation process
Pd	*Anabaena, Bacteroides vulgatus, Bacillus sphaericus, Calothrix, Clostridium pasterianum, Cupriavidus metallidurans,C. nector, Citrobacter braakii, Delsulfovibrio desulfuricans, D. fructosivorans, D. vulgaris, Paracoccus denitrificans, Pseudmonas putida, Plectonema boryanum, Geobacter*	Na_2PdCl_4	Bioreduction

	sulfurreducens		
	Serratia sp. biofilm	Na_2PdCl_4	Bioreduction
	Aerobic granular sludge	Na_2PdCl_4	Bioreduction
	Anaerobic granular sludge	Na_2PdCl_4	Bioreduction
Pt	*D.sulfuricans,shewanellaalgae, Pseudomonas sp.*	$PtCl_6^{2-}$	Bioreduction
Ru	Bacterial biomass/chitosan	Ru-acetate	Biosorption

From the table, it is clear that biorecovery methods for the PGM mainly focus on Pd and Pt, while research on the other PGM is still limited. In addition, there is very little research focusing on the biorecovery of PGM from contaminated land or mining wastes.

2.3 Introduction to dissimilatory metal reducing bacteria (DMRB): *Geobacter sulfurreducens*

Dissimilatory metal-reducing bacteria (DMRB) can reduce a number of high oxidation metals and metalloid ions to affect their oxidation states and solubility by using organic matter as electron donors in the environment (Lloyd, 2003). *Geobacter* species which are Gram-negative anaerobic bacteria belong to the DMRB and are widely distributed in subsurface environments (groundwater, sediment and soil) (Mahadevan et al., 2011; Muhamadali et al., 2015). *Geobacter* species are important in the global metal cycle and in the carbon cycle of the natural subsurface environment. They can gain energy for growth via the reduction of Fe(III) and other metal ions coupled to the oxidation of natural organic matter, such as acetate (Lovley, 1995; Methe et al., 2003).

Geobacter sulfurreducens PCA is a model *Geobacter* species and was isolated from surface sediments of a hydrocarbon-contaminated ditch in Norman, Oklahoma (Caccavo Jr et al., 1994). *G. sulfurreducens* was found to be able to reduce Fe(III), elemental sulfur, fumarate, Co(III)-EDTA and some other metals by using acetate as electron donor, with the acetate oxidised to CO_2. Figure 2.3 shows the acetate metabolism pathway when fumarate is used as an electron acceptor (Muhamadali et al., 2015). According to previous research, fumarate cannot be oxidised or used as a carbon and energy source (Caccavo Jr et al., 1994; Mahadevan et al., 2006). Acetate was imported in 2 ways by *G. sulfurreducens*. As Figure 2.3 shows, the first way (yellow) is that acetate is oxidised to acetyl-CoA through the transformation process of succinyl-CoA to succinate, via the activity of succinyl-CoA:acetate CoA-transferase enzyme (EC 2.8.3.18). The acetyl-CoA formed can participate in the tricarboxylic acid (TCA) cycle to form citrate (blue) (Muhamadali et al., 2015; Segura et al., 2008). The second pathway involves transfer of acetate to Acetyl-CoA, but through the activity of phosphotransacetylase enzyme (EC 2.3.1.8) (purple). The Acetyl-CoA formed is converted to pyruvate by the reversed activity of pyruvate oxidoreductase (EC 1.2.7.1). The oxidation of ferredoxin produced by the TCA cycle leads to this reduction process. During this process, fumarate is taken up by *G. sulfurreducens* used as an electron acceptor (Galushko and Schink, 2000; Muhamadali et al., 2015; Segura et al., 2008).

According to previous research, during the reduction processes of fumarate, 1.5 mol ATP are generated when 1 mol acetate is consumed (Mahadevan et al., 2006). When insoluble Fe(III) (or electrodes) act as an electron acceptor, compared to the reduction process of fumarate, the reduction reaction takes place outside the cell. During the Fe(III) reduction process, electrons are transferred to the outside of the cell and combined with Fe(III) to promote the reduction process. However, taking into account all protons produced and consumed during metabolism, the theoretical maximum yield with Fe(III) as the electron acceptor is 0.5 mol of ATP per 1 mol of acetate consumed, which is one third of that when fumarate is used. This observation suggests that less biomass is produced when *G. sulfurreducenss* reduces extracellular electron acceptors than when reducing intracellular electron acceptors (Mahadevan et al., 2006). *G. sulfurreducens* can also reduce Fe(III) citrate to Fe(II) coupling with the oxidation of hydrogen or acetate (Caccavo Jr et al., 1994; Lovley et al., 2004). The following equation can show the former process: $2\ Fe(III) + H_2 \rightarrow 2H^+ + 2Fe(II)$. In addition to reducing some metal ions, *G. sulfurreducens* also plays an important role in the transformation of Fe minerals in subsurface environments (Coker et al., 2008; Cutting et al., 2009).

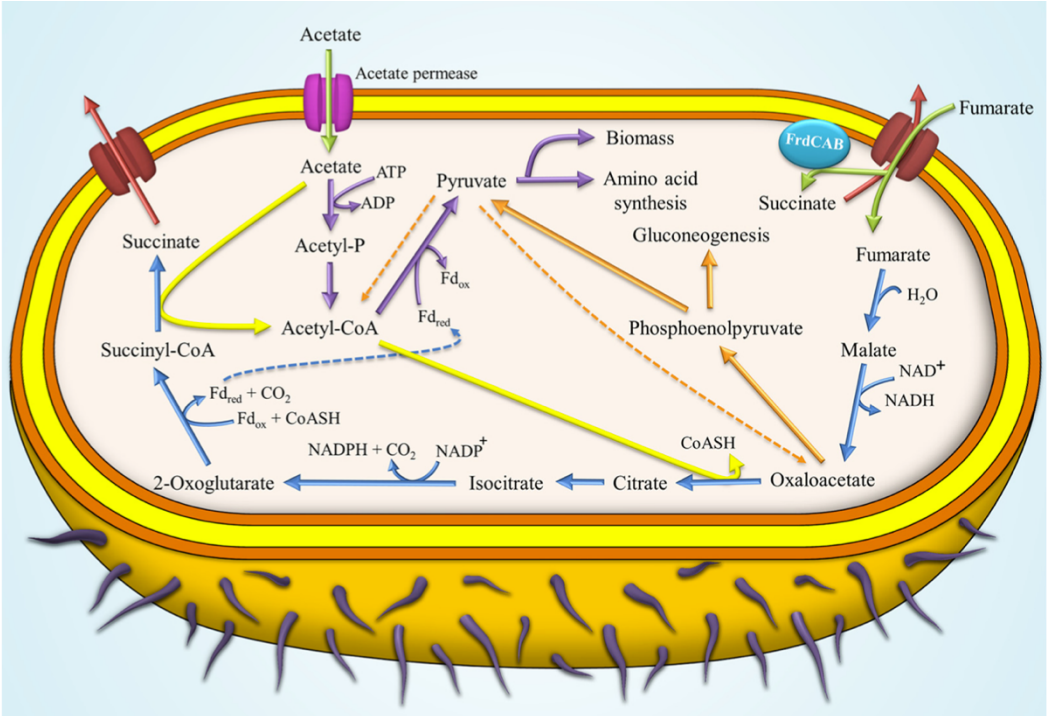

Figure 2.3 Pathway of acetate metabolism in *G. sulfurreducens* during growth on NBAF medium with fumarate as the electron acceptor and acetate as the electron donor (Muhamadali et al., 2015)

2.3.1 The bioreduction and bioremediation of metal contaminations by *G. sulfurreducens*

As mentioned above, *G. sulfurreducens* can use organic matter and hydrogen as electron donors and reduce a range of metal ions extracellularly. Thus it is feasible to use *G. sulfurreducens* in the bioremediation and biorecovery of metal contamination such as U(VI), Cu(II), Co(III) and Cr(VI) in the subsurface environment (Cutting et al., 2010; Kimber et al., 2020; Lloyd, 2003; Lloyd and Lovley, 2001; Telling et al., 2009). For example, uranium is a common radioactive contaminant in groundwater near to nuclear legacy sites (Law et al., 2011; Renshaw et al., 2005). U(IV) and U(VI) are the two most common oxidation states for uranium in the natural environment. U(VI) usually occurs as

UO_2^{2+} which is soluble under acidic and carbonate rich environments, while U(IV) is essentially insoluble in the environment. According to previous research, U(VI) can be reduced to U(IV) by *G. sulfurreducens* under anaerobic conditions, which can cause the immobilisation of uranium (Finneran et al., 2002; Law et al., 2011; Lloyd and Renshaw, 2005; Lovley et al., 1991; Williams et al., 2013).

Other research shows that *G. sulfurreducens* can reduce U(VI) which was adsorbed by both synthetic Fe(III) oxides and natural Fe(III)-bearing soil and sediment. The reduction rate and extent of U(VI) in synthetic Fe(III) oxides is similar to that observed in the reduction of aqueous U(VI), and much higher than that in natural Fe(III) mineral-bearing soils and sediments. A possible explanation for the latter observation could be that the cumulative microporosity of natural samples is around 5-10-fold larger than that of synthetic Fe(III) oxides, and the association of U(VI) with natural sediment hinders the bioreduction of U(VI) (Jeon et al., 2004). Co(III)-EDTA can also be reduced to Co(II)-EDTA by *G. sulfurreducens* when using acetate as electron doner (Caccavo Jr et al., 1994). When Co(III)-EDTA is reduced to Co(II)-EDTA, the stability of the complex decreases and the displaced Co(II) is more easily immobilised by oxide minerals (Gorby et al., 1998).

2.3.2 Biotransformation of Fe minerals by *G. sulfurreducens*

Iron oxide minerals are widely distributed in the natural environment (Jenne, 1968) where they exhibit a range of crystal structural variations (Cornell and Schwertmann, 2003; Cutting et al., 2009). For example, ferrihydrite (FeO(OH)) , goethite (α-FeO(OH)) and hematite Fe_2O_3 are all Fe(III) minerals but ferrihydrite is a mineral without a stable crystal structure while goethite and hematite are both crystalline phases. Magnetite is also an iron oxide phase with an ideal chemical formula of Fe_3O_4, and is a common product of microbial Fe(III) reduction. It has a cubic inverse spinel structure with oxygen atoms in a close packed structure; half of the Fe(III) occupies the tetrahedral position (Td), while Fe(II) and the other half of the Fe(III) occupies the octahedral position (Oh) (Coker et al., 2006; Coker et al., 2007; Sun and Zeng, 2002).

Previous studies have shown that *G. sulfurreducens* can not only reduce aqueous Fe(III) ions but can also reduce some Fe(III) oxide phases in subsurface environments (Caccavo Jr et al., 1992; Caccavo Jr et al., 1994; Xiu et al., 2021). However, the crystallinity of Fe oxide minerals has been shown to influence the bioavailability of *G. sulfurreducens*; for example, according to Cutting et al. (2009), a series of Fe(III)-hydroxyl oxides with different crystallinities and effective surface areas were reduced by *G. sulfurreducens*. The latter results show that hematite and goethite which contain a stable crystal structure are not easily reduced by *G. sulfurreducens* while the cryptocrystalline

schwertmannite and ferrihydrite are more readily transformed to magnetite during similar reactions (Cutting et al., 2009).

Other research also shows that poorly crystalline Fe(III) minerals such as ferrihydrite and schwertmannite can be reduced to magnetite nanoparticles by *G. sulfurreducens* (Coker et al., 2008; Coker et al., 2007; Cutting et al., 2012). According to Byrne et al. (2011), the size of the biomagnetite particles generated can be controlled by the initial biomass of *G. sulfurreducens*, and ranges from 10-50 nm. In addition, through adding the electron shuttle analogue anthraquinone-2,6-disulfonate (AQDS) and controlling the initial biomass (OD_{600} from 0.015-4), the final bioproducts can comprise different Fe minerals. Goethite is the main product when the initial biomass is low, magnetite is formed at moderate concentrations, and siderite ($FeCO_3$) is formed at the highest concentrations (Byrne et al., 2011). In addition to the initial biomass affecting the transformation of Fe minerals by *G. sulfurreducens*, the incorporation and adsorption of some metal and metallic ions in the initial Fe(III) oxides also affect the types of Fe minerals after reduction. For example, the bioreduction products of schwertmannite by *G. sulfurreducens* is magnetite at pH 7; however, when As(V)-doped schwertmannite is used, and the content of As(V) is increased in the initial material, the final product may be goethite instead of magnetite (Cutting et al., 2012).

Many studies have shown that magnetite, especially magnetite nanoparticles, can have a wide range of uses such as catalysts and remediation agents for contaminated land and water sources. Therefore, the use of *G. sulfurreducens* to produce biomagnetite has potentially significant applications and, according to research of Byrne et al. (2015), this process has been successfully scaled up, from laboratory scale to pilot plant scale production (Byrne et al., 2015).

Reference:

Akpalu, W. & Normanyo, A. K. (2017). 'Gold mining pollution and the cost of private healthcare: The case of ghana' *Ecological Economics*, 142 pp. 104-112.

Alvarez, P. J. & Illman, W. A. (2005). *Bioremediation and natural attenuation: Process fundamentals and mathematical models*. John Wiley & Sons.

Anderson, C. (2019). 'Antimony production and commodities' *SME mineral processing & extractive metallurgy handbook. society for mining, metallurgy, and exploration. Engelwood*.

Andres, Y., Texier, A.-C. & Le Cloirec, P. (2003). 'Rare earth elements removal by microbial biosorption: A review' *Environmental technology*, 24 (11), pp. 1367-1375.

Anthony, M. & Flett, D. (1994). 'Hydrometallurgy—an environmentally sustainable technology?', *Hydrometallurgy'94*: Springer, pp. 13-26.

Bento, F. M., Camargo, F. A., Okeke, B. C. & Frankenberger, W. T. (2005). 'Comparative bioremediation of soils contaminated with diesel oil by natural attenuation, biostimulation and bioaugmentation' *Bioresource technology*, 96 (9), pp. 1049-1055.

Bosch, D. & Pradkhan, E. (2015). 'The impact of speculation on precious metals futures markets' *Resources Policy*, 44 pp. 118-134.

Brenan, J. M. (2008). 'The platinum-group elements:"Admirably adapted" for science and industry' *Elements*, 4 (4), pp. 227-232.

Brisson, V. L., Zhuang, W. Q. & Alvarez-Cohen, L. (2016). 'Bioleaching of rare earth elements from monazite sand' *Biotechnology and bioengineering*, 113 (2), pp. 339-348.

Burton, E. D., Hockmann, K., Karimian, N. & Johnston, S. G. (2019). 'Antimony mobility in reducing environments: The effect of microbial iron(iii)-reduction and associated secondary mineralization' *Geochimica et cosmochimica acta*, 245 pp. 278-289. DOI: 10.1016/j.gca.2018.11.005.

Butu, A., Rodino, S., Dobre, A. & Butu, M. (2016). 'Potential of microbial functional communities for high-tech critical metals recovery' *Studia Universitatis Vasile Goldis Seria Stiintele Vietii (Life Sciences Series)*, 26 (2).

Byrne, J. M., et al. (2015). 'Scale-up of the production of highly reactive biogenic magnetite nanoparticles using *geobacter sulfurreducens*' *Journal of the royal society interface*, 12 (107), p. 20150240.

Byrne, J. M., et al. (2011). 'Control of nanoparticle size, reactivity and magnetic properties during the bioproduction of magnetite by *geobacter sulfurreducens*' *Nanotechnology*, 22 (45), p. 455709. DOI: 10.1088/0957-4484/22/45/455709.

Caccavo Jr, F., Blakemore, R. P. & Lovley, D. R. (1992). 'A hydrogen-oxidizing, fe (iii)-reducing microorganism from the great bay estuary, new

hampshire' *Applied and Environmental Microbiology*, 58 (10), pp. 3211-3216.

Caccavo Jr, F., et al. (1994). '*Geobacter sulfurreducens* sp. Nov., a hydrogen- and acetate-oxidizing dissimilatory metal-reducing microorganism' *Applied and environmental microbiology*, 60 (10), pp. 3752-3759.

Cao, Y., Guo, Q., Liang, M. & Sun, W. (2020). 'Sb (iii) and sb (v) removal from water by a hydroxyl-intercalated, mechanochemically synthesized mg-fe-ldh' *Applied Clay Science*, 196 p. 105766.

Chang, E., et al. (2020). 'Surface complexation model of rare earth element adsorption onto bacterial surfaces with lanthanide binding tags' *Applied Geochemistry*, 112 p. 104478.

Cinti, D., Angelone, M., Masi, U. & Cremisini, C. (2002). 'Platinum levels in natural and urban soils from rome and latium (italy): Significance for pollution by automobile catalytic converter' *Science of the Total Environment*, 293 (1-3), pp. 47-57.

Coker, V., et al. (2006). 'Xas and xmcd evidence for species-dependent partitioning of arsenic during microbial reduction of ferrihydrite to magnetite' *Environmental science & technology*, 40 (24), pp. 7745-7750.

Coker, V. S., et al. (2008). 'Time-resolved synchrotron powder x-ray diffraction study of magnetite formation by the fe (iii)-reducing bacterium g*eobacter sulfurreducens*' *American Mineralogist*, 93 (4), pp. 540-547.

Coker, V. S., et al. (2007). 'Cation site occupancy of biogenic magnetite compared to polygenic ferrite spinels determined by x-ray magnetic circular dichroism' *European Journal of Mineralogy*, 19 (5), pp. 707-716.

Commission, E. (2020). Study on the eu's list of critical raw materials. European Commission Brussels, Belgium.

Cornell, R. M. & Schwertmann, U. (2003). *The iron oxides : Structure, properties, reactions, occurrences, and uses*. 2nd, completely rev. and extended edn. Weinheim: Wiley-VCH.

Creamer, N. J., et al. (2006). 'Palladium and gold removal and recovery from precious metal solutions and electronic scrap leachates by *desulfovibrio desulfuricans*' *Biotechnology letters*, 28 (18), pp. 1475-1484.

Cutting, R. S., et al. (2009). 'Mineralogical and morphological constraints on the reduction of fe(iii) minerals by *geobacter sulfurreducens*' *Geochimica et cosmochimica acta*, 73 (14), pp. 4004-4022. DOI: 10.1016/j.gca.2009.04.009.

Cutting, R. S., et al. (2010). 'Optimizing cr (vi) and tc (vii) remediation through nanoscale biomineral engineering' *Environmental science & technology*, 44 (7), pp. 2577-2584.

Cutting, R. S., et al. (2012). 'Microbial reduction of arsenic-doped schwertmannite by *geobacter sulfurreducens*' *Environmental science & technology*, 46 (22), pp. 12591-12599.

Deplanche, K. & Macaskie, L. (2008). 'Biorecovery of gold by escherichia coli and *desulfovibrio desulfuricans*' *Biotechnology and bioengineering*, 99 (5), pp. 1055-1064.

Dong, H., et al. (2015). 'Recovery of platinum group metals from spent catalysts: A review' *International Journal of Mineral Processing*, 145 pp. 108-113.

Dovick, M. A., Kulp, T. R., Arkle, R. S. & Pilliod, D. S. (2015). 'Bioaccumulation trends of arsenic and antimony in a freshwater ecosystem affected by mine drainage' *Environmental Chemistry*, 13 (1), pp. 149-159.

Du, H., et al. (2020). 'Bacteria affect sb (iii, v) adsorption and oxidation on birnessite' *Journal of Soils and Sediments*, 20 (5), pp. 2418-2425.

Ek, K. H., Morrison, G. M. & Rauch, S. (2004). 'Environmental routes for platinum group elements to biological materials—a review' *Science of the Total Environment*, 334 pp. 21-38.

ENTR, D. (2014). 'Report on critical raw materials for the eu' *European Commission*.

EU (1998). 'Council directive 98/83/ec of 3 november 1998 on the quality of water intended for human consumption' *Official journal of the European communities*, 41 pp. 32-54.

Feng, R., et al. (2013). 'The uptake and detoxification of antimony by plants: A review' *Environmental and experimental botany*, 96 pp. 28-34.

Fernandez, V. (2017). 'Rare-earth elements market: A historical and financial perspective' *Resources Policy*, 53 pp. 26-45.

Ferreira, G. & Critelli, J. (2022). 'China's global monopoly on rare-earth elements' *The US Army War College Quarterly: Parameters*, 52 (1), pp. 57-72.

Filella, M., Belzile, N. & Chen, Y.-W. (2002a). 'Antimony in the environment: A review focused on natural waters: I. Occurrence' *Earth-Science Reviews*, 57 (1-2), pp. 125-176.

Filella, M., Belzile, N. & Chen, Y.-W. (2002b). 'Antimony in the environment: A review focused on natural waters: Ii. Relevant solution chemistry' *Earth-science reviews*, 59 (1), pp. 265-285. DOI: 10.1016/S0012-8252(02)00089-2.

Filella, M., Belzile, N. & Lett, M.-C. (2007). 'Antimony in the environment: A review focused on natural waters. Iii. Microbiota relevant interactions' *Earth-Science Reviews*, 80 (3-4), pp. 195-217.

Finneran, K. T., Anderson, R. T., Nevin, K. P. & Lovley, D. R. (2002). 'Potential for bioremediation of uranium-contaminated aquifers with microbial u (vi) reduction' *Soil and Sediment Contamination: An International Journal*, 11 (3), pp. 339-357.

Flower, B. & Goering, P. (1991). Antimony, v merian e.(ed.): Metals and their compounds in the environment. VCH Verlagsgesellschaft, Weinheim.

Foulkes, J. M., et al. (2016). 'A novel aerobic mechanism for reductive palladium biomineralization and recovery by *escherichia coli*' *Geomicrobiology Journal*, 33 (3-4), pp. 230-236.

Gadd, G. M. (2010). ‘Metals, minerals and microbes: Geomicrobiology and bioremediation’ *Microbiology*, 156 (3), pp. 609-643.

Galushko, A. S. & Schink, B. (2000). ‘Oxidation of acetate through reactions of the citric acid cycle by *geobacter sulfurreducens* in pure culture and in syntrophic coculture’ *Archives of microbiology*, 174 (5), pp. 314-321.

Gebel, T. (1997). ‘Arsenic and antimony: Comparative approach on mechanistic toxicology’ *Chemico-biological interactions*, 107 (3), pp. 131-144.

Giese, E. C. (2020). ‘Biosorption as green technology for the recovery and separation of rare earth elements’ *World Journal of Microbiology and Biotechnology*, 36 (4), pp. 1-11.

Girtan, M., et al. (2021). The critical raw materials issue between scarcity, supply risk, and unique properties. Multidisciplinary Digital Publishing Institute.

Goodenough, K., et al. (2016). ‘Europe's rare earth element resource potential: An overview of ree metallogenetic provinces and their geodynamic setting’ *Ore Geology Reviews*, 72 pp. 838-856.

Gorby, Y. A., Caccavo, F. & Bolton, H. (1998). ‘Microbial reduction of cobaltiiiedta-in the presence and absence of manganese (iv) oxide’ *Environmental science & technology*, 32 (2), pp. 244-250.

Graedel, T. E., et al. (2012). ‘Methodology of metal criticality determination’ *Environmental science & technology*, 46 (2), pp. 1063-1070.

Guo, X., et al. (2014). ‘Adsorption of antimony onto iron oxyhydroxides: Adsorption behavior and surface structure’ *Journal of hazardous materials*, 276 pp. 339-345.

Haque, N., Hughes, A., Lim, S. & Vernon, C. (2014). ‘Rare earth elements: Overview of mining, mineralogy, uses, sustainability and environmental impact’ *Resources*, 3 (4), pp. 614-635.

Hayes-Labruto, L., Schillebeeckx, S. J., Workman, M. & Shah, N. (2013). ‘Contrasting perspectives on china's rare earths policies: Reframing the debate through a stakeholder lens’ *Energy Policy*, 63 pp. 55-68.

He, M., Wang, X., Wu, F. & Fu, Z. (2012). ‘Antimony pollution in china’ *Science of the total environment*, 421 pp. 41-50.

Hu, H., Jin, Q. & Kavan, P. (2014). ‘A study of heavy metal pollution in china: Current status, pollution-control policies and countermeasures’ *Sustainability*, 6 (9), pp. 5820-5838.

Hughes, A. E., Haque, N., Northey, S. A. & Giddey, S. (2021). ‘Platinum group metals: A review of resources, production and usage with a focus on catalysts’ *Resources*, 10 (9), p. 93.

Hurst, C. (2010). *China's rare earth elements industry: What can the west learn?* : Institute for the Analysis of Global Security Washington DC.

Ilgen, A. G., et al. (2014). ‘Oxidation and mobilization of metallic antimony in aqueous systems with simulated groundwater’ *Geochimica et Cosmochimica Acta*, 132 pp. 16-30.

Işıldar, A., et al. (2017). 'Biorecovery of metals from electronic waste', *Sustainable heavy metal remediation*: Springer, pp. 241-278.

Jackson, M. T., Sampson, J. & Prichard, H. M. (2007). 'Platinum and palladium variations through the urban environment: Evidence from 11 sample types from sheffield, uk' *Science of the Total Environment*, 385 (1-3), pp. 117-131.

Jenne, E. A. (1968). 'Controls on mn, fe, co, ni, cu, and zn concentrations in soils and water: The significant role of hydrous mn and fe oxides': ACS Publications.

Jeon, B.-H., et al. (2004). 'Microbial reduction of u (vi) at the solid− water interface' *Environmental science & technology*, 38 (21), pp. 5649-5655.

Kantin, R. (1983). 'Chemical speciation of antimony in marine algae' *Limnology and Oceanography*, 28 (1), pp. 165-168.

Karim, S. & Ting, Y.-P. (2021). 'Recycling pathways for platinum group metals from spent automotive catalyst: A review on conventional approaches and bio-processes' *Resources, Conservation and Recycling*, 170 p. 105588.

Kettler, P. B. (2003). 'Platinum group metals in catalysis: Fabrication of catalysts and catalyst precursors' *Organic process research & development*, 7 (3), pp. 342-354.

Kimber, R. L., et al. (2020). 'Biomineralization of cu2s nanoparticles by *geobacter sulfurreducens*' *Applied and environmental microbiology*, 86 (18), pp. e00967-20.

Kulp, T. R., et al. (2014). 'Microbiological reduction of sb (v) in anoxic freshwater sediments' *Environmental science & technology*, 48 (1), pp. 218-226.

Kuppusamy, S., et al. (2016). 'In-situ remediation approaches for the management of contaminated sites: A comprehensive overview' *Reviews of Environmental Contamination and Toxicology Volume 236*, pp. 1-115.

Lai, C.-Y., et al. (2016). 'Autotrophic antimonate bio-reduction using hydrogen as the electron donor' *Water research*, 88 pp. 467-474.

Law, G. T., et al. (2011). 'Uranium redox cycling in sediment and biomineral systems' *Geomicrobiology Journal*, 28 (5-6), pp. 497-506.

Le, M. N. & Lee, M. S. (2021). 'A review on hydrometallurgical processes for the recovery of valuable metals from spent catalysts and life cycle analysis perspective' *Mineral Processing and Extractive Metallurgy Review*, 42 (5), pp. 335-354.

Li, J., et al. (2016). 'Microbial antimony biogeochemistry: Enzymes, regulation, and related metabolic pathways' *Applied and environmental microbiology*, 82 (18), pp. 5482-5495. DOI: 10.1128/AEM.01375-16.

Li, J., et al. (2018). 'Antimony contamination, consequences and removal techniques: A review' *Ecotoxicology and Environmental Safety*, 156 pp. 125-134.

Liang, X. & Gadd, G. M. (2017). 'Metal and metalloid biorecovery using fungi' *Microbial biotechnology*, 10 (5), pp. 1199-1205.
Liu, H. (2016). 'Rare earths: Shades of grey: Can china continue to fuel our global clean & smart future' *China Water Risk*.
Lloyd, J. R. (2003). 'Microbial reduction of metals and radionuclides' *FEMS microbiology reviews*, 27 (2-3), pp. 411-425.
Lloyd, J. R. & Lovley, D. R. (2001). 'Microbial detoxification of metals and radionuclides' *Current opinion in biotechnology*, 12 (3), pp. 248-253.
Lloyd, J. R. & Renshaw, J. C. (2005). 'Bioremediation of radioactive waste: Radionuclide–microbe interactions in laboratory and field-scale studies' *Current opinion in biotechnology*, 16 (3), pp. 254-260.
Lloyd, J. R., Yong, P. & Macaskie, L. E. (1998). 'Enzymatic recovery of elemental palladium by using sulfate-reducing bacteria' *Applied and Environmental Microbiology*, 64 (11), pp. 4607-4609.
Lovley, D. R. (1995). 'Bioremediation of organic and metal contaminants with dissimilatory metal reduction' *Journal of industrial microbiology*, 14 (2), pp. 85-93.
Lovley, D. R., et al. (1993). '*Geobacter metallireducens* gen. Nov. Sp. Nov., a microorganism capable of coupling the complete oxidation of organic compounds to the reduction of iron and other metals' *Archives of microbiology*, 159 (4), pp. 336-344.
Lovley, D. R., Holmes, D. E. & Nevin, K. P. (2004). 'Dissimilatory fe (iii) and mn (iv) reduction' *Advances in microbial physiology*, 49 (2), pp. 219-286.
Lovley, D. R., Phillips, E. J., Gorby, Y. A. & Landa, E. R. (1991). 'Microbial reduction of uranium' *Nature*, 350 (6317), pp. 413-416.
Lu, J., et al. (2012). 'Valuable metal recovery during the bioremediation of acidic mine drainage using sulfate reducing straw bioremediation system' *Water, Air, & Soil Pollution*, 223 (6), pp. 3049-3055.
Macaskie, L., et al. (2010). 'Today's wastes, tomorrow's materials for environmental protection' *Hydrometallurgy*, 104 (3-4), pp. 483-487.
Maes, S., et al. (2016). 'Platinum recovery from synthetic extreme environments by halophilic bacteria' *Environmental science & technology*, 50 (5), pp. 2619-2626.
Mahadevan, R., et al. (2006). 'Characterization of metabolism in the fe (iii)-reducing organism *geobacter sulfurreducens* by constraint-based modeling' *Applied and environmental microbiology*, 72 (2), pp. 1558-1568.
Mahadevan, R., Palsson, B. Ø. & Lovley, D. R. (2011). 'In situ to in silico and back: Elucidating the physiology and ecology of *geobacter* spp. Using genome-scale modelling' *Nature Reviews Microbiology*, 9 (1), pp. 39-50.
Megharaj, M., et al. (2011). 'Bioremediation approaches for organic pollutants: A critical perspective' *Environment international*, 37 (8), pp. 1362-1375.
Melber, C., Keller, D. & Mangelsdorf, I. (2002). 'Palladium: Environmental health criteria' *World Health Organization, Geneva*, 222.

Methe, B., et al. (2003). ‘Genome of *geobacter sulfurreducens*: Metal reduction in subsurface environments’ *Science*, 302 (5652), pp. 1967-1969.

Mitsunobu, S., Takahashi, Y. & Sakai, Y. (2008). ‘Abiotic reduction of antimony(v) by green rust (fe4(ii)fe2(iii)(oh)12so4 · 3h2o)’ *Chemosphere (Oxford)*, 70 (5), pp. 942-947. DOI: 10.1016/j.chemosphere.2007.07.021.

Mpinga, C., Eksteen, J., Aldrich, C. & Dyer, L. (2015). ‘Direct leach approaches to platinum group metal (pgm) ores and concentrates: A review’ *Minerals Engineering*, 78 pp. 93-113.

Mudd, G. M. (2012). ‘Key trends in the resource sustainability of platinum group elements’ *Ore Geology Reviews*, 46 pp. 106-117.

Mudd, G. M., Jowitt, S. M. & Werner, T. T. (2018). ‘Global platinum group element resources, reserves and mining–a critical assessment’ *Science of the Total Environment*, 622 pp. 614-625.

Muhamadali, H., et al. (2015). ‘Metabolic profiling of *geobacter sulfurreducens* during industrial bioprocess scale-up’ *Applied and environmental microbiology*, 81 (10), pp. 3288-3298.

Murray, A., Zhu, J., Wood, J. & Macaskie, L. (2017). ‘A novel biorefinery: Biorecovery of precious metals from spent automotive catalyst leachates into new catalysts effective in metal reduction and in the hydrogenation of 2-pentyne’ *Minerals Engineering*, 113 pp. 102-108.

Nancharaiah, Y., Mohan, S. V. & Lens, P. (2016). ‘Biological and bioelectrochemical recovery of critical and scarce metals’ *Trends in biotechnology*, 34 (2), pp. 137-155.

Natarajan, G. & Ting, Y.-P. (2015). ‘Gold biorecovery from e-waste: An improved strategy through spent medium leaching with ph modification’ *Chemosphere*, 136 pp. 232-238.

Nguyen, V. K. & Lee, J.-U. (2014). ‘Isolation and characterization of antimony-reducing bacteria from sediments collected in the vicinity of an antimony factory’ *Geomicrobiology Journal*, 31 (10), pp. 855-861.

O'Driscoll, B., Garwood, R., Day, J. M. & Wogelius, R. (2018). ‘Platinum-group element remobilization and concentration in the cliff chromitites of the shetland ophiolite complex, scotland’ *Mineralogical Magazine*, 82 (3), pp. 471-490.

O’Driscoll, B. & González-Jiménez, J. M. (2016). ‘Petrogenesis of the platinum-group minerals’ *Reviews in Mineralogy and Geochemistry*, 81 (1), pp. 489-578.

Ohnuki, T., et al. (2015). ‘Sorption of trivalent cerium by a mixture of microbial cells and manganese oxides: Effect of microbial cells on the oxidation of trivalent cerium’ *Geochimica et Cosmochimica Acta*, 163 pp. 1-13.

Ohnuki, T., et al. (2008). ‘Concurrent transformation of ce (iii) and formation of biogenic manganese oxides’ *Chemical Geology*, 253 (1-2), pp. 23-29.

Park, D. M., et al. (2016). ‘Bioadsorption of rare earth elements through cell surface display of lanthanide binding tags’ *Environmental science & technology*, 50 (5), pp. 2735-2742.

Paulick, H. & Machacek, E. (2017). ‘The global rare earth element exploration boom: An analysis of resources outside of china and discussion of development perspectives’ *Resources Policy*, 52 pp. 134-153.

Pergent, G. & Pergent-Martini, C. (1999). ‘Mercury levels and fluxes in posidonia oceanica meadows’ *Environmental pollution*, 106 (1), pp. 33-37.

Pierart, A., Shahid, M., Séjalon-Delmas, N. & Dumat, C. (2015). ‘Antimony bioavailability: Knowledge and research perspectives for sustainable agricultures’ *Journal of hazardous materials*, 289 pp. 219-234.

Priya, M., Gurung, N., Mukherjee, K. & Bose, S. (2014). 'Microalgae in removal of heavy metal and organic pollutants from soil', *Microbial biodegradation and bioremediation*: Elsevier, pp. 519-537.

Rakshit, S., Sarkar, D., Punamiya, P. & Datta, R. (2011). ‘Antimony sorption at gibbsite–water interface’ *Chemosphere*, 84 (4), pp. 480-483.

Rana, S., et al. (2020). ‘Microbe-mediated sustainable bio-recovery of gold from low-grade precious solid waste: A microbiological overview’ *Journal of Environmental Sciences*, 89 pp. 47-64.

Rao, C. & Reddi, G. (2000). ‘Platinum group metals (pgm); occurrence, use and recent trends in their determination’ *TrAC Trends in Analytical Chemistry*, 19 (9), pp. 565-586.

Ravindra, K., Bencs, L. & Van Grieken, R. (2004). ‘Platinum group elements in the environment and their health risk’ *Science of the total environment*, 318 (1-3), pp. 1-43.

Renshaw, J. C., et al. (2005). ‘Bioreduction of uranium: Environmental implications of a pentavalent intermediate’ *Environmental Science & Technology*, 39 (15), pp. 5657-5660.

Reuter, M., et al. (2013). ‘Metal recycling: Opportunities, limits, infrastructure’ *A report of the working group on the global metal flows to the international resource panel*.

Sahu, P., Jena, M., Mandre, N. R. & Venugopal, R. (2021). ‘Platinum group elements mineralogy, beneficiation, and extraction practices–an overview’ *Mineral Processing and Extractive Metallurgy Review*, 42 (8), pp. 521-534.

Sathishkumar, M., et al. (2010). ‘Green recovery of gold through biosorption, biocrystallization, and pyro-crystallization’ *Industrial & Engineering Chemistry Research*, 49 (16), pp. 7129-7135.

Schmitt, C. J., et al. (2007). ‘Biomarkers of metals exposure in fish from lead-zinc mining areas of southeastern missouri, USA’ *Ecotoxicology and Environmental Safety*, 67 (1), pp. 31-47.

Segura, D., Mahadevan, R., Juárez, K. & Lovley, D. R. (2008). 'Computational and experimental analysis of redundancy in the central metabolism of geobacter sulfurreducens' *PLoS computational biology*, 4 (2), p. e36.

Sterner, R. W. & Elser, J. J. (2017). *Ecological stoichiometry*. Princeton university press.

Sun, S. & Zeng, H. (2002). 'Size-controlled synthesis of magnetite nanoparticles' *Journal of the American Chemical Society*, 124 (28), pp. 8204-8205.

Telling, N., et al. (2009). 'Remediation of cr (vi) by biogenic magnetic nanoparticles: An x-ray magnetic circular dichroism study' *Applied Physics Letters*, 95 (16), p. 163701.

Ternjej, I., Srček, V. G., Mihaljević, Z. & Kopjar, N. (2013). 'Cytotoxic and genotoxic effects of water and sediment samples from gypsum mining area in channel catfish ovary (cco) cells' *Ecotoxicology and environmental safety*, 98 pp. 119-127.

Terry, L. R., et al. (2015). 'Microbiological oxidation of antimony(iii) with oxygen or nitrate by bacteria isolated from contaminated mine sediments' *Applied and environmental microbiology*, 81 (24), pp. 8478-8488. DOI: 10.1128/AEM.01970-15.

Tesfaye, F., Lindberg, D. & Hamuyuni, J. (2017). 'Valuable metals and energy recovery from electronic waste streams', *Energy technology 2017*: Springer, pp. 103-116.

Todand, M. M., Jarvis, I. & Jarvis, K. E. (1995). 'Microwave digestion and alkali fusion procedures for the determination of the platinum-group elements and gold in geological materials by icp-ms' *Chemical Geology*, 124 (1-2), pp. 21-36.

USEPA (1999). National primary drinking water standards. United States Environmental Protection Agency Office

USGS (2020). Mineral commodity summaries 2020.

Vermaak, C. 'Platinum-group metals: A global perspective mintek, randburg, south africa, 1995' *Google Scholar There is no corresponding record for this reference*.

Vijayaraghavan, K., Sathishkumar, M. & Balasubramanian, R. (2010). 'Biosorption of lanthanum, cerium, europium, and ytterbium by a brown marine alga, turbinaria conoides' *Industrial & engineering chemistry research*, 49 (9), pp. 4405-4411.

Wang, H., et al. (2013). 'Removal of antimony (sb(v)) from sb mine drainage: Biological sulfate reduction and sulfide oxidation–precipitation' *Bioresource technology*, 146 pp. 799-802. DOI: 10.1016/j.biortech.2013.08.002.

Wang, Y., et al. (2022). 'Au (iii)-induced extracellular electron transfer by burkholderia contaminans zcc for the bio-recovery of gold nanoparticles' *Environmental Research*, 210 p. 112910.

WHO, W. H. O. (1991). ‘Environmental health criteria platinum’ *International Programme on Chemical Safety, Geneva World Health Organisation*, 125.

Williams, K. H., Bargar, J. R., Lloyd, J. R. & Lovley, D. R. (2013). ‘Bioremediation of uranium-contaminated groundwater: A systems approach to subsurface biogeochemistry’ *Current opinion in biotechnology*, 24 (3), pp. 489-497.

Wilson, S. C., Lockwood, P. V., Ashley, P. M. & Tighe, M. (2010). ‘The chemistry and behaviour of antimony in the soil environment with comparisons to arsenic: A critical review’ *Environmental pollution (1987)*, 158 (5), pp. 1169-1181. DOI: 10.1016/j.envpol.2009.10.045.

Xiao, Z. & Laplante, A. (2004). ‘Characterizing and recovering the platinum group minerals—a review’ *Minerals Engineering*, 17 (9-10), pp. 961-979.

Xiu, W., et al. (2021). ‘A critical review of abiotic and microbially-mediated chemical reduction rates of fe (iii)(oxyhydr) oxides using a reactivity model’ *Applied Geochemistry*, 126 p. 104895.

Yang, J., et al. (2016). ‘Bioimmobilization of heavy metals in acidic copper mine tailings soil’ *Geomicrobiology Journal*, 33 (3-4), pp. 261-266.

Yi, H. & Hai, W. (2005). ‘The application of bioremediation in heavy metals pollution treatment [j]’ *Chemistry*, 1 pp. 36-42.

Yousefi, S., Shemirani, F. & Jamali, M. (2010). ‘Determination of antimony (iii) and total antimony in aqueous samples by electrothermal atomic absorption spectrometry after dispersive liquid–liquid microextraction (dllme)’ *Analytical Letters*, 43 (16), pp. 2563-2571.

Zhu, N., et al. (2016). ‘Biorecovery of gold as nanoparticles and its catalytic activities for p-nitrophenol degradation’ *Environmental Science and Pollution Research*, 23 (8), pp. 7627-7638.

Zhu, Y.-G., Yoshinaga, M., Zhao, F.-J. & Rosen, B. P. (2014). ‘Earth abides arsenic biotransformations’ *Annual Review of Earth and Planetary Sciences*, 42 pp. 443-467.

Chapter 3. Methodology

In this chapter, the main experiment operations and analytical techniques for this project were described. The aim for this chapter is to provide some details about the research methods and the principles of the instruments used. The details and preparation methods of all stock solution used in this project were concluded in section 3.1. Section 3.2 included synthesis methods of all solid Fe minerals in this project. Section 3.3 covered all bioreduction and biorecovery processes, as well as the steps involved in *Geobacter sulfurreducens* culture. Chapter 3.4 and 3.5 respectively introduced the liquid and solid geochemical analysis methods and the principle and structure of the corresponding instruments. The last chapter 3.6 was about the experimental method of catalytic reduction of 4-NP experiments.

3.1 Stock solution preparation

The nutrient broth acetate-fumarate (NBAF) growth medium (1L) was prepared by following the recipe as follows: 0.42 g of KH_2PO_4, 0.22 g of K_2HPO_4, 0.2 g of NH_4Cl, 0.38 g of KCl, 0.36 g of NaCl, 0.04 g of $CaCl_2$ * $2H_2O$, 0.1 g of $MgSO_4$ * 7H2O, 1.8 g of $NaHCO_3$, 0.5 g of Na_2CO_3, 2.04 g of $NaC_2H_3O_2$ * $3H_2O$, 6.4 g of $Na_2C_4H_4O_4$, 1.0 ml of 100 mM Na_2SeO_4, 15.0 ml of a vitamin solution, and 10.0 ml of NB trace mineral solution (Coppi et al., 2001). The pH value of the NBAF medium was adjusted to around 7.0 by adding 10 M NaOH. Once mixed appropriately, the solution was flushed with 80:20 mix of N_2:CO_2 for 20 minutes

to remove O_2. The 1L mixed solution was then decanted to small bottles (100 ml) in an anaerobic cabinet and sealed with rubber stoppers and aluminium crimps. These bottles were autoclaved for 20 minutes at 126ºC (Ceron et al., 2006; Cerveró et al., 2010) and then stored in the dark before use.

The concentration and preparation methods of other solutions used in the experiments are listed in Table 3.1.

Table 3.1. Detailed compositional information of the solutions used in experiments

Stock solution	**Total volume**	**Medicament and preparation method**	**Purpose(s)**
30 mM sodium bicarbonate	1 L	Add 2.5203 g sodium bicarbonate into 1L DIW and adjust pH to around 6.8-7.0by 10M NaOH. Then the adjusted solution was flushed with 80:20 mix of N_2:CO_2 for around half hour to remove O_2 and keep the pH around 7.0.	Cell washing
1M sodium bicarbonate	50 mL	4.2005 g $NaHCO_3$ were added into 50 mL DIW and store airtight in refrigerator.	Bioreduction experiments setup
1M sodium acetate	50 mL	Add 4.1015 g sodium acetate into 50 mL DIW and store airtight in refrigerator.	Bioreduction experiments setup
6.25M hydroxylamine hydrochloride solution	1.6 mL	Add 0.6946 g hydroxylamine hydrochloride into 1.6 mL DIW. It should be mixed well before using, and prepared freshly for each use.	Ferrozine assay
Ferrozine solution	1 L	1 g Ferrozine powder (3-(2- Pyridyl)-5,6-diphenyl-1,2,4-triazine-p,p'-disulfonic	Ferrozine assay

		acid monosodium salt hydrate) and 11.96 g HEPES were dissolved by 1L DIW. Then, the pH of the solution was adjusted to around 7.0. store in the fridge for using.	
0.5M hydrochloric acid, HCl	~1 L	Add ~ 43 mL 37% HCl into 950ml DIW and mix well	Ferrozine assay
2% Nitric acid	1 L	Add 30 ml 70% HNO_3 into 970ml DIW and mix well	ICP sample preparation
5% Nitric acid	~10L	Slowly add 714 ml of water to the plastic container containing 9.3 L of DIW. Prepare acid bath every 2 months.	Acid bath
20mM Sb(V) stock solution	250 mL	1.3145 g Potassium hexahydroxoantimonate(V) ($KSb(OH)_6$ was added to 250 ml DIW. The Sb(V) stock solution was stored at 4 ºC in the dark before using.	Sb experiments
50 mM Pd(II) stock solution	10 mL	Weigh 0.1471 g of sodium tetrachloropalladate(II) Na_2PdCl_4, dissolve it in a small amount of water and transfer it to a 10 mL volumetric bottle with a constant volume of 10 ml. Store in the fridge away from light.	PGM experiments
50mM Pt(IV) stock solution	10 mL	Weigh 0.2269 g of sodium hexachlorplatinate Na_2PtCl_6, dissolve it in a small amount of water and transfer it to a 10 mL volumetric bottle with a constant volume of 10 ml. Store in the fridge away from light.	PGM experiments

50mM Rh(III) stock solution	10 mL	Weigh 0.1303 g of rhodium chloride hydrate $RhCl_3.XH_2O$ (39.5%), dissolve it in a small amount of water and transfer it to a 10 mL volumetric bottle with a constant volume of 10 ml. Store in the fridge away from light.	PGM experiments
50mM Ru(III) stock solution	10 mL	Weigh 0.1330 g of ruthenium chloride hydrate $RuCl_3.XH_2O$ (min 38%), dissolve it in a small amount of water and transfer it to a 10 mL volumetric bottle with a constant volume of 10 ml. Store in the fridge away from light.	PGM experiments

3.2 Mineral materials synthesis

3.2.1 Synthesis of the Ferrihydrite and Ce-bearing Ferrihydrite

Ferrihydrite (FeO(OH)) was prepared according to established methods (Byrne et al., 2011; Lovley and Phillips, 1986). Approximately 108 g of $FeCl_3.6H_2O$ (Sigma-Aldrich) was dissolved into 1 L deionized water. The solution was hydrolysed by adding 10M NaOH solution. The pH value of the initial solution was around 6.8-7.0 prior to precipitation, and the solid-liquid mixture was continually shaken for 1 hour with at constant pH. Precipitates were then centrifuged at 5000 *g* and 21 ºC to separate solids from the supernatant. An additional five washes were made with deionized water to remove any interfering ions.

To prepare samples for ICP-AES analysis, 0.1 ml sample of mineral slurry was added to 4.9 ml 37% HCl, and incubated for 30 minutes; the 0.1 ml of digest sample was then added to 9.9 ml 2% HNO_3 to prior to analysis. Final solutions were sampled and analysed by ICP-AES to test the concentration of iron and cerium in the initial precipitates. Precipitates were also dried in air and powdered for XRD analysis (details below).

For Ce-bearing ferrihydrite preparation, four different Ce-doped ferrihydrite minerals were prepared (0.5% 1% 2% & 5% molar ratio) from ferric chloride ($FeCl_3$) and cerium chloride ($CeCl_3$). The following hydrolysis and minerals washing steps are same to the preparation of pure ferrihydrite.

3.2.2 Sb(V) adsorbed ferrihydrite preparation

In Chapter 5 Sb(V) stock solutions were prepared. 0.25 ml, 0.5 ml,1 ml and 2.5 ml of 20 mM Sb(V) solution were added to 100 mL serum bottles which contained 10 mmoles $liter^{-1}$ slurry ferrihydrite, 30 mM sodium bicarbonate and 10 mM sodium acetate. A mixed gas of 80:20 (v/v) N_2 and CO_2 was used to flush all serum bottles for 30 minutes and maintain a stable pH around 7.0.

These bottles were subsequently stored at room temperature and samples were collected from them regularly to determine the concentration of residual Sb in the liquid phase during the adsorption process.

3.3 Biological reduction and recovery experiments

3.3.1 Cultivation of *Geobacter sulfurreducens*

This work was carried out in the Geomicrobiology lab in Department of Earth and Environmental Science (DEES). For *Geobacter sulfurreducens* inoculation (figure 3.1), around 10 ml of a fresh stationary phase culture was added to bottles containing 90 ml NBAF solution. These bottles were then incubated in a 30ºC incubator for around 2-3 days for use in the metal reduction experiments. Before use, the cultured bacteria were harvested from the growth medium by centrifuging at 5000 *g* and 4 ºC for 20 minutes. Next, the separated bacteria were washed twice in 30 mM bicarbonate buffer (pH 7 and flushed by mixed gases). Before each washing step, the bacterial suspension was flushed with 80:20 mix of N_2:CO_2 for 30 minutes to prevent oxygen from entering the suspension. After washing, the cells were resuspended in flushed 30 mM $NaHCO_3$ solution. The cell suspension was added to the test solutions in subsequent bioreduction experiments.

Figure 3.1 Left: NBAF media without cells; right: *Geobacter sulfurreducens* in NBAF enrichment medium.

3.3.2 Dissimilatory metal reduction experimental by *Geobacter sulfurreducens*

Before the addition of cells, bottles containing 10 mmoles liter^{-1} slurry ferrihydrite (metal-bearing) (Chapter 4&5) or 0.2 mM PGM (Chapter 6), 30 mM sodium bicarbonate and 10 mM sodium acetate, were all flushed with mixed gases to achieve anaerobic conditions and maintain a pH neutral environment. The washed *Geobacter sulfurreducens* was added to serum bottles to the equivalent final OD_{600} biomass of around 0.4. The bottles were then incubated at 30 ºC, and periodically sampled for testing.

3.4 Aqueous geochemical analyses

3.4.1 Monitoring experiments and Ferrozine assay

For the ferrihydrite experiments (Chapter 4&5), bottle tops were all sterilised with ethanol and flame (Bunsen burner) and handled using standard aseptic technique, to avoid contamination of the cultures. 1 ml nitrogen gas was

injected into the bottle before withdrawing samples to keep the air pressure balanced. After the bottles were shaken well, 1 ml of the slurry was sampled into empty Eppendorf tubes. After that, 0.1 ml of the sample was added to centrifuge tubes containing 4.9 ml 0.5M HCl for 1 hour reactions. The remaining slurry samples were centrifuged at 14,800 rpm (16,162 *g*) for 10 minutes. In the next step, 0.1 ml of the supernatant was sampled for ICP-AES/(MS) testing. After 1 hour, 200 µl of the slurry, which had been digested by 0.5 M HCl solution, was added to cuvettes that contained 2.3 ml of ferrozine solution, to quantify the concentration of Fe(II).

The ferrozine assay was used to measure the bioavailable iron concentration in samples. This assay is based on a colorimetric reaction of Fe(II) with ferrozine solution (Stookey, 1970). To measure the total bioavailable iron, hydroxylamine hydrochloride solution was used to reduce all Fe ions to Fe(II) (Newsome et al., 2014). However, the 'total bioavailable iron' does not necessarily mean the real concentration of the bioavailable iron in the samples, as it is an operationally-defined parameter (Lovley and Phillips, 1987; Newsome et al., 2014). The detecting instrument of this assay is a spectrophotometer. The sediment slurry was digested by 0.5 M HCl or 0.25 M hydroxylamine hydrochloride in 0.5 M HCl before measuring Fe(II) or total iron. After blanking the spectrophotometer against the ferrozine solution, the absorbance of the sample solutions was measured at 562 nm. 200 µl of the

hydroxylamine hydrochloride solution was also added to the sediment slurry centrifuge tubes to reduce all bioavailable iron ions to Fe(II) prior to measurement (1-hour treatment). For data analysis, the absorbance detected should be converted to concentration by a Fe(II) standard calibration curve. 0, 1, 2, 5, 10 and 20 mM Fe(II) standards (prepared by $FeSO_4 \cdot 7H_2O$) were used to calculate the Fe(II) standard calibration curve (see figure 3.2).

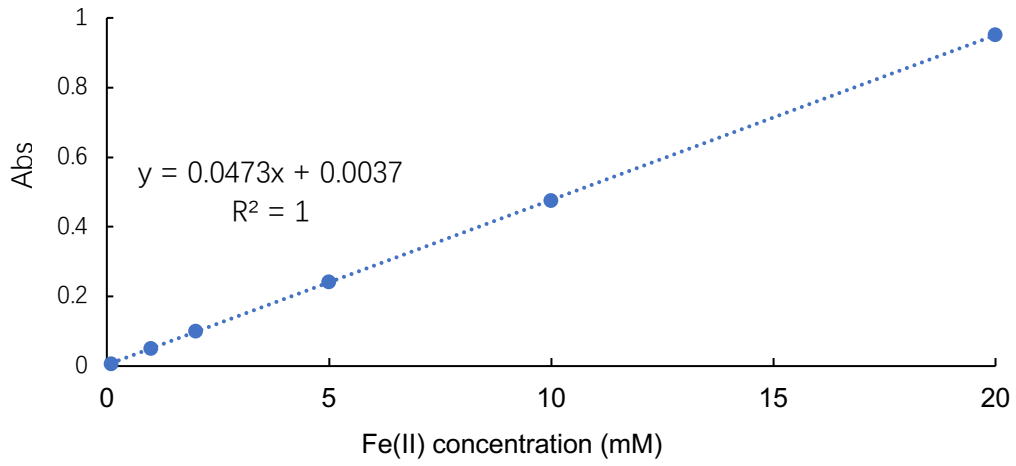

Figure 3.2 Fe(II) standard calibration curve for ferrozine assay. The equation is for Fe concentration calculation, X represents concentration and Y represents absorbance. R^2 =1 means the linearity of the standard curve is good.

3.4.2 pH and Eh

The pH and Eh parameters are both important indicators of the chemical conditions of the bioreduction experiments. The Eh value is a measure of the oxidation or reducibility of the solution. The higher the Eh value means the greater oxidation intensity. The pH value is a measure of how acidic or alkaline a solution is. A solution with a pH of 7 is neutral while a pH<7 is acidic, and a

pH>7 is alkaline. A Denver Instruments Fisher Scientific Accumet Basic pH/Eh meter was used to measure pH and Eh in the Geomicrobiology Lab in DEES. The Mettler Toledo InLab® Redox Micro probe and Fisherbrand FB58801 probe are appropriate for Eh and pH measurement, respectively. Before each measurement, the instruments need to be calibrated. Calibration of pH and Eh was carried out using pH 4, 7, 10 standard buffers and 220 mV standard solution, respectively.

3.4.3 Inductively-Coupled Plasma Atomic-Emission Spectroscopy (ICP-AES) and Inductively coupled plasma mass spectrometry (ICP-MS)

ICP-AES and ICP-MS were used to measure the concentration of the elements (Fe, Ce, Sb, Pd, Pt, Rh, Ru) in the supernatant. The atoms in samples are excited by ICP and consequently emit characteristic electromagnetic radiation. The AES and MS are detectors coupled to ICP, which can quantitatively measure the concentrations of specific elements (Beauchemin, 2008; Charles and Fredeen, 1997). The Perkin-Elmer Optima 5300 dual view ICP-AES and Agilent 8800 Triple Quadrupole ICP-MS of the Manchester Analytical Geochemistry Lab were used for the current project. ICP-AES was mainly used in the Ce experiments (Chapter 4), whereas ICP-MS was used for the bioreduction (Sb-ferrihydrite and PGM) experiments (Chapters 5 and 6, respectively).

As shown in figure 3.3, the ICP-AES system contains a nebulizer system, a plasma torch tube, an air supply system and the spectrometer. The injector sends the samples into the atomizer, and the argon carrier gas is used to carry the aerosol mist into the flame. At that moment, the components in the sample are atomized, ionized and excited, and emit energy in the form of light. When atoms of different elements return to the ground state after excitation or ionization, they emit characteristic spectra of different wavelengths (Hill, 2008). The ICP-AES results can be quantitatively analysed because the intensity of the emission light is dependent on the concentration of the element being analysed. Compared with ferrozine assay, the detection limit of ICP-AES is much lower, i.e., around 10-50 ppb.

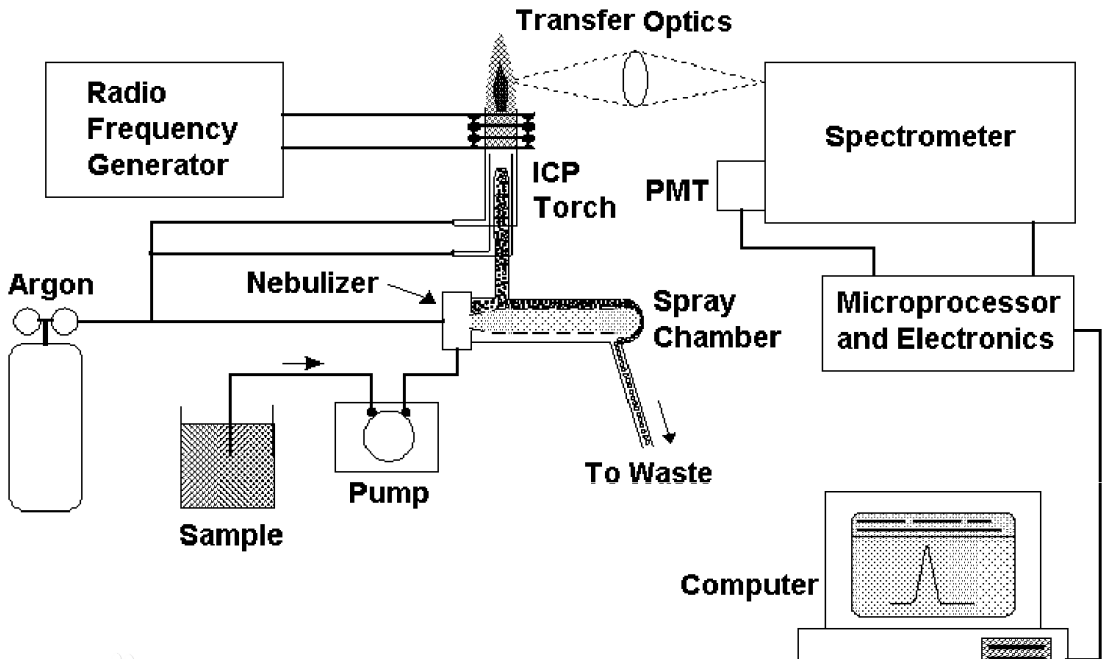

Figure 3.3 The structure of ICP-AES (Sneddon and Vincent, 2008)

ICP-MS differs from ICP-AES in that the detection of elements in aerosolized and ionized samples is based on mass spectrometry rather than photon

emission. Compared to ICP-AES, the main advantage of ICP-MS is the higher sensitivity of mass spectrometer-based techniques; the detection limits of ICP-MS can achieve parts per trillion (ppt) levels (Barin et al., 2016; Sneddon and Vincent, 2008).

The sample preparation for ICP-MS and ICP-AES was the same. Samples were centrifuged at 14,800 rpm (16,162 *g*) for 10-20 minutes, 0.1 ml of supernatant was added into 9.9 ml 2% HNO_3 and mixed well. All of the samples were stored in a cold room before analysis.

3.5 Solid-phase geochemistry

3.5.1 X-ray diffraction (XRD)

XRD was an important solid phase detection instrument and used in all three chapters. The diffraction pattern of crystalline mineral samples revealed by X-ray diffraction analysis can be used to obtain information on the structure of atoms and molecules within these materials. When an X-ray is projected into a crystal as an electromagnetic wave, it is scattered by atoms in the crystal. As the atoms are arranged periodically in the crystal, there is a fixed phase relationship between these scattered spherical waves, which leads to a strengthening of spherical waves in some scattering directions and self-cancellation in other directions, resulting in diffraction phenomenon. The basic principle of the XRD is Bragg's Law where $2d\sin\theta=n\lambda$ (λ and d represent the

wavelength of the X-rays and the spacing between the lattice planes of parallel crystals, respectively, and n represent an integer; (Le Bail et al., 2008; Waseda et al., 2011). Figure 3.4 shows the basic structure of XRD and light path during the XRD process.

In the current study, a Bruker D2 Phaser diffractometer, equipped with a Lynxeye XE-T detector, an axial 2.5º Soller slit, and anti-scatter screen was used with the angle of incidence θ varied to change the diffraction angles (2 θ) between 10° and 70° with a step size of 0.04°. The sample was rotated 380° during analysis to ensure all diffraction conditions were met. The XRD pattern can be input into the Scherrer formula to calculate the crystal size of nanoparticles (Byrne et al., 2011; Patterson, 1939), estimates that can in turn be compared with particle sizes calculated from TEM images. However, the Scherrer formula is not useful for crystal sizes larger than 200 nm. The Scherrer formula is shown below (Holzwarth and Gibson, 2011; Muniz et al., 2016):

$$D = K\lambda / B \cos\theta$$

(Where D is Crystal size; K is a constant usually 0.9; θ is the diffraction angle; λ is the X-ray wavelength [0.154 nm for CuKα1]; and B is the peak broadening in radians, which can be calculated by measuring the peak width at half the maximum intensity of a given diffraction peak in the XRD pattern and subtracting the instrumental broadening).

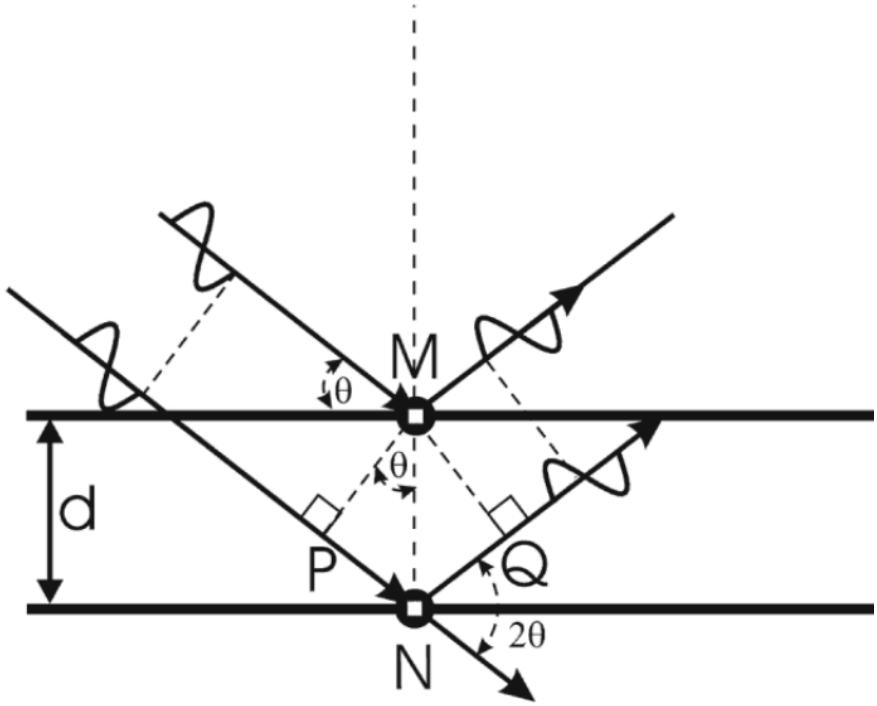

Figure 3.4 A diagram of the principal of Bragg's Law. Two beams of incident X-rays at the same wavelength are scattered by crystals at the distance between planes (d) (Le Bail et al., 2008)

Around 0.1 g of the relevant samples were taken and dried overnight in an anaerobic cabinet. The dried samples were ground by a pestle and mortar to fine powders and applied evenly to glass slides with isopropanol. The results were evaluated using the EVA version 5 software, which compares experimental data to standards from the ICDD (International Centre for Diffraction Data) Database.

3.5.2 X-ray absorption spectrum (XAS)

X-ray absorption spectroscopy (XAS) is a widely used technique for determining the local geometric and electronic structure of matter. An accelerated beam of high-energy electrons around the storage ring passes

through the electromagnet, producing X-rays which then pass through the samples of interest (Penner-Hahn, 2003). Based on the change in the incidence of the X-rays, the composition of samples, electronic valence of elements and microstructure of the samples can all be analysed. XAS samples can be solid, liquid or gas. In detail, an inner electron (usually in K or L shell) can absorb the X-ray when the energy of the X-ray is equal to the ionization energy of the electron. The electron will become a photoelectron after absorbing this energy. The photoelectron produced can then be emitted from the atom while the atom is in an unstable excited state. The minimum energy needed to produce a photoelectron is called the absorption edge of the element. Each element has a specific absorption edge, so XAS can be used in the qualitative analysis of elements.

The fine structure extends from the front of the absorption edge to the high energy segment about 1000 eV, and the whole spectrum is referred to as XAFS (X-Ray Absorption Fine Structure). According to their formation mechanism (multiple scattering and single scattering; figure 3.5), they can be divided into XANES (X-ray Absorption Near Edge Structure) and EXAFS (Extend X-ray Absorption Fine Structure). As figure 3.6 shows, the range of XANES is up to ~50 eV after the absorption edge and it is often used to identify the valence state of elements. The range of EXAFS is from 50 eV to 1,000 eV after the absorption edge. EXAFS can reveal information about the number of

backscattering atoms (i.e., coordination number), and the distance of the backscattering atoms from the central absorber (bond distance) (Newville, 2014). In this study, samples were dried in an anaerobic cabinet before being taken to the Diamond Light Source in Harwell (UK) for XAS testing.

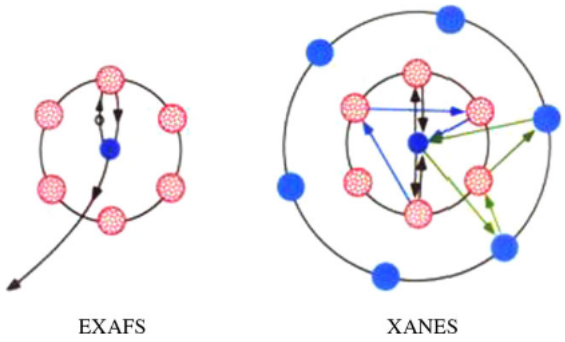

Figure 3.5. Schematic diagrams of multiple scattering and single scattering of the electron between a central atom and its surrounding atoms (Cheng et al., 2014)

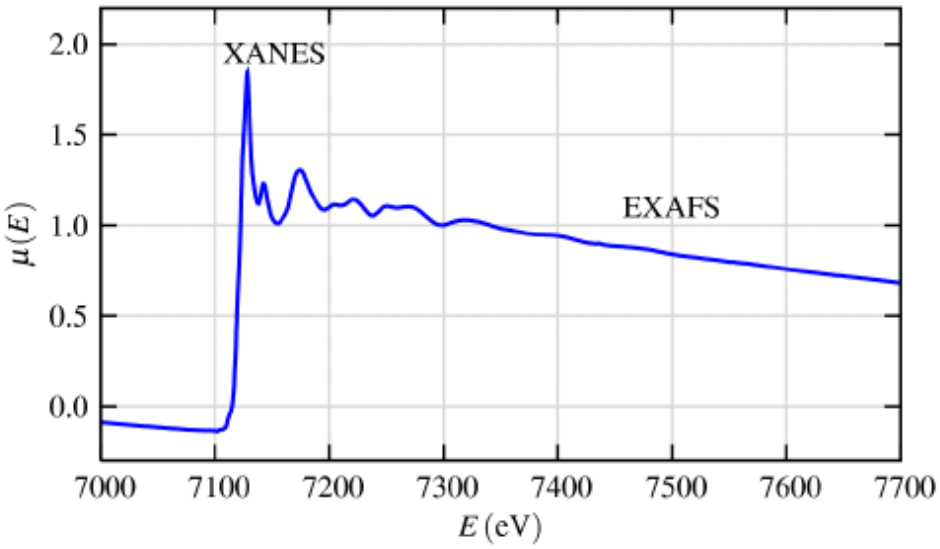

Figure 3.6 XAS spectrum example (XANES & EXAFS) (Newville, 2014)

3.5.3 X-ray magnetic circular dichroism (XMCD)

XMCD was used to identify the biomagnetite formed in Ce-ferrihydrite bioreduction experiments (Chapter 4). The XMCD spectra of Fe $L_{2,3}$-edge were

collected to measure the three potential Fe environments within magnetite (Fe^{2+} O_h, Fe^{3+} T_d and Fe^{3+} O_h) at the Advanced Light Source (ALS; Berkeley, USA) (Coker et al., 2007; Joshi et al., 2018). An XMCD spectrum is a differential spectrum of two XAS in the magnetic field. A pair of XAS were measured for the two opposite magnetisation directions set parallel and anti-parallel to the beam direction and then two XAS spectra are subtracted to get the XMCD spectra (Coker et al., 2006; Pattrick et al., 2002). In stoichiometric magnetite, the Fe occupancy of the d^6O_h: d^5T_d: d^5O_h site is 1:1:1 and Fe(III) is split to Oh and Td sites equally while Fe(II) only occurs in Oh sites. Therefore, XMCD can be used to detect the relative occupation of these sites, and then compare with standard magnetite to understand the change of each occupation under the influence of experimental conditions.

3.5.4 X-ray photoelectron spectroscopy (XPS)

X-ray photoelectron spectroscopy (XPS) is a surface analysis method that uses X-rays to irradiate samples so that the inner or valence electrons of atoms or molecules are ejected and was used to identify the valance states of Sb Pd, Pt and Rh in Chapter 5 and 6. The electrons excited by photons are called photoelectrons. The energy and number of photoelectrons can be measured to obtain the composition of the material. XPS is mainly used to determine the binding energy of electrons to identify the composition and valence states of the elements on the sample surface. The characteristics of XPS are that

photoelectrons come from the surface within 10 nm and thus only reveal the chemical information of the surface. In addition, XPS analysis have other advantages that it requires a small number of samples and is a non-destructive analysis technique (Moulder et al., 1992).

For the samples preparation, two XPS sample preparatory methods were used in this project. For the Ce and Sb experiments, the gendered minerals were first washed twice with DIW and then dried in an anaerobic chamber. The dried samples were then collected and ground into as uniform and fine-grained a powder as possible. The powder was then loaded onto a sample holder. For the PGM experiment, another sample treatment method was used, because the concentration and amount of the products was typically very small, and the dry grinding process would have caused sample loss. Similarly, the PGM sample was washed twice with deionized water, and the supernatant was removed as much as possible after the last centrifugation. The sediment was remixed in a small amount of water, and part of the suspension was removed and dripped onto a clean silicon wafer for anaerobic drying. The processed samples were then placed on a sample holder and mounted on a movable sample stage. An ultra-high vacuum is required before starting the run to minimize the decay of the emitted photoelectrons. A Mg Kα or Al Kα X-ray source is typically used and a monochromator illuminates selected areas of the sample. The scan range is usually 0-1000 eV, and multiple high-resolution

scans can be performed in the region of the target element with characteristic peaks to obtain better data (Moulder et al., 1992). The emitted photoelectrons are passed to an electron energy analyzer, which uses a hemispherical capacitor to analyze the kinetic energy (KE) of the photoelectrons, which depends on the photon energy (hv) and the electron binding energy (BE). Their relationship can be expressed by the formula: $KE=hv-BE-\phi_s$ (where ϕ_s is the spectrometer work function (Hofmann, 2012; Moulder et al., 1992). By measuring the kinetic energy of the emitted electrons, the electron binding energy is calculated, and the elements and their chemical states near the surface of the material are determined.

XPS spectra analyses and curve fitting were carried out using the CasaXPS software. To analyze the valence state of the target element, CasaXPS is employed to split the peaks and compare the results with a standard database (NIST XPS database). After the peak splitting process, the proportion of each valence state can also be estimated by the proportion of the area of each peak representing different valence state (see Figure 3.7).

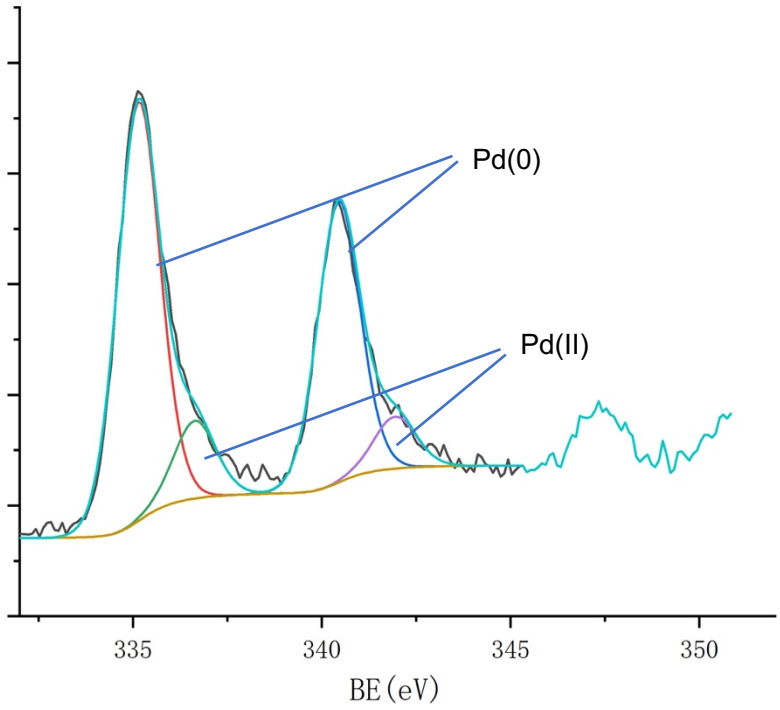

Figure 3.7 an XPS Pd 3d spectra of the bioreduction products of Pd(II) by Geobacter. Two sets of different Pd peaks (3d 3/2 and 3d 5/2) have been fitted and represent Pd(II) and Pd(0)

3.5.5 Transmission electron microscopy (TEM)

Transmission electron microscopy (TEM) was used to collect images of the bioreduction nanoparticles by *Geobacter sulfurreducens* in all three research chapters. Energy Dispersive X–ray Spectroscopy (EDS), a high angle annular dark field (HAADF) detector and electron diffraction patterns were also performed to test the composition and elements in the nanoparticle-bearing samples. A Scanning Transmission Electron Microscope (STEM, Thermo Fisher, Titan, G2 80–200) equipped with an EDS detector and HAADF detector operating with an inner angle of 55 mrad at 200 kV was used in the present work, and the electron diffraction patterns of the selected areas of samples

were obtained by Thermo Fisher Talos STEM. TEM analyses were performed by Dr. Rongshen Cai at the Electron Microscopy Centre of University of Manchester.

TEM is a high-resolution, high-magnification electron-optical instrument that uses a very short-wavelength electron beam emitted by an electron gun to focus and image with electromagnetic lenses in a vacuum (Hayat, 2012; Reimer, 2013; Williams and Carter, 1996). The accelerated and focused beam of electrons passes through the sample, before being refocused by a further electromagnetic lens, and finally onto a detector, usually a phosphor screen, semiconductor detector, or scintillator-photomultiplier tube system. In order to reduce the loss of the electron beam in the process of passing through the sample, the thickness of the TEM sample is usually not more than 100 nm (Hayat, 2012; Williams and Carter, 1996). For EDS, when the electron beam passes through the surface of the sample in a vacuum chamber, the excited substances emit characteristic X-rays, and the elements are characterised according to the wavelength of the characteristic X-rays.

Samples were first centrifuged at 5000*g* for 20 minutes, and then the separated precipitates were washed by DIW 3 times. The washed precipitates were resuspended in DIW and mixed well. The mixture was diluted 5 to 10 times until

nearly colourless, and drop-cast onto a copper grid coated with an amorphous carbon film.

3.6 Applications of the post reduction products

3.6.1 The catalytic reduction experiment of 4-nitrophenol by PGM nanoparticles

4-NP is an environmental contamination which can cause damage to the central nervous system, respiratory system, kidneys and liver of animals and humans (Nehru et al., 2020; Vilian et al., 2017). 62.5 mM $NaBH_4$ solution was used to reduce 4-NP to 4-AP with the PGM as catalysts. According to Ghosh et al.'s study, the reduction process cannot be conducted without catalysts, because E^0 for 4-NP/4-AP was around -0.76 V vs. standard hydrogen electrode (SHE) which is higher than that of H_3BO_3/BH_4^- (-1.33 V vs. SHE) (Ghosh et al., 2004). Thus, this reaction can be chosen for the test of the catalytic performance of different catalysts. UV-Vis was used to measure the concentration changes of 4-NP during the reduction processes. For example, Figure 3.8 represents the changes of 4-NP (absorbance) with time changing while using Pd(0) nanoparticles as the catalyst. The absorption peak at 400 nm is for 4-NP, the abundance of 4-NP peak decreased during the bioreduction processes, suggesting decomposition of 4-NP pollutant.

31.25 µL of 10 mM 4-nitrophenol solution and 1 mL of 62.5 mM $NaBH_4$ were mixed into a cuvette containing 1.97 mL of DIW. Then, 125 µL of washed bio-PGMs solution was pipetted into the above cuvette at room temperature. The cuvette holder was placed onto an orbital shaker at 100 rpm. A UV-Vis spectrophotometer (Bruker) was used to collect spectra during the reduction processes, in the range of 200-600nm at 0, 0.75, 1.5, 3, 5, 10, 20, 40, and 60 minutes.

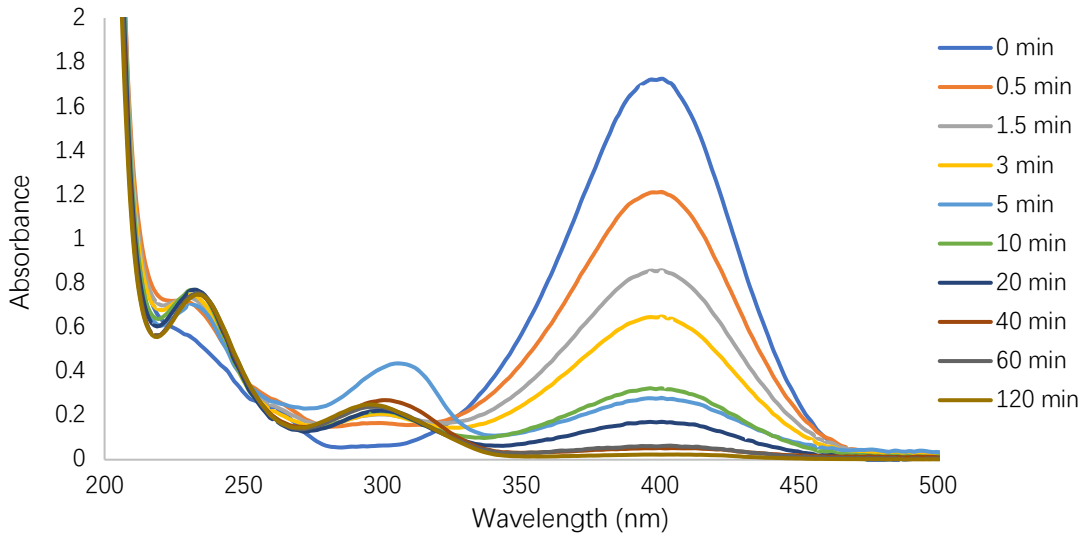

Figure 3.8 Time-dependent UV-vis spectra for the changes of 4-NP reductions while using Pd(0) nanoparticles catalysts.

3.6.2 Principal of electrochemical characterization for oxygen reduction reaction: the application of Ce doped magnetite in Pt/C catalyst for the cathode electrode

Cyclic voltammetry (CV) is commonly used to evaluate the electrochemical surface area (ECSA) of electrocatalysts through measuring the coulombic charge of hydrogen underpotential deposition (HUPD) in an acid electrolyte

system. The main process is that hydrogen ions ($H^+_{(aq)}$) in aqueous solution are adsorbed on the surface of the Pt sites with scanning towards a negative potential from 0 V to -0.2 V as shown below. With decreasing potential, the adsorption of H atoms ($H_{(ad)}$) increases meanwhile leads to more charge transfer in the solution. Then, the potential is reversed to the positive sweep and the desorption of hydrogen occurs to produce hydrogen desorption peak(Doña Rodríguez et al., 2000).

$$H^+_{(aq)} + e^- + site \leftrightharpoons H_{(ad)}$$

In the central potential region, the capacitive process takes place without electrochemical reactions. At higher positive potential region, platinum oxides are formed by hydration during the positive sweep. Then, they are reduced with the negative potential sweep(Doña Rodríguez et al., 2000).

ECSAs of catalysts were determined by integrating the hydrogen adsorption and desorption charge in the equation below(Seger and Kamat, 2009):

$$ECSAs = Q_h/(Q_m \cdot E.L)$$

Where, Q_h is the coulombic charge ($\mu C\ cm^{-2}$). Q_m is the adsorption charge for an atomically smooth surface, with a value for Pt of 210 $\mu C\ cm^{-2}$. E.L is the Pt loading on the electrode ($g\ cm^{-2}$).

Linear sweep voltammetry (LSV) has been used as a vital method for assessing oxygen reduction reaction (ORR) activity of electrocatalysts. The potential will scan in single direction with starting at high potential and stopping at low

potential. At higher potential, there is no reaction occurs. As the potential decrease, oxygen is reduced by the following reaction and produce negative current(Stephens et al., 2012).

$$O_2 + 4H^+ + 4e^- \rightarrow 2H_2O$$

The reaction rate is determined by the diffusion-limit of O_2 under different rotating rate and kinetics-limit. Generally, the diffusion-limit occurs at lower potential and restrict the reaction rate due to shortage of reactants(Stephens et al., 2012). Therefore, a diffusion-limiting current can be observed as little changes of current. For different catalysts under same rotating rate, higher diffusion-limiting current means higher activity of ORR (Wang et al., 2011). The onset potential (E_o) was defined as the potential at which the ORR starts, and the half wave potential ($E_{1/2}$) was defined as the potential at which the ORR current is 50% of the limiting current density.

References:

Barin, J. S., et al. (2016). 'Determination of elemental impurities in pharmaceutical products and related matrices by icp-based methods: A review' *Analytical and bioanalytical chemistry*, 408 (17), pp. 4547-4566.

Beauchemin, D. (2008). 'Inductively coupled plasma mass spectrometry' *Analytical chemistry*, 80 (12), pp. 4455-4486.

Byrne, J. M., et al. (2011). 'Control of nanoparticle size, reactivity and magnetic properties during the bioproduction of magnetite by *geobacter sulfurreducens*' *Nanotechnology*, 22 (45), p. 455709. DOI: 10.1088/0957-4484/22/45/455709.

Ceron, G. M., et al. (2006). 'Mixotrophic production of marine microalga phaeodactylum tricornutum on various carbon sources' *Journal of microbiology and biotechnology*, 16 (5), pp. 689-694.

Cerveró, J. M., et al. (2010). 'Enzymatic hydrolysis and fermentation of palm kernel press cake for production of bioethanol' *Enzyme and microbial technology*, 46 (3-4), pp. 177-184.

Charles, B. & Fredeen, K. J. (1997). 'Concepts, instrumentation and techniques in inductively coupled plasma optical emission spectrometry' *Perkin Elmer Corporation*, 3 p. 2.

Cheng, J., et al. (2014). 'An overview on the research of iron-based high-t c superconductors probed by x-ray absorption spectroscopy' *Journal of Superconductivity and Novel Magnetism*, 27 (1), pp. 9-15.

Coker, V., et al. (2006). 'Xas and xmcd evidence for species-dependent partitioning of arsenic during microbial reduction of ferrihydrite to magnetite' *Environmental science & technology*, 40 (24), pp. 7745-7750.

Coker, V. S., et al. (2007). 'Cation site occupancy of biogenic magnetite compared to polygenic ferrite spinels determined by x-ray magnetic circular dichroism' *European Journal of Mineralogy*, 19 (5), pp. 707-716.

Coppi, M. V., Leang, C., Sandler, S. J. & Lovley, D. R. (2001). 'Development of a genetic system for *geobacter sulfurreducens*' *Applied and environmental microbiology*, 67 (7), pp. 3180-3187.

Doña Rodríguez, J. M., Herrera Melián, J. A. & Pérez Peña, J. (2000). 'Determination of the real surface area of pt electrodes by hydrogen adsorption using cyclic voltammetry' *Journal of Chemical Education*, 77 (9). DOI: 10.1021/ed077p1195.

Ghosh, S. K., et al. (2004). 'Bimetallic pt–ni nanoparticles can catalyze reduction of aromatic nitro compounds by sodium borohydride in aqueous solution' *Applied Catalysis A: General*, 268 (1-2), pp. 61-66.

Hayat, M. (2012). *Basic techniques for transmission electron microscopy*. Elsevier.

Hill, S. J. (2008). *Inductively coupled plasma spectrometry and its applications*. John Wiley & Sons.

Hofmann, S. (2012). *Auger-and x-ray photoelectron spectroscopy in materials science: A user-oriented guide*. Springer Science & Business Media.

Holzwarth, U. & Gibson, N. (2011). 'The scherrer equation versus the'debye-scherrer equation'' *Nature nanotechnology*, 6 (9), pp. 534-534.

Joshi, N., et al. (2018). 'Microbial reduction of natural fe (iii) minerals; toward the sustainable production of functional magnetic nanoparticles' *Frontiers in Environmental Science*, 6 p. 127.

Le Bail, A., et al. (2008). *Powder diffraction: Theory and practice*. Royal society of chemistry.

Lovley, D. R. & Phillips, E. J. (1986). 'Availability of ferric iron for microbial reduction in bottom sediments of the freshwater tidal potomac river' *Applied and Environmental Microbiology*, 52 (4), pp. 751-757.

Lovley, D. R. & Phillips, E. J. (1987). 'Rapid assay for microbially reducible ferric iron in aquatic sediments' *Applied and Environmental Microbiology*, 53 (7), pp. 1536-1540.

Moulder, J. F., Stickle, W. F., E.'Sobol, P. & Bomben, K. D. (1992). 'Handbook of x-ray photoelectron spectroscopy' *Perkin-Elmer, USA*, p. 261.

Muniz, F. T. L., Miranda, M. R., Morilla dos Santos, C. & Sasaki, J. M. (2016). 'The scherrer equation and the dynamical theory of x-ray diffraction' *Acta Crystallographica Section A: Foundations and Advances*, 72 (3), pp. 385-390.

Nehru, R., Gopi, P. K. & Chen, S.-M. (2020). 'Enhanced sensing of hazardous 4-nitrophenol by a graphene oxide–tio 2 composite: Environmental pollutant monitoring applications' *New Journal of Chemistry*, 44 (11), pp. 4590-4603.

Newsome, L., et al. (2014). 'Microbial reduction of uranium (vi) in sediments of different lithologies collected from sellafield' *Applied geochemistry*, 51 pp. 55-64.

Newville, M. (2014). 'Fundamentals of xafs' *Reviews in Mineralogy and Geochemistry*, 78 (1), pp. 33-74.

Patterson, A. (1939). 'The scherrer formula for x-ray particle size determination' *Physical review*, 56 (10), p. 978.

Pattrick, R. A., et al. (2002). 'Cation site occupancy in spinel ferrites studied by x-ray magnetic circular dichroism: Developing a method for mineralogists' *European Journal of Mineralogy*, 14 (6), pp. 1095-1102.

Penner-Hahn, J. E. (2003). 'X-ray absorption spectroscopy' *Comprehensive Coordination Chemistry II*, 2 pp. 159-186.

Reimer, L. (2013). *Transmission electron microscopy: Physics of image formation and microanalysis*. Springer.

Seger, B. & Kamat, P. V. (2009). 'Electrocatalytically active graphene-platinum nanocomposites. Role of 2-d carbon support in pem fuel cells' *The Journal of Physical Chemistry C*, 113 (19), pp. 7990-7995. DOI: 10.1021/jp900360k.

Sneddon, J. & Vincent, M. D. (2008). 'Icp-oes and icp-ms for the determination of metals: Application to oysters' *Analytical letters*, 41 (8), pp. 1291-1303.

Stephens, I. E. L., et al. (2012). 'Understanding the electrocatalysis of oxygen reduction on platinum and its alloys' *Energy & Environmental Science*, 5 (5). DOI: 10.1039/c2ee03590a.

Stookey, L. L. (1970). 'Ferrozine---a new spectrophotometric reagent for iron' *Analytical chemistry*, 42 (7), pp. 779-781.

Vilian, A. E., et al. (2017). 'Pd nanospheres decorated reduced graphene oxide with multi-functions: Highly efficient catalytic reduction and ultrasensitive sensing of hazardous 4-nitrophenol pollutant' *Journal of hazardous materials*, 333 pp. 54-62.

Wang, S., et al. (2011). 'Polyelectrolyte-functionalized graphene as metal-free electrocatalysts for oxygen reduction' *ACS Nano*, 5 (8), pp. 6202-9. DOI: 10.1021/nn200879h Available at: https://www.ncbi.nlm.nih.gov/pubmed/21780760.

Waseda, Y., Matsubara, E. & Shinoda, K. (2011). *X-ray diffraction crystallography: Introduction, examples and solved problems*. Springer Science & Business Media.

Williams, D. B. & Carter, C. B. (1996). 'The transmission electron microscope', *Transmission electron microscopy*: Springer, pp. 3-17.

Chapter 4 :
Bioreduction of cerium-bearing ferrihydrite; a new route to carbon-black supported platinum catalysts

Jinxin Xie, ZiYu Zhao, Victoria S. Coker, Brian O'Driscoll, Rongsheng Cai, Sarah J. Haigh, Stuart M. Holmes, Jonathan R. Lloyd*

This chapter is a manuscript in preparation for the journal Environmental Science & Technology. Supporting information submitted with this manuscript is included in Appendix S4.

Chapter 4: Bioreduction of cerium-bearing ferrihydrite; a new route to carbon-black supported platinum catalysts

Jinxin Xie, ZiYu Zhao, Victoria S. Coker, Brian O'Driscoll, Rongsheng Cai, Sarah J. Haigh, Stuart M. Holmes, Jonathan R. Lloyd*

Abstract

There is much interest in the impact of biogeochemical processes on metals in the environment, and the potential for microbial cells to fabricate novel nanomaterials from waste metals through such processes. The research reported here focuses on the fate of Ce during the microbial reduction of Fe(III) minerals. Four different Ce bearing ferrihydrite minerals were prepared (0.5% 1% 2% & 5% molar ratios) from the co-precipitation of ferric chloride ($FeCl_3$) and cerium chloride ($CeCl_3$). Cerium K edge XANES analyses show that trivalent cerium and tetravalent cerium coexisted in the starting materials, with higher proportions of tetravalent cerium observed with increasing Ce content. The subsurface metal-reducing bacterium *Geobacter sulfurreducens* was used to reduce the Ce-bearing ferrihydrite substrates, forming the Fe(II)-bearing mineral magnetite (with small amounts of goethite also detected by XRD) in the presence of 0.5% and 1% Ce. At higher concentrations of Ce (2% and 5%), Fe(III) reduction was inhibited, and goethite dominated, with $CeCO_3$ minerals also detected. During microbial Fe(III) reduction, no Ce ions were released to solution, suggesting a tight coupling between Fe and Ce during redox cycling in environmental systems, even at extremely high Ce loadings. Fe $L_{2,3}$ XMCD spectra results suggest that Ce is partially incorporated into the Fe(III) containing sites of the magnetite. Commercial uses for the Ce-bearing bioreduced Fe minerals prepared in this study were also explored, focusing on use as a hydrogen fuel cell catalyst. Electrodes containing biomagnetite doped with 0.5% Ce showed better durability than conventional electrodes prepared with Pt, suggesting that bioprocessing of Ce-containing Fe(III) minerals (potentially from waste sources) offers a new route for the sustainable synthesis

of fuel cell catalysts.

4.1 Introduction

Cerium (Ce) is the most abundant of the rare earth elements (REE) in the Earth's crust, at bulk rock concentrations of approximately 0.0046% (Dahle and Arai, 2015; Sridharan and Menéndez, 2010). Cerium oxide is used widely in anthropogenic applications including as polishing materials, catalysts, ultraviolet absorbers, fuel cell electrolytes and automobile exhaust absorbers (Aneggi et al., 2020; Dahle and Arai, 2015; Frey et al., 2013; Lim et al., 2015). However, the mining and beneficiation of raw REEs have caused serious environmental challenges. Liu (2016) highlighted the paradox that some rare earth elements products are being used to build a clean, smart, low-carbon and climate-resilient future while simultaneously causing environmental damage. For example, in China, rare element mining and extraction have caused water pollution of the Pearl River Basin, which has severely affected local agriculture and fisheries (Liu, 2016; Ouyang et al., 2006). Moreover, in the region of Baotou City, where there are large REE reserves, cancer cases have been reported in villages and attributed to buried radioactive toxic REE mining wastes (Liu, 2016).

Unlike other REEs, that exist in only the trivalent state, Ce(III) may be converted to tetravalent cerium (Ce(IV)) under oxidizing conditions in surface environments. Ce(III) oxidation to Ce(IV) in the soil environment is closely

related to dissolution/precipitation processes during weathering (Janots et al., 2015). In addition, Ce(IV) is adsorbed more readily to bacteria or soils in natural environments than other trivalent rare earth elements (Ohnuki et al., 2008). Although Ce can exist in two oxidation states in the environment, most work on microbe-Ce interactions have focused on sorption of Ce(III) to biomass (biosorption) (Nancharaiah et al., 2016). Anders (2003) carried out REE biosorption experiments to a range of microorganisms. The results of their study showed that the adsorption capacity of a range of bacteria varies greatly (2 to 1000 µmol/g biomass), with carboxylic or phosphate functions in the cell wall implicated in sorption of REE cations (Andres et al., 2003). Ohnuki *et al*. (2015) conducted experiments to compare the sorption of Ce(III) to synthetic Mn(IV) oxides and the soil bacterium *Pseudomonas fluorescens.* Both Mn(IV) oxides and *Pseudomonas fluorescens* had the ability to remove Ce(III) ions from solution, with the oxidation of Ce(III) associated with Mn(IV) oxides but not the bacterial cells. The results of Ohnuki *et al*. (2015) also showed that the adsorbed Ce(III) on the cell surface reacts with P released from the cell to form Ce(III) phosphate nano-particles, and these nano-particles inhibited the oxidation of Ce(III) to Ce(IV) (Ohnuki et al., 2015). Furthermore, Garcia (2012) conducted experiments to investigate the effect of cerium oxide (CeO_2) on a mixed wastewater treatment microbial community (including heterotrophic and ammonia-oxidizing bacteria). Anaerobic experiments were performed in 1000 mL gas- tight reactors with a pressure transducer to monitor biogas production.

The results showed that cerium oxide nanoparticles caused nearly 100% inhibition in biogas production (García et al., 2012). Cerium oxide and magnetite are both catalysis of fuel cell electrodes, so using bioreduction processes to produce Ce(IV)-bearing magnetite is a worthwhile process to explore because of the potential applications for fuel cell electrodes (Liu et al., 2018; Takahashi et al., 2007) .

Dissimilatory metal-reducing bacteria (DMRB) can conserve energy for growth by coupling the oxidation of organic matter to the reduction of high oxidation state metals and metalloids, often altering their solubility (Lloyd, 2003). For example, under anaerobic conditions, a wide range of metals such as Cu(II), U(VI), Pd(II), Ag(I) and Au(III) are bioreduced and can be precipitated as extracellular or intracellular metallic nanoparticles via these respiratory processes (Joshi et al., 2018; Kimber et al., 2018; Lloyd, 2003; Natarajan and Ting, 2015; Zhu et al., 2016). Through the process of dissimilatory metal reduction, some minerals containing metallic elements can be transformed into new mineral phases; for example, *Shewanella oneidensis* can reduce Fe(III) in smectite, which results in a structural change in the smectite and the formation of illite in ~2 weeks (Kim et al., 2004). In addition, Fe(III)-reducing bacteria, such as *Geobacter sulfurreducens* and *Shewanella oneidensis,* can also reduce poorly crystalline Fe(III) minerals using organic matter as an electron doner, producing Fe(II)-bearing minerals such as magnetite, siderite or vivianite (Lloyd,

2003; Lovley et al., 1993; Lovley and Phillips, 1987). During the latter process, Fe(III) in the ferrihydrite is initially reduced to generate soluble Fe(II) ions, which then combine with the Fe(III) mineral to form magnetite under optimized conditions (Byrne et al., 2015; Coker et al., 2006; Cutting et al., 2012; Lovley et al., 1987).

Previous work has studied the fate of metal ions associated with Fe(III)-oxyhydroxides (which have a high surface area and high sorption capabilities) during the process of dissimilatory metal reduction. In several cases, the contaminant metals such as Cr and Tc, are incorporated into the newly formed inverse spinel structure of magnetite, altering the physical/chemical properties of the mineral (Byrne et al., 2013; Cutting et al., 2010; Kimber et al., 2018). Although dissimilatory metal reduction of Fe(III)-oxyhydroxides, such as ferrihydrite, by Fe(III)-reducing bacteria has been well studied (Coker et al., 2007), the geochemistry of cerium associated with iron minerals is mainly limited to adsorption studies (Nancharaiah et al., 2016), and the impact of Ce on Fe(III) mineral bioreduction, as well as associated final products, remain poorly understood. Cerium oxide and magnetite are both catalysts of fuel cell electrodes, so using bioreduction processes to produce Ce(IV)-bearing magnetite is a worthwhile process to explore because of the potential applications for fuel cell electrodes (Liu et al., 2018; Takahashi et al., 2007) .

This study focuses on the bioreduction of Ce-bearing ferrihydrite by *Geobacter sulfurreducens* in order to identify the fate of this REE in Fe-rich environmental systems undergoing redox transformations. It also explores the feasibility of biosynthesising Ce-bearing magnetite, which could be a potential new catalyst for fuel cell electrodes. Experiments with different initial cerium concentrations were used to study whether the REE influences the biological process, including exploring the final site occupancy of Ce in biomagnetite. The relevance of our results to the environmental fate of the REEs, and the potential to harness this system for REE bioprocessing to produce novel Fe-based mineral nanoparticles, are discussed. In addition, low Ce-bearing bioreduction products were tested as carbon-black-supported platinum catalysts, offering several advantages over commercially available alternatives.

4.2 Materials and Methods

4.2.1 Cultivation of *Geobacter sulfurreducens*

NBAF growth medium (pH 7.0) was prepared as described previously (Coppi et al., 2001) and decanted to 100 ml serum bottles, flushed with 80:20 mix of N_2:CO_2 for 20 minutes to remove oxygen and sealed with butyl rubber stoppers. The bottles were then autoclaved for 20 minutes at 126ºC and stored in the dark before use. A 10 ml aliquoted of a fresh stationary phase culture of *Geobacter sulfurreducens* was added to the bottles (which contained 90 ml NBAF medium). The bottles were incubated at 30ºC until the cultures had

reached late exponential phase and then harvested for use by centrifuging at 5000 *g* and 4 ºC, for 20 minutes. The cells were then washed twice in 30 mM bicarbonate buffer (pH 7) under an 80:20 mix of N_2: CO_2 .

4.2.2 Synthesis of Ce bearing Ferrihydrite

Four different Ce-bearing ferrihydrite preparations were synthesised (0.5% 1% 2% and 5% molar ratio of Ce) from ferric chloride ($FeCl_3$) and cerium chloride ($CeCl_3$) stock solutions. The solutions were hydrolysed and precipitated by adding 10M NaOH solution to pH 6.8-7.0, and the solid-liquid mixture was continually shaken for 1 hour maintaining a constant pH value. The mixture was then centrifuged at 5000 *g* and at room temperature to separate solid precipitate from the supernatant, which was discarded. An additional five washes were performed with deionized water to remove excess chloride ions. The precipitate was then stored as a suspension in deionised water at 4^{o}C. ICP-AES was used to measure the concentration of total Fe and Ce in the samples, and precipitates were also dried in air and powdered for analysis by X-ray diffraction (XRD; see section 4.2.5 for details).

4.2.3 Microbial reduction of Ce-bearing ferrihydrite

Washed suspensions of *Geobacter sulfurreducens* cells were added to 30 mM sodium bicarbonate solution, supplemented with Ce bearing ferrihydrite (10 mmoles liter^{-1} slurry) and 10 mM sodium acetate as an electron donor. Biomass

loadings were equivalent a final OD_{600} value of 0.4. The resting cell cultures were incubated under an atmosphere of N_2 and CO_2 (80:20) at 30ºC. To measure the bioavailable Fe(II) generated, The Ferrozine assay was used to monitor the production of Fe(II) over time (Lovley and Phillips, 1987; Newsome et al., 2014).

4.2.4 Synthesis of catalysts

Pt/ carbon black (CB) supported catalysts were synthesized in an autoclave by a modified polyol reduction method (Dong et al., 2010; Ji et al., 2021) for comparison to biogenic nanomaterials. Magnetite and 0.5% Ce bearing magnetite were prepared through the bioreduction of ferrihydrite and 0.5% Ce bearing ferrihydrite by *Geobacter sulfurreducens*. Fe-Pt/ CB and 0.5%Ce-Fe-Pt/CB supported catalysts was synthesized, by sonicating 50 mg of CB in 5 mL deionised water for 30 mins to yield a fully dispersed solution. 166.7 mg chloroplatinic acid hexahydrate ($H_2PtCl_6 \cdot 6H_2O$) and 12.5 mg magnetite (or Ce-bearing biomagnetite) were added to 20 mL ethylene glycol (EG) to achieve a final 1:5 ratio of Fe and Pt. Then, the mixed solution was mixed with the CB dispersed solution and sonicated for another 2 hrs and stirred for 1 h. Afterwards, the uniform dispersed solution was transferred into a Teflon-steel autoclave to carry out the hydrothermal reduction process at 120 ℃ for 24 hours in the oven. After cooling to room temperature, the catalyst solution was filtered under vacuum and washed with ethanol and deionised water to remove

all residues (e.g., chlorides and solvent). Finally, the catalyst was dried in a vacuum oven at 60 ℃ overnight and stored at room temperature. Similarly, Pt/CB was also synthesized by the same process using 200 mg $H_2PtCl_6 \cdot 6H_2O$.

4.2.5 Geochemical and mineralogical analysis

Inductively Coupled Plasma Atomic Emission Spectroscopy (ICP-AES) was used to measure the concentrations of iron and cerium using a Perkin Elmer Optima 5300 dual view instrument. Starting materials were analysed by removing 0.1 ml sample of mineral slurry, which was then added to 4.9 ml 37% HCl and incubated for 30 minutes, and then 0.1 ml of this digest was added to 9.9 ml 2% HNO_3, prior to analysis using ICP-AES for total Fe and Ce. For routine monitoring, supernatants of samples were analysed for Fe and Ce by ICP-AES. 1 ml slurry samples were taken from microbial incubations and centrifuged at 14,800 rpm (16,162 *g*) for 10 minutes, and then 0.1 ml of the supernatant was added to 9.9 ml 2% HNO_3, prior to analysis.

A Bruker D8 system, operating at 40 kV/40 mA, with Cu Kα1 radiation (λ=1.5406) was used for X-ray diffraction (XRD) analyses of solid samples. The angle of incidence (θ) was varied to change the diffraction angles (2θ) between 5° and 70°, with a step size of 0.02°, and the sample was rotated 360° to ensure all diffraction conditions were met (Byrne et al., 2013). Samples were ground to a uniform fine powder and then mounted on glass slides with amyl acetate. XRD

data analysis (background subtraction and peak identification) was performed by Diffrac. EVA with the International Centre for Diffraction Data (ICDD) Powder Diffraction Database.

X-ray absorption near edge structure (XANES) characterization of solid materials was performed at the Ce L_3-edge of samples to determine oxidation state. 1 ml slurry was taken and centrifuged. Then the supernatant was discarded, and the sediment was resuspended in 1 ml DIW. After washing twice, 0.5 ml of slurry was air dried overnight, and then put onto a layer of Kapton tape. These tapes were then mounted on to an aluminium sample holder. XANES data for the starting materials were collected at room temperature at the Ce L_3-edge (≈5727eV) on beamline B18 at the Diamond Light Source. The Athena software was used to process the XANES raw data.

XAS and X-ray magnetic circular dichroism (XMCD) spectra at the Fe $L_{2,3}$-edge were collected at the Advanced Light Source (ALS; Berkeley, USA) to measure the relative occupation of the three Fe ion sites within the magnetite structure (Coker et al., 2007; Joshi et al., 2018). XAS data were collected in total-electron yield (TEY) mode, which gives an effective probing depth of ~4.5 nm. At each energy point, the XAS were measured for the two opposite magnetisation directions set parallel and anti-parallel to the beam direction with a magnetic field strength of 0.6 Tesla. The XMCD spectrum were made via subtracting two

normalised XAS spectra of different magnetisation directions (Pattrick et al., 2002). XMCD data and standards were fitted using the Qfit software. According to previous research, there are three main peaks in the Fe L_3-edge XMCD of magnetite, which are negative, positive, negative respectively (Coker et al., 2006). Samples were freeze-dried first, and then ground to powders in an anaerobic cabinet before loading onto carbon tape.

Scanning Transmission Electron Microscopy (STEM, Thermo Fisher, Titan, G2 80–200) was used to collect observations on the morphology and structure of the Ce-bearing Fe minerals. The STEM is equipped with an Energy Dispersive X–ray Spectroscopy (EDS) detector and a high angle annular dark field (HAADF) detector. The operating conditions were set at an inner angle of 55 mrad at 200 kV. The distribution of different elements (Fe, Ce, O) in the post reduction products were characterized by EDS mapping in STEM mode. Electron diffraction patterns were collected using a Thermo Fisher Talos STEM on the chosen areas. For STEM sample preparation, the post reduction minerals were washed three times anaerobically using DIW and then drop-cast onto an amorphous carbon film coated copper TEM grid.

Electrochemical surface area (ECSA) and oxygen reduction reaction (ORR) activity were measured by cyclic voltammetry (CV) and linear sweep voltammetry (LSV), respectively. A conventional three electrode system was

used, with an electrolyte solution of 0.5 M H_2SO_4, the counter electrode (platinum wire) and the reference electrode (Ag/AgCl), whilst a glassy carbon rotating disk electrode was used as the working electrode covered by catalysts. 5 mg of catalyst was dispersed in a mixture of 0.95 ml ethanol and 0.05 ml Nafion solution (5 wt.%), following sonication for 1 h. Samples of catalyst suspension (20 µl) were dropped on to the glassy carbon rotating disk electrode. CVs were performed under a nitrogen-saturated atmosphere with a potential scan rate of 50 mV s^{-1} from -0.2 to 1.0 V, rotating at a rate of 1600 rpm(Beltrán-Gastélum et al., 2019). LSV testing was performed under an oxygen-saturated atmosphere with a scan rate of 20 mV s^{-1} from 1.0 to 0 V(Beltrán-Gastélum et al., 2019; Seger and Kamat, 2009). The accelerated stress test (AST) was used to estimate the durability of catalysts for oxygen reduction reaction under oxygen saturated 0.5M H_2SO_4 solution. Cyclic voltammetry was performed with a scan rate of 100 mV s^{-1} between 0.6 to 1.0 V to accelerate the degradation of catalysts. After 30000 cycles, the ECSA and ORR activity were tested again to estimate any changes to quantify the long-term stability and catalyst activity of the catalysts.

4.3 Results and discussion

4.3.1 Synthesis and characterisation of Ce bearing ferrihydrite

Ferrihydrite was prepared with different target concentrations of Ce (0.5% 1% 2% and 5% molar ratio) to investigate the fate of cerium in Fe(III)-bioreducing

systems, and determine whether cerium can affect microbial reduction of Fe(III) minerals. This was achieved by adding $CeCl_3$ to and $FeCl_3$ solution in the proportion of 0.5%, 1%, 2% and 5% (molar ratio) during hydrolysis by 10M NaOH. However, after coprecipitation and the mineral washing process, a proportion of the Ce and Fe was lost yielding 0.23%, 0.49%, 1.43% and 4.17%, Ce in the ferrihydrite.

XRD analyses of the Ce(III)-doped starting materials confirmed the presence of poorly crystalline ferrihydrite (Figure 4.1), with broad peaks at 35° and 62° 2θ. However, no changes were observed when Ce was added, and notably there was no evidence for the formation of crystalline cerium(IV) oxide by XRD analysis, even at the higher loadings added (although such products may have been below the level of detection by XRD).

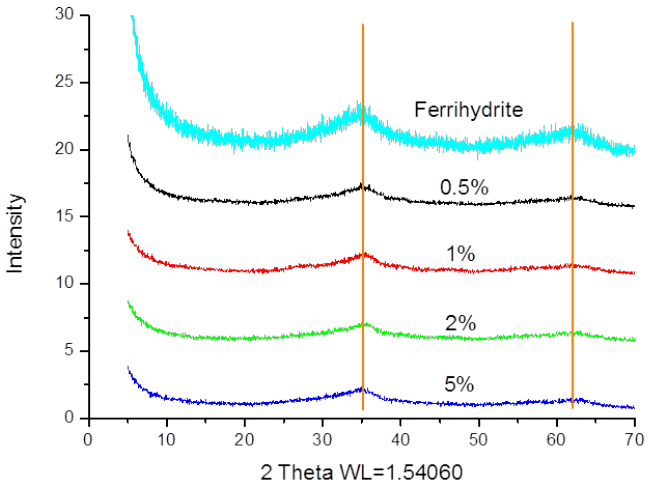

Figure 4.1 XRD results obtained from Ce bearing ferrihydrite with different Ce concentrations (0%, 0.5%, 1%, 2% and 5% molar ratio of Ce: Fe)

In contrast Ce *K-edge* XANES analysis suggested the presence of both Ce(III)

and Ce(IV) in the samples, with progressively more Ce(IV) at higher loadings of cerium (Figure 4.2) when compared to a Ce(IV)/MnO_2 standard (apparent from an increased peak height at 5738 eV). A possible explanation for this could be that a proportion of the $Ce(OH)_3$ was oxidized to $Ce(OH)_4$ by air during the washing process. In weakly acidic or alkaline solution, Ce(III) can be oxidized to Ce(IV), reaching 97% Ce(IV) hydroxide under optimal conditions (Zou et al., 2014).

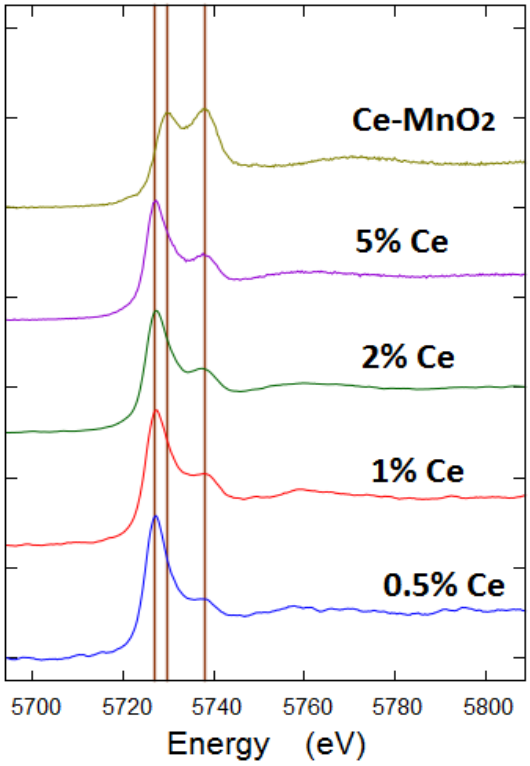

Figure 4.2 Normalized Ce K edge XANES of different concentration of Ce bearing ferrihydrite, Ce-MnO_2 which was used as Ce(IV) standard

4.3.2 The bioreduction of Ce-bearing ferrihydrite

Microbial reduction of ferrihydrite resulted in the accumulation of Fe(II) (Figure 4.3). Ce added to 0.5%, 1% and 2% had negligible impact on the rate and extent of Fe(III) reduction by cells of *G. sulfurreducens*. In these treatments

Fe(II) (measured by ferrozine) reached approximately 1.5–1.8 mmoles liter^{-1} slurry after 20 hours of incubation, which was similar to the results noted in Ce-free ferrihydrite (Figure 4.3). Although there was a further gradual increase in Fe(II) measured in some of these treatments of over longer periods time (e.g. to a maximum of 2.2 and 2.4 mmoles liter^{-1} slurry in the 0.5% and 1% samples, respectively) the Fe(II) levels did exceed 25% of the total Fe(III) added to the system. A black magnetic mineral formed in 0.5% and 1% Ce bearing samples treatments, consistent with the conversion of ferrihydrite to magnetite(Coker et al., 2006), although this formed more quickly (1 day) in the no Ce ferrihydrite incubations, compared to the Ce-bearing systems (2 days).

In contrast, at 5% added Ce, Fe(II) formation was significantly lower, reaching a maximum of 1.0 mmoles liter^{-1}after 45 hours, and in 2% and 5% Ce samples, the end-point mineral remained orange and non-magnetic. These results suggest that Ce has less impact on the rate and extent of iron reduction at the lower Ce levels, but at the higher loading tests (2% and 5%) the REE significantly impacted on the microbial process. Fe(II) did not accumulate in cell-free control experiments, confirming a role for the microbial electron transfer in the reduction processes reported here. According to ICP-AES results (not show here), no Ce ions was released to solution for all samples during the bioreduction processes, indicating that the microbial reduction of ferrihydrite by *G. sulfurreducens* does not mobilise Ce ions associated the Fe mineral.

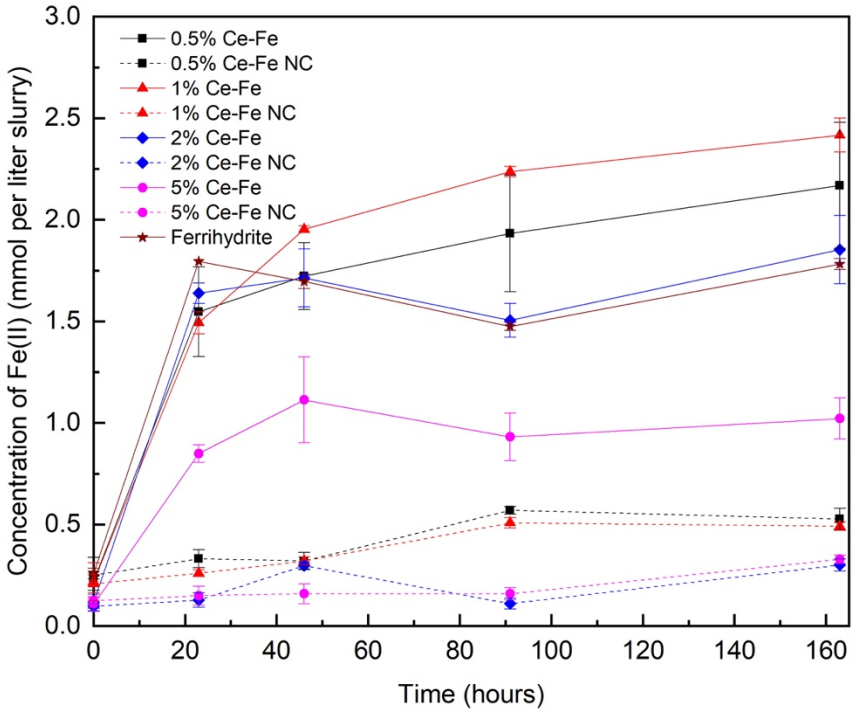

Figure 4.3 Changes of Fe(II) concentration of 0.5% 1% 2% & 5% Ce bearing samples. (averages of triplicate incubations, each sample also measured in triplicate); NC means no cell control samples

4.3.3 Characterisation of the secondary Fe minerals

Post reduction products were analysed by XRD after exposure to *G.sulfurreducens* (Figure 4.4). The XRD results were in good agreement with the magnetic properties of the products detected during the experiment. Comparing the traces for the post-reduction products to the biomagnetite standard, magnetite was present in both low-Ce bearing samples (0.5% and 1%). However, although the products of the 1% Ce-bearing sample contained magnetite, the composition of the product was not homogeneous. The XRD data showed characteristic peaks at around 22, 34, 36, 54 and 57 2-theta, suggesting a significant proportion of goethite. For the high Ce-bearing samples

(2% and 5%), goethite was the only Fe-bearing mineral in the post reduction products. With an increase in Ce content, the biomagnetite crystallites produced were progressively smaller, up to Ce contents of ~2%, which resulted in an apparent absence of biomagnetite in the experimental products. Furthermore, cerium(III) carbonate octahydrate was observed in the products of the 2% and 5% Ce-bearing samples. It is possible that during the bioreduction process, some Ce(III) was released from the initial material and combined with carbonate ions from the buffer. However, based on the ICP-AES data collected over the whole bioreduction process (7 days), the concentration of Ce in the solution was below the detect limits of ICP-AES which indicated that Ce in Fe minerals was not released into the solution during the reaction process.

In addition, the crystallite sizes of pure biomagnetite, 0.5% Ce-bearing and 1% Ce-bearing magnetite were around 37 nm, 20 nm and 11 nm, respectively (calculated from the XRD data using the Scherrer equation) (Byrne et al., 2013; Patterson, 1939; Zhu et al., 2009). The large crystallite size and needle-like morphology of goethite preclude precise calculation of its crystallite size using this method. Overall, our results indicate that the Ce concentration in the initial materials not only affects the composition of the biological products but may also affect biomagnetite crystallite size.

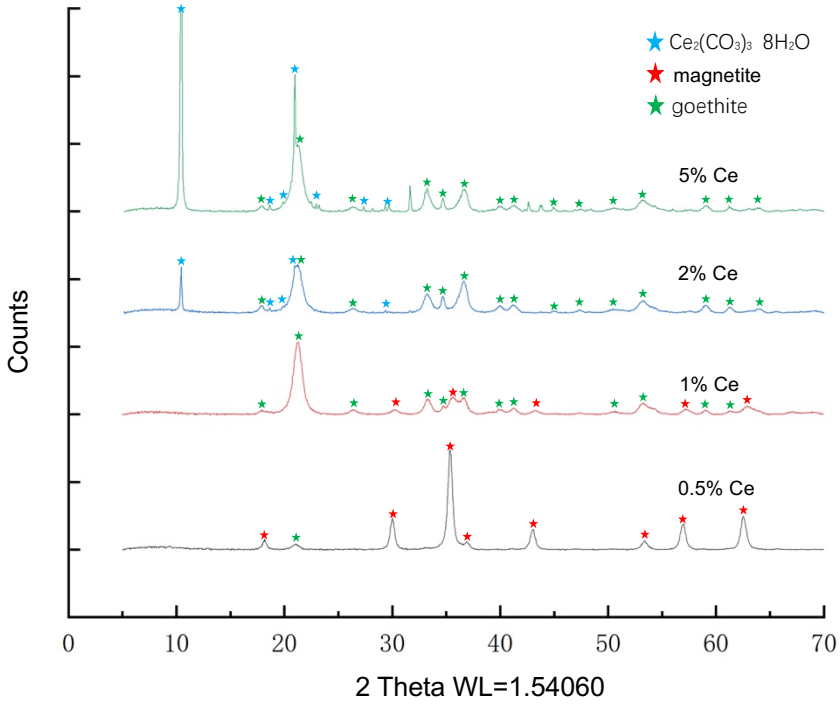

Figure 4.4 XRD results of post reduction of samples with different proportions of Ce bearing (0.5%,1%,2% and 5%)

The TEM images and diffraction results (Figure 4.5) were consistent with the XRD data, with magnetite only present in the low Ce-bearing samples (0.5% and 1%), while goethite was detected in the higher Ce-bearing samples. The 1% Ce-bearing products contained both rounded and needle-like products, and the diffraction results show both magnetite reflections and goethite (2 1 2) and (2 0 0) reflections (marked by red spots and highlighted in Figure 4.5), consistent with identification of these minerals by XRD. In addition, according to the TEM images (Figure 4.5), the sizes of the magnetite nanoparticles formed in the 0.5% and 1% Ce-bearing samples were 19.15 nm (SD=3.14nm) and 9.61 nm (SD=2.41nm), respectively, similar to the crystallite size (~20 nm and 11 nm) calculated using the XRD results. Goethite was also formed in the bioreduction products of the 1%, 2% and 5% Ce-bearing samples. The average width of the

formed goethite was similar in all of the latter samples, at around 7-8 nm. In the products of the 2% and 5% Ce-bearing samples, the length of the generated goethite was similar to about 140 nm, but in comparison, the length of the goethite produced in the 1% Ce-bearing sample was slightly smaller, at about 90 nm. These results confirmed that the cerium concentration of the initial product affected the size of the crystallite products.

However, there were also some discrepancies between the results from the two methods. According to XRD results, a small goethite (1 1 0) reflection was present in the products of the 0.5% Ce-bearing samples, but the TEM results showed that the products are pure magnetite. In the 2% Ce-bearing samples, only goethite present in TEM images, while the associated XRD spectrum showed a small reflection of $Ce_2(CO_3)_3$. These observations might be due to the missing product in either case being fine-grained and/or sporadically distributed. Relatively large Ce-bearing crystallites were present in the products of the 5% Ce-bearing sample, possibly corresponding to the cerium(III) carbonate octahydrate observed in the XRD results. However, based on the TEM EDS mapping and ESEM-EDS results (Figure S4.1 and S4.2), there were large (Fe-Ce-C-O-bearing) crystallites in the product, for which the TEM diffraction results suggested that the particle was a crystal of a single phase. This may reflect the presence of a carbonate compound containing Ce and Fe, with a similar crystal structure to cerium(III) carbonate octahydrate. Indeed, the

TEM EDS mapping results (Figure S4.1) indicated that Ce distribution was closely spatially associated with Fe-bearing minerals in all bioreduction products.

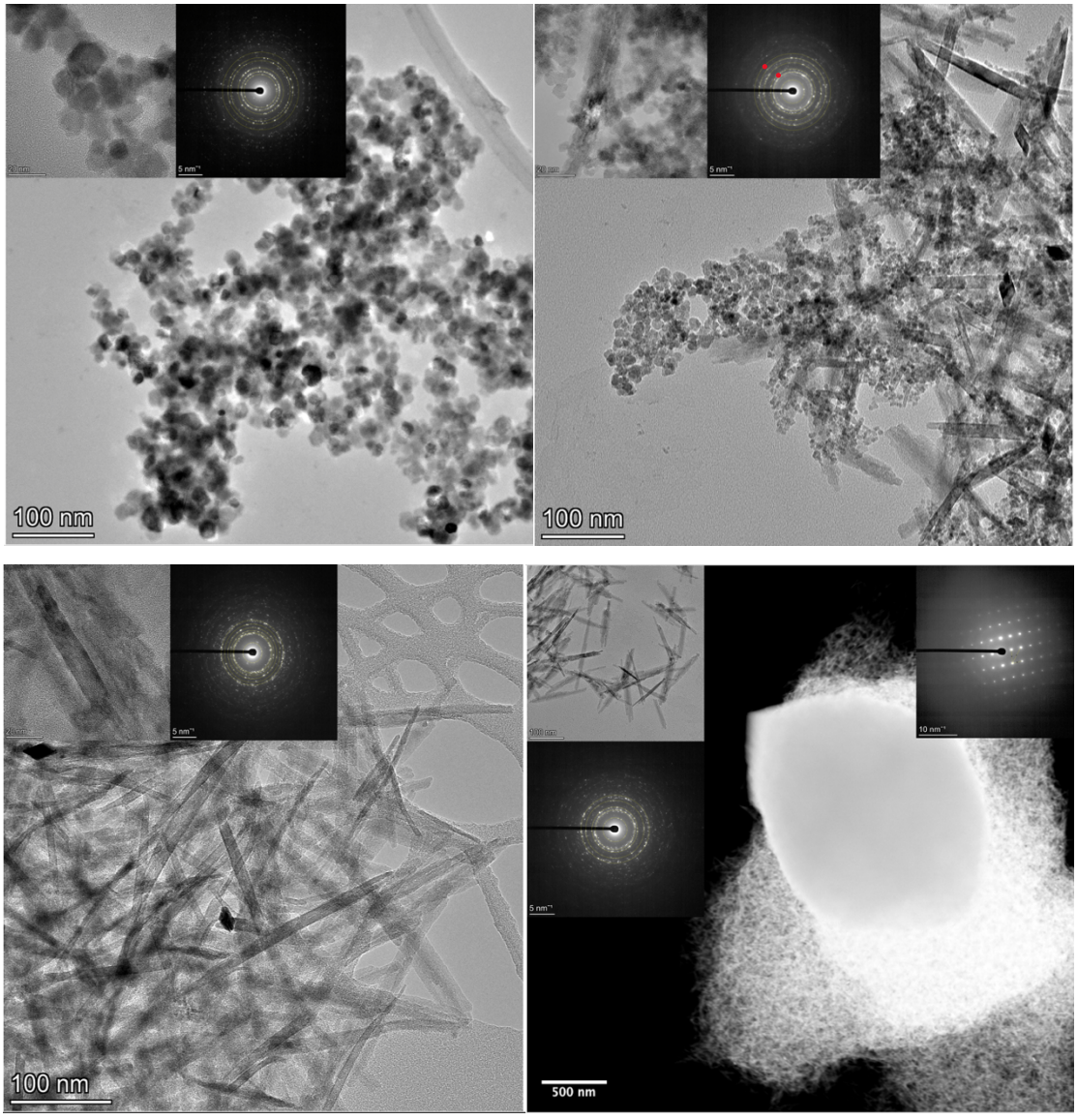

Figure 4.5 TEM images of A)0.5% B) 1% C) 2% D) 5% Ce bearing post reduction products and their TEM diffraction results. Reflections belonging to Goethite have been marked with red dots to separate them from those of magnetite in B)1% samples.

X-ray magnetic circular dichroism (XMCD) spectra at the Fe $L_{2,3}$-edge were collected for the *G. sulfurreducens* bioreduction products to investigate the

structure of the magnetic biominerals that were formed. Figure 4.6 shows the Fe $L_{2,3}$ XMCD experimental spectra (black lines) and the best-fit calculated spectra (red lines) for all samples. Fitting the spectra using calculated data for the three potential Fe environments within magnetite (Fe^{2+} octahedral coordination (O_h), Fe^{3+} tetrahedral coordination (T_d) and Fe^{3+} O_h)can provide information on the oxidation state and site occupancies of the Fe cations.

Stoichiometric magnetite has an Fe occupancy of 1:1:1 in each of the $Fe^{2+}O_h$: $Fe^{3+}T_d$: $Fe^{3+}O_h$ sites (Coker et al., 2007) similar to the Fe occupancies measured in the biogenic magnetite (Table 4.1). However, the 0.5% and 1% Ce bearing samples differed, with increased values for Fe(II) O_h , and decreased occupancies of Fe(III) in both the T_d and O_h sites. In general, the Fe(II) to Fe(III) ratios of the Ce-magnetite samples were much higher than that of the biogenic magnetite, and the ratio in 1% Ce-bearing samples was highest. In addition, the proportion of d^5 Fe(III) O_h in the Ce bearing magnetic samples (0.5% and 1%) were both lower than that in the biomagnetite, and the 1% Ce-bearing sample had the least amount of Fe(III) O_h of all samples which suggested that with the increasing of Ce, the content of Fe(III) O_h decreased. These data could indicated that Ce was partially incorporated into the Fe(III) sites of the magnetite and replaced some Fe(III) in O_h sites; however, further information is required, specifically Ce *L-edge* EXAFS data, to investigate this possibility further.

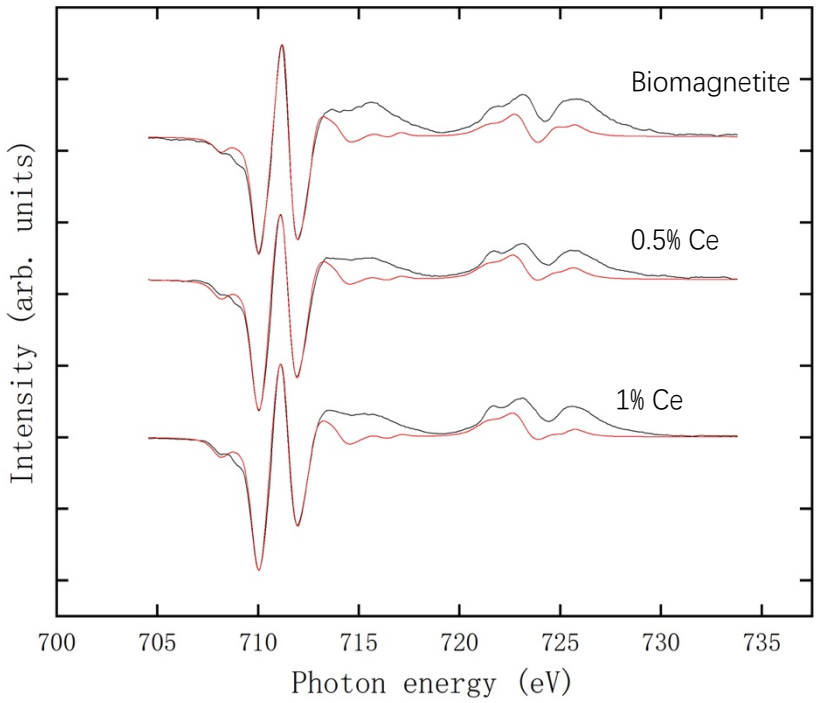

Figure 4.6 The Fe L2,3 XMCD experimental (black line) spectrum and best fit (red line) calculated spectrum of pure biomagnetite, 0.5% Ce bearing samples and 1% Ce bearing samples

Table 4.1 Fe site occupancies and the ratio of Td/Oh and FeII/FeIII for all biomagnetite, calculated from XMCD.

sample name	d^6 FeII O_h	d^5 FeIII T_d	d^5 FeIII O_h	total	Td/Oh	FeII/FeIII
0.5% Ce post	1.22	0.94	0.85	3.01	0.45	0.68
1% Ce post	1.28	0.98	0.75	3.01	0.48	0.74
biomagnetite	1.05	1.05	0.91	3.01	0.54	0.54

4.3.4 Application of biomagnetite and 0.5% Ce-bearing magnetite in carbon black supported platinum catalysts for oxygen reduction reactions

In a hydrogen fuel cell, hydrogen is oxidized at the anode and oxygen is

reduced at the cathode. The oxygen reduction kinetics of the cathode is relatively slow as the breaking of O-O bonds is challenging, and efficient catalysts are needed to improve the energy conversion efficiency of the whole system. According to previous studies, Pt and platinum-based catalysts have the highest catalytic activity for oxygen reduction. However, platinum is very expensive, and sourcing non-noble metal catalysts to reduce the amount of platinum used has become a research focus. As cerium-containing materials and magnetite are both used as catalysts in fuel cell electrodes, the products of the Fe(III)/Ce bioreduction experiments were tested for this application. According to the XRD and TEM results, magnetite was detected in both the 0.5% and 1% Ce bearing sample, but the 1% Ce bearing sample contained high levels of goethite contamination. For this reason, pure biomagnetite and 0.5% Ce-bearing magnetite were added into carbon black supported platinum catalysts, and their performance tested (figure 4.7, figure 4.8 and table 4.2). It should be noted that the 1% Ce magnetite and goethite-bearing sample yielded poor results in preliminary tests (not show here).

Electrochemical characterization was conducted to assess the activity of the catalysts. Electrochemical surface areas (ECSAs) of carbon black supported Pt-Fe alloy catalysts are shown in Figure 4.7 and Table 4.2. Fe-Pt/CB showed a maximum ECSA of 17.6 $m^2 \cdot g^{-1}$, which was higher than that of Pt/CB, at 16.1 $m^2 \cdot g^{-1}$. With the addition of Ce, the ECSA decreased to 7.6$m^2 \cdot g^{-1}$ for

the 0.5% Ce-Fe-Pt/CB. This is the result of uneven dispersion and larger particle formation of Pt, thereby decreasing the effective ECSA.

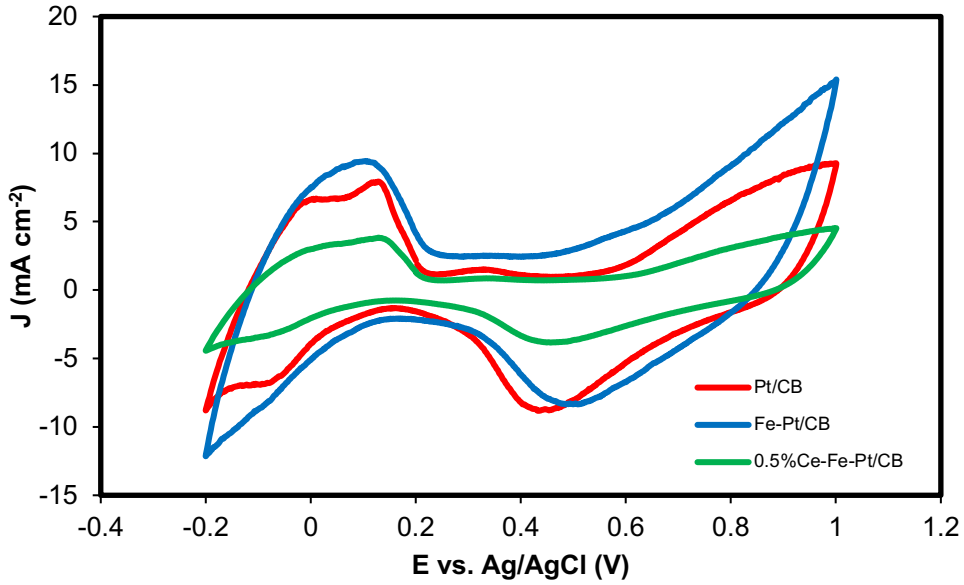

Figure 4.7 CV curves results of 0.5%Ce-Fe-Pt/CB, Fe-Pt/CB and Pt/CB.

Table 4.2 Electrochemical characterization of catalysts before and after AST.

Catalysts	Before AST				After AST			
	ECSA (m^2/g)	E_0 (V)	$E_{1/2}$ (V)	J (mA/cm^2)	ECSA (m^2/g)	E_0 (V)	$E_{1/2}$ (V)	J (mA/cm^2)
Fe-Pt/CB	17.58	0.84	0.64	-6.14	9.73	0.84	0.54	-5.21
0.5%Ce-Fe-Pt/CB	7.60	0.85	0.58	-5.35	5.78	0.79	0.59	-5.06
Pt/CB	16.10	0.88	0.62	-6.01	10.76	0.87	0.59	-5.22

linear sweep voltammetry (LSV) was also used to estimate the activity of the oxygen reduction reaction (ORR) for all catalysts under a rotating speed of 1600 rpm (Figure 4.8). The Fe-Pt/CB sample gave the lowest diffusion-limiting current density of -6.14 $mA \cdot cm^{-2}$, similar to that of Pt/CB (-6.01 $mA \cdot cm^{-2}$),

and lower than that of 0.5% Ce-Fe-Pt/CB (-5.35 $mA \cdot cm^{-2}$) (see Table 4.2). Moreover, the half-wave potential ($E_{1/2}$) of 0.639 V for Fe-Pt/CB was higher than that of 0.624 V for Pt/CB and 0.585 V for 0.5% Ce-Fe-Pt/CB. This suggested that Fe-Pt/CB had a similar ORR activity to that of the Pt/CB sample, obtained while using lower amounts of Pt. Meanwhile, the onset potential (E_0) of Fe-Pt/CB and 0.5% Ce-Fe-Pt/CB was approximately 0.84 V, while Pt/CB had a higher onset potential of 0.88 V. This indicated that the addition of magnetite and Ce-magnetite slightly retarded the start of the oxygen reduction reaction.

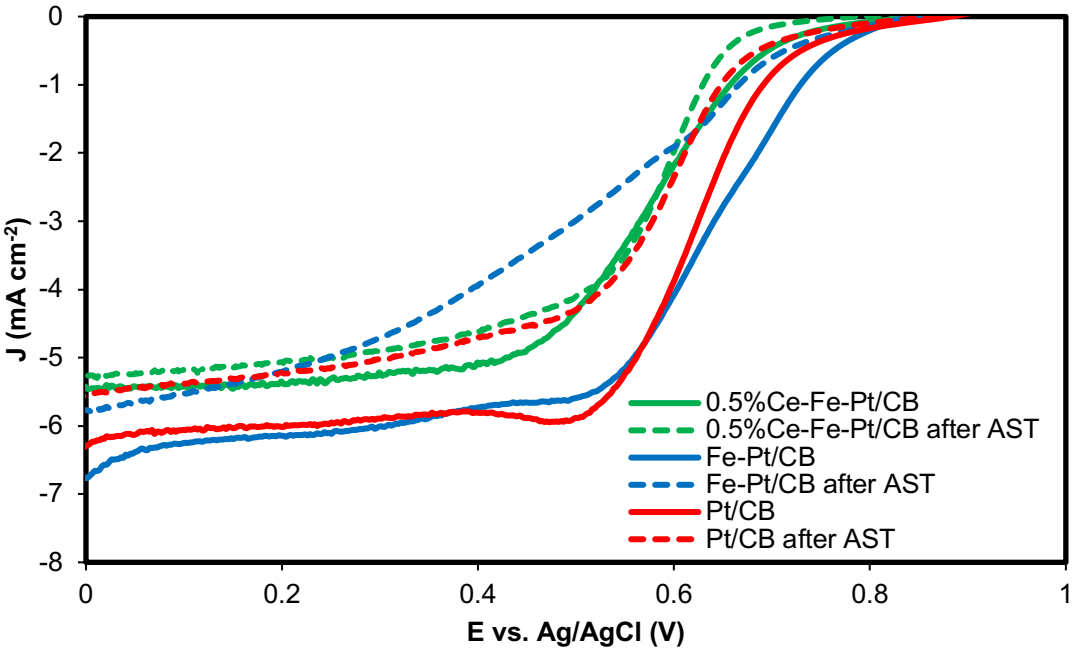

Figure 4.8 LSV before (solid lines) and after (dotted lines) 30000 cycles of AST.

The durability of the Fe-Pt/CB, 0.5%Ce-Fe-Pt/CB and Pt/CB containing electrodes were first estimated after the accelerated stress test (AST) followed by the ECSA (see Figure S1.3 and Table 4.2). The ECSA of Fe-Pt/CB declined dramatically with 45% loss after 30000 cycles of AST. In addition, there was a 33% loss of initial ECSA with the Pt/CB materials. The ECSAs decreased by

only 23% for 0.5% Ce-Fe-Pt/CB, indicating a better durability compared to Pt/CB and Fe-Pt/CB.

A comparison of ORR activities before (solid lines) and after (dotted lines) 30000 cycles AST was carried out to estimate the durability of these catalysts (Figure 4.8). The 0.5% Ce-Fe-Pt/CB material was relatively stable with a negligible decrease of half-wave potential between 0.585 V and 0.580 V. However, significant decreases from 0.639 V to 0.536 V and from 0.624 V to 0.592 V, were evident for Fe-Pt/CB and Pt/CB materials, respectively. These results illustrated that the Fe-Pt alloy had a lower durability than pure Pt catalysts; however, the added Ce materials substantially improved the stability of the Fe-Pt alloy catalysts. The diffusion-limiting current density of the 0.5% Ce-Fe-Pt/CB electrode was reduced by only 5.3% (-5.35 to -5.06 $mA \cdot cm^{-2}$), compared to 13.1% and 15.1% losses with the Pt/CB and Fe-Pt/CB materials respectively (decreased to 5.22 $mA \cdot cm^{-2}$ and 5.21 $mA \cdot cm^{-2}$).

In summary, an electrode containing 0.5% Ce-Fe-Pt/CB possessed similar ORR activity to Pt/CB and Fe-Pt/CB electrodes after AST, however, it retained about 94% of the diffusion-limiting current density after 30000 cycles. Thus the addition of Ce-bearing biomagnetite to a Pt/CB electrode can lead to improved electrode durability for catalytic ORR applications, which in turn will reduce operating costs and lead to decreased utilisation of Pt (around 17% reduced).

According to the research of Masuda et al (2012), the metallic Pt is more suitable catalyst for ORR activity (compared to Pt oxides), so the longer durability of 0.5% Ce-Fe-Pt/CB was most likely due to the presence of Ce^{3+} which could be oxidized to Ce^{4}+, limiting the formation of Pt oxides (Masuda et al., 2012).

4.4 Conclusion

In conclusion, when Ce was co-precipitated with ferrihydrite, it was successfully reduced by *G. sulfurreducens* to yield Ce bearing magnetite, although at higher concentrations (2% molar ratio; 1.43% real Ce content) microbial Fe(III) reduction was inhibited and goethite was produced. During the bioreduction processes (7 days), the lack of Ce solubilisation in all our experiments suggest a tight coupling between Fe and Ce in natural and engineered systems, which also opens up the way for the production of novel functional biomaterials for technological use. This is illustrated by the superior performance of Pt/CB fuel cell catalysts when supplemented with 0.5% Ce-biomagnetite, offering improved and more durable catalytic activity with around 17% reduced of the platinum content of commercial Pt/CB. These proof of concept experiments point the way to novel bioprocessing options for REE materials, that could be further engineered for applications using a range of approaches including optimization of biological activity.

Acknowledgements

We would like to thank Mr Paul R, Lythgoe and Dr. Abby Ragazzon-Smith for their suggestions and assistances with ICP-AES analyses. We also thank Dr, John Water for assistance with XRD measurements and data analysis. I also would like to thank Sul who guided me a lot in the beginning of the experiment. The Advanced Light Source is supported by the Director, Office of Science, Office of Basic Energy Sciences, of the US Department of Energy. The authors acknowledge beamtime awarded at the Diamond Light Source for XANES on beamline B18 under proposal SP-16136.

References:

Andres, Y., Texier, A.-C. & Le Cloirec, P. (2003). 'Rare earth elements removal by microbial biosorption: A review' *Environmental technology*, 24 (11), pp. 1367-1375.

Aneggi, E., et al. (2020). 'Catalytic applications of cerium dioxide', Cerium oxide (ceo_2): Synthesis, properties and applications: *Elsevier*, pp. 45-108.

Beltrán-Gastélum, M., et al. (2019). 'Pt-au nanoparticles on graphene for oxygen reduction reaction: Stability and performance on proton exchange membrane fuel cell' *Energy*, 181 pp. 1225-1234.

Byrne, J., et al. (2013). 'Controlled cobalt doping in biogenic magnetite nanoparticles' *Journal of The Royal Society Interface*, 10 (83), p. 20130134.

Byrne, J. M., et al. (2015). 'Scale-up of the production of highly reactive biogenic magnetite nanoparticles using *geobacter sulfurreducens*' *Journal of the royal society interface*, 12 (107), p. 20150240.

Coker, V., et al. (2006). 'Xas and xmcd evidence for species-dependent partitioning of arsenic during microbial reduction of ferrihydrite to magnetite' *Environmental science & technology*, 40 (24), pp. 7745-7750.

Coker, V. S., et al. (2007). 'Cation site occupancy of biogenic magnetite compared to polygenic ferrite spinels determined by x-ray magnetic circular dichroism' *European Journal of Mineralogy*, 19 (5), pp. 707-716.

Coppi, M. V., Leang, C., Sandler, S. J. & Lovley, D. R. (2001). 'Development of a genetic system for *geobacter sulfurreducens*' *Applied and environmental microbiology*, 67 (7), pp. 3180-3187.

Cutting, R. S., et al. (2010). 'Optimizing cr (vi) and tc (vii) remediation through nanoscale biomineral engineering' *Environmental science & technology*, 44 (7), pp. 2577-2584.

Cutting, R. S., et al. (2012). 'Microbial reduction of arsenic-doped schwertmannite by *geobacter sulfurreducens*' *Environmental science & technology*, 46 (22), pp. 12591-12599.

Dahle, J. T. & Arai, Y. (2015). 'Environmental geochemistry of cerium: Applications and toxicology of cerium oxide nanoparticles' *International journal of environmental research and public health*, 12 (2), pp. 1253-1278.

Dong, L., et al. (2010). 'Graphene-supported platinum and platinum–ruthenium nanoparticles with high electrocatalytic activity for methanol and ethanol oxidation' *Carbon*, 48 (3), pp. 781-787.

Frey, M. H., Pierpont, D. M. & Hamrock, S. J. (2013). High durability fuel cell components with cerium oxide additives. Google Patents.

García, A., et al. (2012). 'Effect of cerium dioxide, titanium dioxide, silver, and gold nanoparticles on the activity of microbial communities intended in wastewater treatment' *Journal of hazardous materials*, 199 pp. 64-72.

Janots, E., et al. (2015). ‘Ce (iii) and ce (iv)(re) distribution and fractionation in a laterite profile from madagascar: Insights from in situ xanes spectroscopy at the ce liii-edge’ *Geochimica et cosmochimica acta*, 153 pp. 134-148.

Ji, Z., et al. (2021). ‘A structured catalyst support combining electrochemically exfoliated graphene oxide and carbon black for enhanced performance and durability in low-temperature hydrogen fuel cells’ *Energy*, 226 p. 120318.

Joshi, N., et al. (2018). ‘Microbial reduction of natural fe (iii) minerals; toward the sustainable production of functional magnetic nanoparticles’ *Frontiers in Environmental Science*, 6 p. 127.

Kim, J., et al. (2004). ‘Role of microbes in the smectite-to-illite reaction’ *Science*, 303 (5659), pp. 830-832.

Kimber, R. L., et al. (2018). ‘Biosynthesis and characterization of copper nanoparticles using *shewanella oneidensis*: Application for click chemistry’ *Small*, 14 (10), p. 1703145.

Lim, C., et al. (2015). ‘Fuel cell durability enhancement with cerium oxide under combined chemical and mechanical membrane degradation’ *ECS Electrochemistry Letters*, 4 (4), p. F29.

Liu, H. (2016). ‘Rare earths: Shades of grey: Can china continue to fuel our global clean & smart future’ *China Water Risk*.

Liu, P., et al. (2018). ‘Stimulated electron transfer inside electroactive biofilm by magnetite for increased performance microbial fuel cell’ *Applied energy*, 216 pp. 382-388.

Lloyd, J. R. (2003). ‘Microbial reduction of metals and radionuclides’ *FEMS microbiology reviews*, 27 (2-3), pp. 411-425.

Lovley, D. R., et al. (1993). ‘*Geobacter metallireducens* gen. Nov. Sp. Nov., a microorganism capable of coupling the complete oxidation of organic compounds to the reduction of iron and other metals’ *Archives of microbiology*, 159 (4), pp. 336-344.

Lovley, D. R. & Phillips, E. J. (1987). ‘Competitive mechanisms for inhibition of sulfate reduction and methane production in the zone of ferric iron reduction in sediments’ *Applied and Environmental Microbiology*, 53 (11), pp. 2636-2641.

Lovley, D. R., Stolz, J. F., Nord, G. L. & Phillips, E. J. (1987). ‘Anaerobic production of magnetite by a dissimilatory iron-reducing microorganism’ *Nature*, 330 (6145), pp. 252-254.

Masuda, T., et al. (2012). ‘Role of cerium oxide in the enhancement of activity for the oxygen reduction reaction at pt–ceox nanocomposite electrocatalyst - an in situ electrochemical x-ray absorption fine structure study’ *The Journal of Physical Chemistry C*, 116 (18), pp. 10098-10102. DOI: 10.1021/jp301509t.

Nancharaiah, Y., Mohan, S. V. & Lens, P. (2016). ‘Biological and bioelectrochemical recovery of critical and scarce metals’ *Trends in*

biotechnology, 34 (2), pp. 137-155.
Natarajan, G. & Ting, Y.-P. (2015). 'Gold biorecovery from e-waste: An improved strategy through spent medium leaching with ph modification' *Chemosphere*, 136 pp. 232-238.
Newsome, L., et al. (2014). 'Microbial reduction of uranium (vi) in sediments of different lithologies collected from sellafield' *Applied geochemistry*, 51 pp. 55-64.
Ohnuki, T., et al. (2015). 'Sorption of trivalent cerium by a mixture of microbial cells and manganese oxides: Effect of microbial cells on the oxidation of trivalent cerium' *Geochimica et Cosmochimica Acta*, 163 pp. 1-13.
Ohnuki, T., et al. (2008). 'Concurrent transformation of ce (iii) and formation of biogenic manganese oxides' *Chemical Geology*, 253 (1-2), pp. 23-29.
Ouyang, T., et al. (2006). 'Dissolved trace elements in river water: Spatial distribution and the influencing factor, a study for the pearl river delta economic zone, china' *Environmental geology*, 49 (5), pp. 733-742.
Patterson, A. (1939). 'The scherrer formula for x-ray particle size determination' *Physical review*, 56 (10), p. 978.
Pattrick, R. A., et al. (2002). 'Cation site occupancy in spinel ferrites studied by x-ray magnetic circular dichroism: Developing a method for mineralogists' *European Journal of Mineralogy*, 14 (6), pp. 1095-1102.
Seger, B. & Kamat, P. V. (2009). 'Electrocatalytically active graphene-platinum nanocomposites. Role of 2-d carbon support in pem fuel cells' *The Journal of Physical Chemistry C*, 113 (19), pp. 7990-7995.
Sridharan, V. & Menéndez, J. C. (2010). 'Cerium (iv) ammonium nitrate as a catalyst in organic synthesis' *Chemical reviews*, 110 (6), pp. 3805-3849.
Takahashi, M., et al. (2007). 'Design of high-quality pt–ceo2 composite anodes supported by carbon black for direct methanol fuel cell application' *Journal of the American Ceramic Society*, 90 (4), pp. 1291-1294.
Zhu, N., et al. (2016). 'Biorecovery of gold as nanoparticles and its catalytic activities for p-nitrophenol degradation' *Environmental Science and Pollution Research*, 23 (8), pp. 7627-7638.
Zhu, S., Marschilok, A. C., Takeuchi, E. S. & Takeuchi, K. J. (2009). 'Crystallite size control and resulting electrochemistry of magnetite, fe3o4' *Electrochemical and Solid-State Letters*, 12 (4), p. A91.
Zou, D., et al. (2014). 'Wet air oxidation and kinetics of cerium (iii) of rare earth hydroxides' *Industrial & Engineering Chemistry Research*, 53 (35), pp. 13790-13796.

Appendix S4

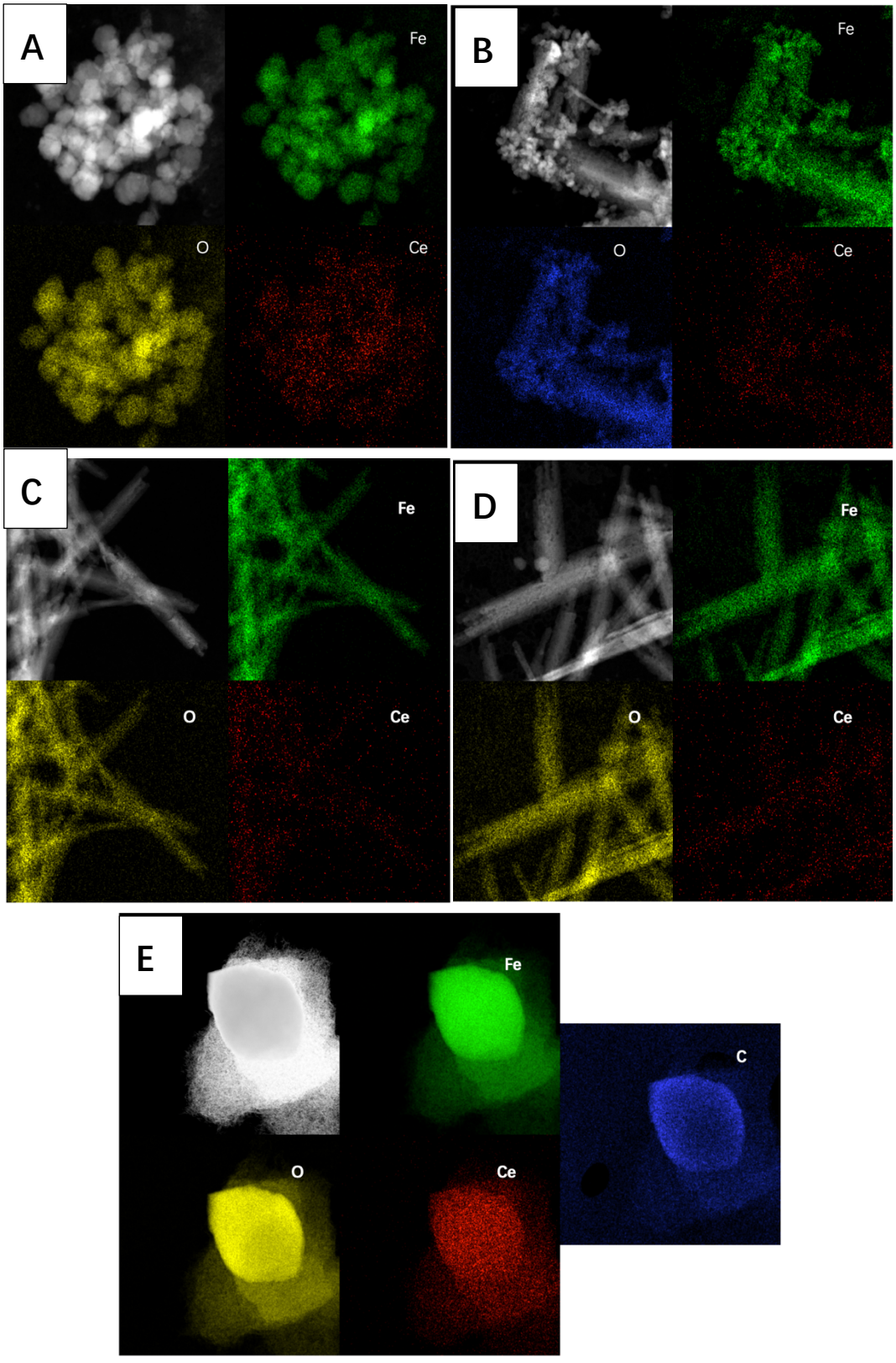

Figure S 4.1 TEM HAADF and EDS mapping images of A) 0.5%, B) 1%, C) 2%, D) and E) 5% Ce bearing post reduction products.

A: The bioreduction product of 0.5% samples was magnetite, the location of Fe has been marked as green and the location of Ce has been marked as red. B: The bioreduction products of 1% samples were magnetite and goethite, the location of Fe has been marked as green and the location of Ce has been marked as red. C: TEM results show the bioreduction product was goethite. The location of Fe has been marked as green and the location of Ce has been marked as re. For 5% Ce samples there were two different minerals in the products D: Goethite, the location of Fe has been marked as green and the location of Sb has been marked as red. E: carbonate mineral containing Fe and Ce. The location of Fe has been marked as green. The location of Ce has been marked as red and the location of C has been marked as blue.

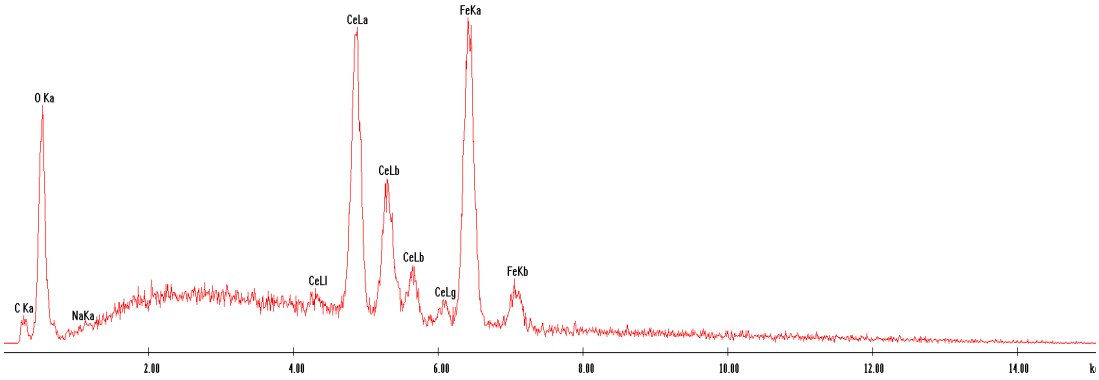

Figure S 4.2 ESEM image of 5% Ce bearing samples bioreduction product and EDS results of selected long strip minerals

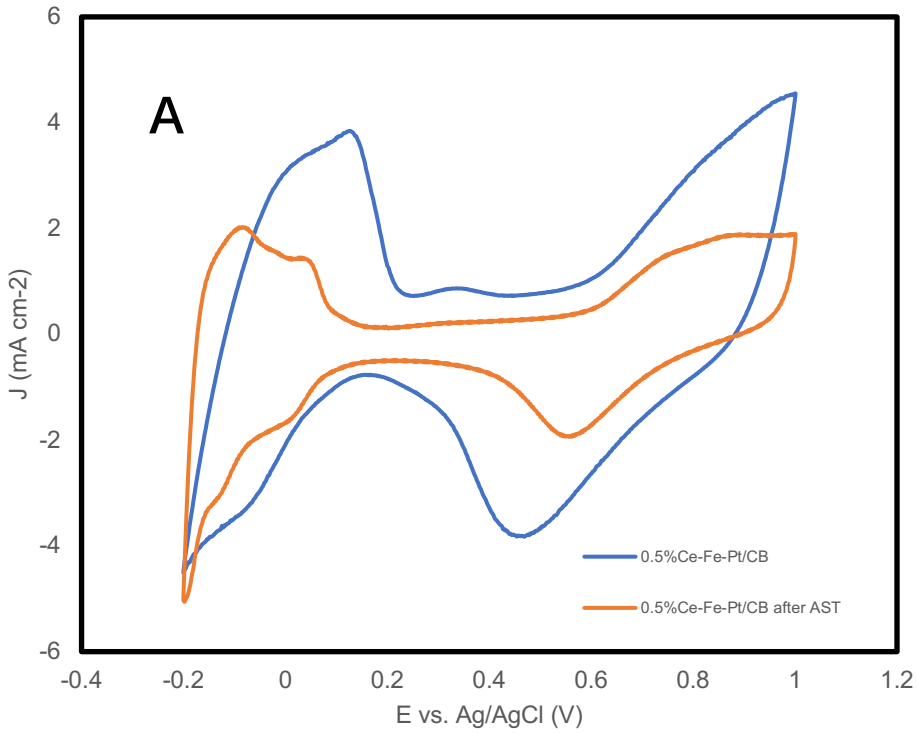

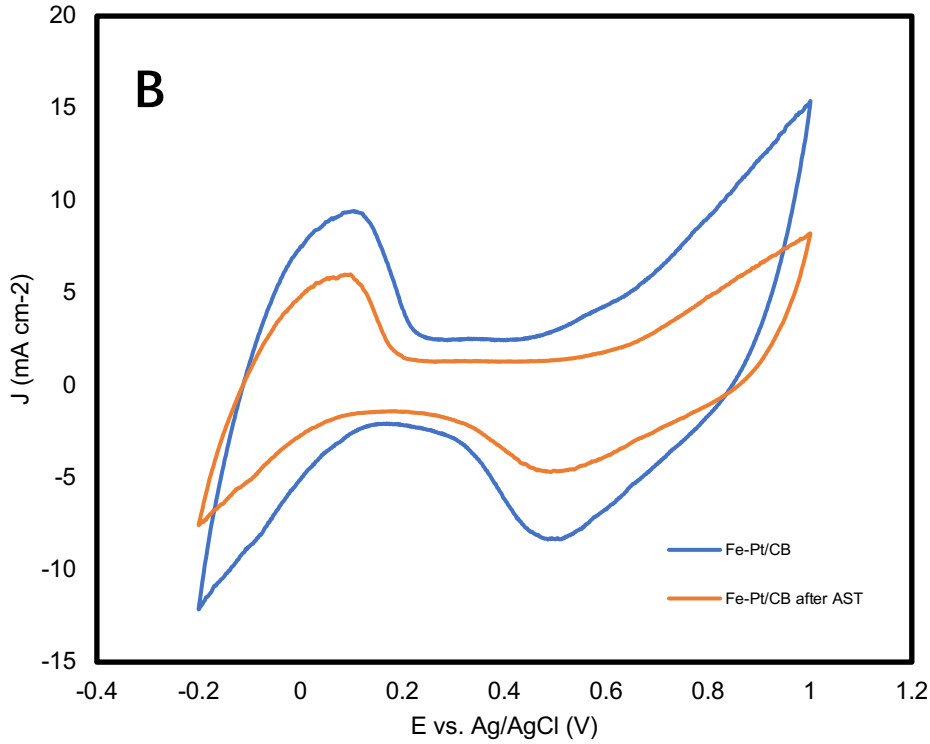

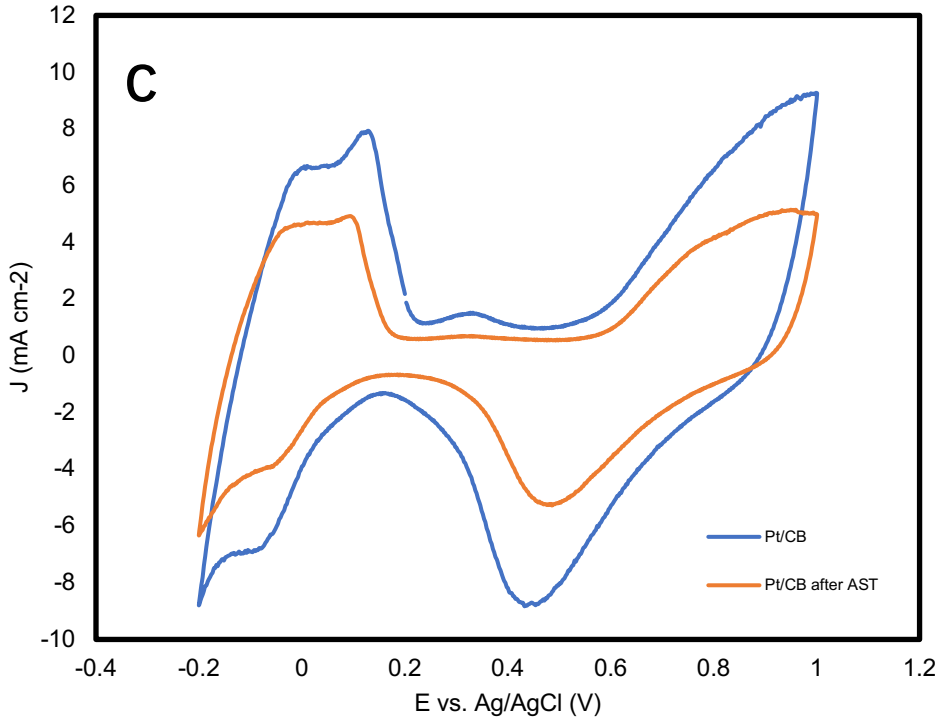

Figure S 4.3 ECSA results of different materials before and after AST. A) 0.5%Ce-Fe-Pt/CB, B) Fe-Pt/CB, C) Pt/CB

Chapter 5 :
Microbial reduction of antimony(V)-bearing ferrihydrite by *Geobacter sulfurreducens*

Jinxin Xie, Victoria S. Coker, Brian O'Driscoll, Rongsheng Cai, Sarah J. Haigh,Jonathan R. Lloyd*

This chapter is a manuscript in preparation for the journal Applied and Environmental Microbiology. Supporting information submitted with this manuscript is included in Appendix S5.

Chapter 5: Microbial reduction of antimony(V)-bearing ferrihydrite by *Geobacter sulfurreducens*

Jinxin Xie, Victoria S. Coker, Brian O'Driscoll, Rongsheng Cai, Sarah J. Haigh,Jonathan R. Lloyd*

Abstract:

The reduction of Sb(V)-bearing ferrihydrite by *Geobacter sulfurreducens* was studied to determine the fate of the metalloid in Fe-rich systems undergoing redox transformations. Sb(V) added at a range of concentrations adsorbed readily to ferrihydrite, and the loadings had pronounced impact on the rate and extent of Fe(III) reduction and the products formed. Magnetite dominated at low (0.5 and 1 mol%) Sb(V) concentrations, with crystallite sizes decreasing at higher Sb loadings; 37 nm, 25 nm and 17 nm for no Sb, 0.5% and 1% samples respectively. In contrast, goethite was the dominant end product for samples with higher antimony loadings (2 and 5 mol%), with increased goethite grainsize in the 5% sample (20 nm width versus 250 nm length). XPS analyses showed that there was no Sb(III) formation during the bioreduction process, confirming that the Fe(III)-reducing bacterium *G. sulfurreducens* cannot reduce Sb(V) enzymatically of via biogenic Fe(II). These findings suggest that a range of Fe (bio)minerals have a potential role in controlling antimony pollution in the environment, even when undergoing redox transformations.

5.1 Introduction

Antimony (Sb) is a metalloid pnictogen belonging to Group 15 of the periodic table and shares many physical and chemical characteristics with arsenic (As), also a Group 15 element (Filella et al., 2002b; Filella et al., 2007; Terry et al., 2015). Antimony has widespread applications in the production of flame retardants, textiles, papers, adhesives, tires, brake linings and plastics (Wang et al., 2013). The main source of antimony is mining and world reserves are ~1,800,000 tons (as of 2016), with the majority found in China, Bolivia, Mexico, Russia, South Africa and Tajikistan. However, nearly 80% of global Sb supply is currently met by China (Li et al., 2016). Antimony is a chalcophile, and as such is often found in nature in sulphide minerals such as stibnite (Sb_2S_3) (Filella et al., 2002a).

Antimony is common in water and soils at low concentration (<1 µg/L); however, higher concentrations of free Sb ions can be discharged through mining, industrial processing or natural weathering of Sb-containing minerals, which can be harmful to the environment and human health[2]. Long-term exposure to high antimony levels can cause health problems, such as lesions of the lungs and heart; therefore, Sb and its compounds are considered pollutants by the US Environmental Protection Agency and the Council of European Communities (EU, 1998; Li et al., 2016; Terry et al., 2015; USEPA, 1999). Antimony is similar to arsenic in that it is not essential for life and its

bioavailability and toxicity depends on its chemical form and oxidation state, with toxicity of Sb decreasing as follows: Sb(III) > Sb(V) > organoantimonials (Gebel, 1997; Wilson et al., 2010).

Antimony mining in southwest China has led to environmental contamination issues where antimony concentrations in water, sediment, and soil were 29.4 mg/L, 1163 mg/kg and 2 mg/kg, respectively, which significantly exceed the maximum allowable limits (1μg/L, 0.800 - 3.00 mg/ kg and 0.57 mg/ kg) (Li et al., 2016). In Australia, Bakers Creek is a highly contaminated river near to an Sb-As mining area, Hillgrove Mine. High concentrations of antimony were detected in both sediment and water of 777 (± 115) μg/g and 381 (± 23) μg/L, respectively (Telford et al., 2009) in Hillgrove Mine. As such, Sb has become a global environmental issue especially in Australia, as well as China and parts of Europe (Kulp et al., 2014).

Sb(III) and Sb(V) can be adsorbed by Fe(III) oxide minerals, such as ferrihydrite and goethite (Filella et al., 2002a; Mitsunobu et al., 2010; Wilson et al., 2010), and may be impacted by subsequent redox transformations. Insights gained from research on the biogeochemistry of As, including the mobility of As mediated by microbial transformations in groundwater systems (Cutting et al., 2012; Islam et al., 2004; Islam et al., 2005), have contributed to our understanding of how antimony in the environment may be impacted by

microbial processes. For example, it is possible that microbially-mediated Fe(III) reduction, may increase the mobility Sb as it does with As (Islam et al., 2004). However, according to previous work, *Geobacter sulfurreducens* cannot reduce As(V) directly in solution, but it can reduce soluble Fe(III) and As bearing ferrihydrite to form new Fe minerals, retaining any sorbed As in the Fe minerals produced (Islam et al., 2005). Thus, as the biogeochemistry of Sb is similar to that of As, it is possible that secondary Fe(II)-bearing minerals could also influence the mobility of Sb(V). Furthermore, previous work suggests that Fe(II)-bearing minerals such as green rust, magnetite and mackinawite can reduce soluble Sb(V) to Sb(III) through chemical redox reactions (Kirsch et al., 2008; Mitsunobu et al., 2008). Therefore, further insights into the biological immobilization of Sb(V) may be gained by studying the bioreduction process(es) of Fe(III) minerals in the presence of the metalloid. Several studies have documented the influence of Fe(III) and Fe(II) minerals on the migration of Sb(III) and Sb(V) under both natural and laboratory conditions (Burton et al., 2019; Filella et al., 2002a; Hockmann et al., 2021; Karimian et al., 2017; Wilson et al., 2010). However, the immobilisation of Sb(V) by ferrihydrite and biologically-formed secondary Fe(III)- and Fe(II)-bearing minerals is a comparatively poorly studied topic.

Dissimilatory metal reducing bacteria (DMRB) such as *Geobacter sulfurreducens* and *Shewanella oneidensis,* can transfer electrons to poorly

crystalline Fe(III) minerals, such as ferrihydrite, using organic matter as an electron donor, to produce Fe(II)-bearing minerals, such as magnetite (Fe_3O_4), siderite ($FeCO_3$) or vivianite ($Fe_3^{2+}(PO_4)_2 8H_2O$) (Lloyd, 2003; Lovley et al., 1993; Lovley and Phillips, 1987). During this reductive biotransformation, Fe(III) in the ferrihydrite is reduced generating Fe(II) ions, which then form the more reduced phase (magnetite) through dissolution and reprecipitation reactions (Byrne et al., 2015; Coker et al., 2006; Cutting et al., 2012; Lovley and Phillips, 1987). However, when additional ions, such as Sb, are adsorbed to ferrihydrite, this could change the reaction products formed during the bioreduction process. For example in a recent study by Burton et al. (2019), *S. oneidensis* was used to reduce 10% Sb-bearing ferrihydrite (Sb:Fe ratio). Here Fe(II) concentrations increased slightly during bioreduction, but the products detected were exclusively Fe(III)-minerals, feroxyhyte ($Fe^{3+}O(OH)$) and goethite (α-FeO(OH)), rather than magnetite (Burton et al., 2019). There are comparatively few studies on the interplay between Fe(III) and antimony species during microbial reduction processes (Charnock et al., 2004). In addition, the effect of lower antimony concentrations on the processes of biological Fe(III) reduction is not well understood.

In light of the above, the aim of this study was to examine the impact of antimony on the bioreduction of Fe(III)-oxyhydroxide (ferrihydrite) by *G. sulfurreducens*, at a range of Sb concentrations, exploring the fate and

oxidation state of the metalloid and its interactions with any Fe(II)-bearing minerals formed. Our results have the potential to improve understanding of antimony cycling in the natural environment, and also have the potential to be applied to the treatment of antimony contamination in natural systems, with applications in the biorecovery and reuse of antimony.

5.2 Materials and Methods

5.2.1 Synthesis of ferrihydrite and Sb(V) stock solution preparation

Ferrihydrite was prepared according to methods of Lovley and Phillips (Byrne et al., 2011; Lovley and Phillips, 1986). Approximately 108 g of $FeCl_3.6H_2O$ (Sigma-Aldrich) was dissolved into 1 L deionized water. The homogeneous Fe(III) solution was then hydrolysed and precipitated by 10N NaOH solution to achieve a final pH of ~7 and the mixture was continually mixed by a magnetic stirrer for 1 hour, while maintaining a constant pH value. The mixture was divided into centrifuge tubes and centrifuged at 5000 *g*, at room temperature, for 20 minutes. The supernatant was removed and the solid resuspended in deionized water. Repeat washing steps were carried out an additional 5 times. The washed ferrihydrite was then stored in a fridge (4 ℃). The exact concentration of ferrihydrite was measured using both ICP-MS and Ferrozine assay.

Potassium hexahydroxoantimonate (V) ($KSb(OH)_6$) (1.3145 g) was added to

250 ml DIW to achieve a 20 mM Sb(V) stock solution. The Sb(V) stock solution was stored at 4 ºC in the dark before use in the experiments.

5.2.2 Cultivation of *Geobacter sulfurreducens*

The Fe(III)-reducing bacterium *G. sulfurreducens* was grown on a medium containing sodium acetate (20 mM) as the electron donor and fumaric acid (40 mM) as the electron acceptor, prepared as described by Coppi et al. (2001) (Coppi et al., 2001). Late exponential cultures of *G. sulfurreducens,* grown at 30 ºC, were harvested and washed twice in 30 mM sodium bicarbonate solution before use. All media and solutions were flushed with 80:20 (v/v) N_2 and CO_2 to remove O_2 and maintained at circumneutral pH.

5.2.3 Sb adsorption experiments and microbial reduction of Sb adsorbed ferrihydrite

Ferrihydrite, sodium bicarbonate and sodium acetate (electron donor) were added to each bottle to achieve the final concentration of 10 mmoles $liter^{-1}$ slurry of Fe, 30 mM and 10 mM, respectively (set final volume 100 ml). 0.25 ml, 0.5 ml,1 ml and 2.5 ml of 20 mM Sb(V) solution were subsequently added to bottles to achieve an Sb(V):Fe(III) of 0.5%,1%, 2% and 5% (mol%) , respectively. After flushing with 80:20 (v/v) N_2 and CO_2, these bottles were maintained at room temperature and samples collected regularly to determine the concentration of residual Sb in the liquid phase during a 186 hour adsorption process. After this adsorption period, a washed cell suspension of *G. sulfurreducens* was added

to the Sb(V)/ferrihydrite slurries to the equivalent final OD_{600} of ~0.4 biomass. All bottles were then incubated at 30 ºC. Samples were taken periodically for ferrozine assay to quantify the changes in bioavailable Fe(II) and total Fe concentration, and the concentration of Sb remaining in solution was analysed by ICP-MS.

5.2.4 Geochemical and mineralogical analysis

The ferrozine assay is used to measure bioavailable Fe(II) and total Fe concentrations (Lovley and Phillips, 1987). 0.1 ml of well mixed slurry was added to 4.9 ml of 0.5M HCl for 1 hour. 200 µL of the digested solution was then added to cuvettes that contained 2.3 ml of ferrozine solution to quantify the concentration of Fe(II). Total bioavailable Fe values were obtained by adding a strong reductant, hydroxylamine hydrochloride solution (6.25M), to the sample and digesting for 1 hour prior to the addition of ferrozine.

An Agilent 8800 Triple Quadrupole ICP-MS was used to quantify the concentration of aqueous Fe and Sb in solution. Prior to ICP-MS analysis, 1 ml mineral slurry was taken from each microcosm bottle. After centrifugation at 14,800 *g* for 10 minutes, 0.1 ml of supernatant was removed and added to 9.9 ml 2% HNO_3 for analysis.

High-performance liquid chromatography–Inductively coupled plasma mass spectrometry (HPLC-ICP-MS) was used to detect Sb(V) species in the solution. 10 mg/L $KSb(OH)_6$ (Sb(V)) and Sb (III) oxide (Sb(III)) solution were used as standards. The HPLC-ICP-MS system was operated according to the conditions reported in Polya et al's research (Polya et al., 2003). A 1 ml sample was taken and centrifuged at 14,800 *g* for 10 minutes and then 0.1 ml supernatant was mixed with 4.9 deionised water (DIW) before carrying out the HPLC-ICP-MS analyses.

X-ray diffraction (XRD) measurements of solid samples were carried out on a Bruker D2 Phaser diffractometer, equipped with a Lynxeye XE-T detector, an axial 2.5° Soller slit and anti-scatter screen. The X-ray generator was set to 30 kV and 10 mA, powering an X-ray tube with a copper source, providing CuKα1 X-rays with a wavelength of 1.5406 Å. Approximately 10 ml of slurry was sampled, concentrated by centrifugation and washed anaerobically three times in DIW to remove the soluble salts, then dried in an anaerobic cabinet. The sample was then ground to a fine powder by a pestle and mortar and mixed with 1 ml amyl acetate. The resultant slurries were transferred to glass microscope slides and air-dried. Samples were scanned from 5-70° 2θ, with a step size of 0.04° and a count rate of 0.4 s per step. The resultant patterns were evaluated using EVA version 5, which compares experimental data to standards from the ICDD (International Centre for Diffraction Data) Database.

X-ray Photoelectron Spectroscopy (XPS) was performed using monochromated Al Kα X-ray radiation (1486 eV, 20 mA emission at 300 W, spot size ~ 1 mm diameter) and an EW-4000 electron energy analyser (Scienta Omicron GmbH); the instrument has a base vacuum pressure of $\sim 5 \times 10^{-10}$ mbar. The entrance slit width used was 1.5 mm, and the pass energies used for survey and core level spectra were 200 and 50 eV, respectively, with total energy resolutions of 1 eV and <0.5 eV, respectively (measured using the full width half maximum (FWHM) of Au 4f7/2 from a reference sample). Charge neutralisation was achieved using a low energy electron flood source (FS40A, PreVac, 0.5 eV energy, 600 V extraction voltage, 300 μA current), and the samples were isolated from the ground to avoid differential charging effects. Binding energy scale calibration was performed by using C-C in the C 1s photoelectron peak at 284.8 eV; analysis and curve fitting was performed using Voigt-approximation peaks using CasaXPS.

Imaging of the morphology and structure of the minerals was conducted using a Scanning Transmission Electron Microscope (STEM, Thermo Fisher, Titan, G2 80–200) equipped with an Energy Dispersive X–ray Spectroscopy (EDS) detector and a high angle annular dark field (HAADF) detector operating with an inner angle of 55 mrad at 200 kV. The composition distribution of products was characterized by EDS mapping in STEM mode. Selected area electron diffraction (SAED) patterns were collected using a Thermo Fisher Talos STEM.

The STEM samples were prepared by dispersing washed (three times) mineral samples in DIW and mixing well by oscillators. After the mixture was diluted 5 to 10 times and dropcast onto a copper grid coated with an amorphous carbon film.

5.3 Results and discussion

5.3.1 Sb (V) bioreduction and adsorption experiment results

To test whether *G. sulfurreducens* can enzymatically reduce Sb(V), a washed cell suspension (final OD_{600}=0.4) was added directly into bicarbonate buffered solution containing 0.5 mM Sb(V) and 10 mM sodium acetate as the electron donor. Table S5.1 shows the results of the Sb(V) (HPLC-ICP-MS) and total antimony concentration measurements (ICP-MS) over a 5 day bioreduction period. The data show that after the addition of *G. sulfurreducens*, total antimony and Sb(V) concentrations remain approximately equal, indicating that *G. sulfurreducens* does not directly reduce aqueous Sb(V) to Sb(III).

Sb(V) was then added to suspensions of ferrihydrite to determine the fate of the metalloid when sorbed to insoluble Fe(III) oxyhydroxides. A range of different loadings were prepared ranging from Sb(V):Fe(III) molar ratios of 0.5%,1%, 2% and 5%. During preparation the initial concentration of soluble Sb(V) decreased relatively quickly in all samples (55%-74% Sb adsorbed) over the first 18 hours, with a slower rate of adsorption thereafter (Figure S5.1). At

186 hours, which was the starting point for the bioreduction experiments, the amount of Sb(V) adsorbed onto the ferrihydrite was 97.3%, 96.2%, 95.3% and 90.8%, for the 0.5%,1%,2% and 5% samples, respectively.

Based on the ferrozine assay, the concentration of Fe(II) remained unchanged (around 0.18-0.28 mM, respectively) during the adsorption process. However the amount of total bioavailable iron became progressively lower with increased Sb(V) loading, giving 9.4 mM, 9.0 mM (+/-0.1mM), 8.7 mM (+/-0.2mM), 8.5 mM (+/-0.2mM) and 8.2 mM (+/-0.2mM) Fe for 0%, 0.5%, 1%, 2% and 5% Sb-bearing samples, respectively (Figure S5.2). Previous work has shown that Sb(V) is adsorbed to the surface of ferrihydrite via an inner-sphere surface complex with Sb-Fe bond distances of 0.31 nm and 0.351 nm (Mitsunobu et al., 2010). Thus, the decrease of bioavailable Fe concentration could be due to the formation of Fe-Sb complexes.

5.3.2 Bioreduction of Sb-bearing ferrihydrite

To identify the impact of Sb in Fe(III)-rich systems undergoing microbial reduction, Sb-sorbed ferrihydrites with a range of Sb loadings were challenged with cultures of *G. sulfurreducens* supplied with sodium acetate as the electron donor (Figure 5.1). Over the first 23 hours, compared to Sb-free ferrihydrite samples, low concentrations of Sb (0.5% and 1%) had little impact on microbial Fe(III) reduction. There was, however, a marked decrease in the rate and extent

of Fe(II) production at higher Sb concentrations (2% and 5%; Figure 5.1). The colours of the end point Fe-bearing minerals also varied, depending on the content of Sb (Figure 5.2). The colour of the starting material (ferrihydrite; dark reddish brown) in the Sb-free sample and the 0.5% Sb-bearing samples became progressively darker, whilst the colour of the high concentration Sb samples remained relatively unchanged. After 23 h, the rate of Fe(II) evolution in the 0% Sb and low Sb-bearing samples (0.5% and 1%) became slower and remained relatively constant at around 1.4 mM until the end of the experiment. After 116 hours, the bioreduction products in the Sb-free control, 0.5% and 1% Sb-bearing samples had to change to black and the residual products were magnetic, consistent with the bioconversion of ferrihydrite to the mixed Fe(II)/(III) mineral magnetite (Fe_3O_4) (Coker et al., 2006).

Interestingly, Fe(II) formation was most extensive in the 2% Sb-bearing samples increased over the duration of the bioreduction experiment, reaching approximately ~2.7 mM at the end of the 185 hour experiment (Figure 5.1). In figure 5.2(C), the solid residue from bioreduction of the 2% Sb-bearing samples was whitish yellow, at the end of the experiment indicating that magnetite was not the stable end point in these treatments. For comparison, the rate of Fe(II) increase was slowest in the 5% Sb-bearing samples, and the final mineral products were brown in colour. It is therefore suggested that different concentrations of adsorbed Sb(V) have a profound influence on the

bioreduction of ferrihydrite, impacting on the rate and type of secondary Fe-bearing minerals that form. No Fe(II) accumulated in the no cell control samples, confirming that Fe(III) reduction was microbially driven in this experiments.

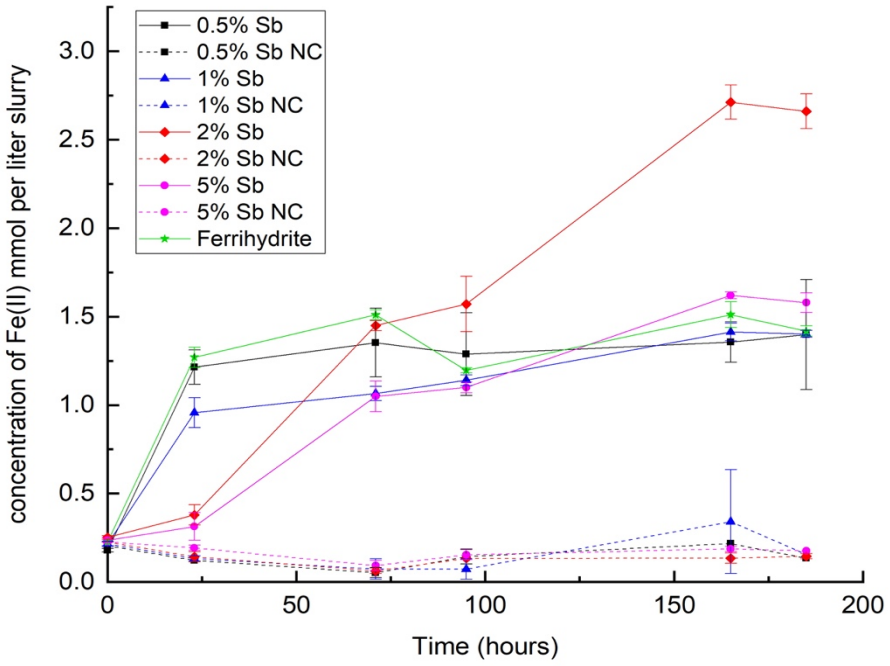

Figure 5.1 Production of Fe(II) in samples with 0% (solid green line), 0.5% (solid black line),1%(solid blue line), 2% (solid red line) and 5% (solid purple line) Sb during the reduction process by *G. sulfurreducens* and the changes of Fe(II) concentration in no cell control samples (black dotted line for 0.5% Sb no cell sample; blue dotted line for 1% Sb no cell sample; red dotted line for 2% Sb no cell sample; purple dotted line for 5% Sb no cell sample)

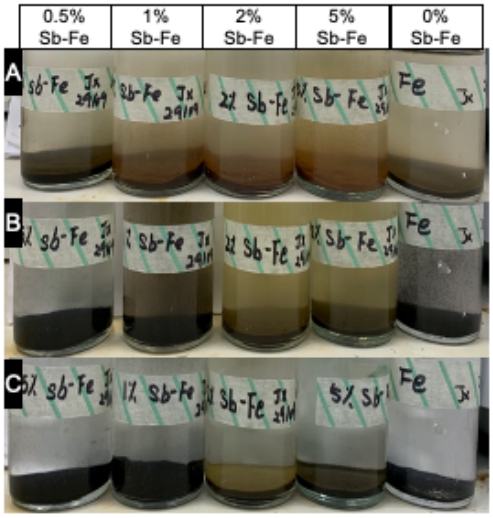

Figure 5.2 Changes in the colour of Fe(III) minerals containing different concentrations of Sb (0% 0.5% 1% 2% and 5% Sb wt%), during bioreduction by *G. sulfurreducens* (A 23 hours, B 116 hours and C 185 hours). The colours of ferrihydrite, magnetite, goethite and siderite are dark reddish brown, black, yellow-brown and white respectively (Schwertmann and Cornell, 2008).

5.3.3 Mineralogical characterization

XRD traces were collected from the mineral products of the ferrihydrite bioreduction experiments with different Sb loadings after 186 hours (Figure 5.3A). Consistent with visual appearance and magnetic properties reported above, the product of ferrihydrite reduction by *Geobacter sulfurreducens*, in the absence of Sb, was magnetite (Coker et al., 2006) (Figure S5.3). Magnetite was also the only crystalline product detected in the 0.5% Sb(V)-bearing sample, whereas for the 1% Sb-bearing sample, magnetite and goethite (α-FeO(OH) were both detected. For the 2% and 5% Sb-bearing samples, goethite was the main residual product with siderite ($FeCO_3$) also detected in the 2% Sb-bearing samples (Figure 5.3A). Therefore, with an increase in Sb content, the secondary iron minerals formed broadly contained progressively

less Fe(II), with the exception of the 2% sample which contained a fully reduced Fe(II)-bearing phase (siderite) and the amount of goethite in the products also increased with a concurrent relative decrease in magnetite content (with magnetite completely absent in 2% and 5% Sb-bearing samples). Figure 5.3B shows the XRD results of the products after aging in the bottles for 8 months; Figure 5.3B indicate the formation of siderite in all Sb-bearing experiments alongside the other minerals which were detected 10 days post reduction.

Previous studies have investigated the bioreduction of ferrihydrite to more stable Fe minerals, and noted that different factors such as pH, Fe(II) concentration, temperature and the presence of electron shuttles may all play a role (Byrne et al., 2011; Coker et al., 2008; Hansel et al., 2005; Schwertmann and Murad, 1983; Yee et al., 2006). Under neutral and near-neutral pH conditions, Fe(II) ions act as a catalyst for the transformation of ferrihydrite to goethite (Cornell and Schwertmann, 2003). However, if the Fe(II) concentration in the environment is higher and the pH is greater than 7, the end product will be Fe(II)-bearing minerals such as magnetite (Burton et al., 2019; Hansel et al., 2005). According to Coker et al. (2008), on the premise of excluding other interference factors, the final biological reduction product of ferrihydrite is magnetite. Goethite is an intermediate mineral formed during the microbial reduction of ferrihydrite, but is converted to magnetite due to

continued recrystallization in presence of biologically-produced Fe(II) (Coker et al., 2008). ICP-MS (not shown) data showed that Fe concentration in the supernatant remains low (<0.05 mM) throughout the microbial reduction process, indicating that no negligible Fe(II) was released into solution, consistent with the proposed role for biogenic Fe(II) sorbed to the mineral surface driving the reduction of Fe(III) minerals by *G. sulfurreducens* (Crosby et al., 2005). Siderite was found in the 2% Sb post-reduction products after 186 hours reaction and in all Sb-containing samples after prolonged (eight months) incubation. Siderite formation would take place when freely-available biologically-reduced Fe(II) ions reacted with sodium bicarbonate in the buffer solution to trigger precipitation, as follows:

$$Fe^{2+} + 2HCO_3^- \longrightarrow FeCO_3 + CO_2 + H_2O$$

Formation of siderite in the 2% Sb-bearing sample indicates that the Fe(II) produced at this intermediate loading of Sb was not incorporated into the evolving mixed Fe(II)/(III) mineral magnetite. This phenomenon was highly reproducible in our experiments, but the mechanism by which Sb at this loading promoted Fe(III) reduction, and disrupted the progression towards magnetite remains to be determined. It is possible to lower loadings of Sb were insufficient to promote this reaction, while the higher (5%) loading had a negative (toxic) impact on the cells nullifying any enhancement of Fe(III) reduction.

Magnetite (220) and (311) reflections from the XRD results (figure 5.3A) were

analysed by the Scherrer formula to calculate the crystallite size of the magnetite produced in the Sb-free and the 0%, 0.5% and 1% Sb-bearing samples. The results showed that the crystallite sizes of magnetite in Sb-free, 0.5% and 1% samples were 37 nm, 25 nm and 17 nm, respectively, indicating that with increasing Sb content, magnetite crystallite size became smaller.

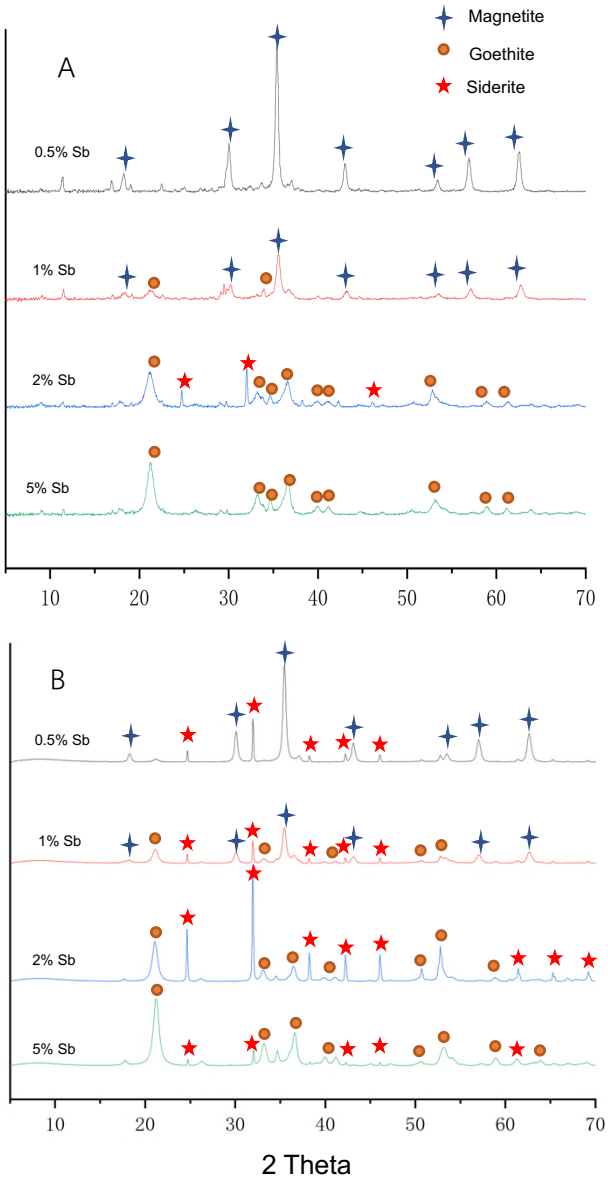

Figure 5.3 XRD results of post reduction of Fe minerals with different proportions of Sb bearing (0.5%,1%,2%,5%) after A) 186 hours reaction and B) 8 months long time reaction ★=magnetite, ●=goethite, ✦ =siderite

TEM images of post bioreduction products and their corresponding selected area diffraction patterns were collected from samples from this experiment (Figure 5.4). The identification of the minerals produced by microbial reduction reaction was consistent with the interpretation of the XRD data. Magnetite was only observed in the 0.5% and 1% Sb-bearing samples, and it is clear that the magnetite content in the 0.5% sample was much higher than that in 1% sample. According to the XRD data, the secondary Fe mineral in the 0.5% Sb-bearing samples was magnetite alone, but as shown in Figure 5.4A, small quantities of needle-shaped crystals were present and the diffraction results suggest the presence of a goethite (2 0 0) reflection (marked by red point).

The apparent absence of goethite in the XRD spectra was likely due to the amount of goethite produced being less than the XRD detection limits (~5%). However, the formation of goethite in the 0.5% Sb bearing samples suggests that the addition of Sb ions inhibits the formation of magnetite even though the Sb content was relatively small. The TEM diffraction data were also consistent with the bulk XRD data for the 1% 2% and 5% Sb samples, and backed up the crystallite sample size calculations across the sample set. For example the TEM results confirmed that the size of magnetite nanoparticles in the 0.5% and 1% Sb-bearing samples were around 22.8 nm (SD=4.1 nm) and 17.5 nm(SD=3.2 nm), respectively, similar to the calculations based on the XRD results. With the increased Sb contents, goethite grainsize was also seen to

increase. For the 1%, 2% and 5% Sb-bearing samples, the goethite crystal lengths were around 120, 150 and 250 nm, respectively, and the widths were ~ 10, 15 and 20 nm, respectively. The siderite produced in the 2% Sb-bearing samples exhibited grainsizes of up to $2\mu m$.

EDS results indicate that the distribution of Sb was closely related to the distribution of the Fe minerals, but did not seem to be closely related to the type of Fe mineral present; Sb concentrations were relatively uniform in the three kinds of Fe-bearing mineral detected (magnetite, goethite and siderite), with no obvious enrichment observed in any of these.(Figure S5.4A-S5.4E)

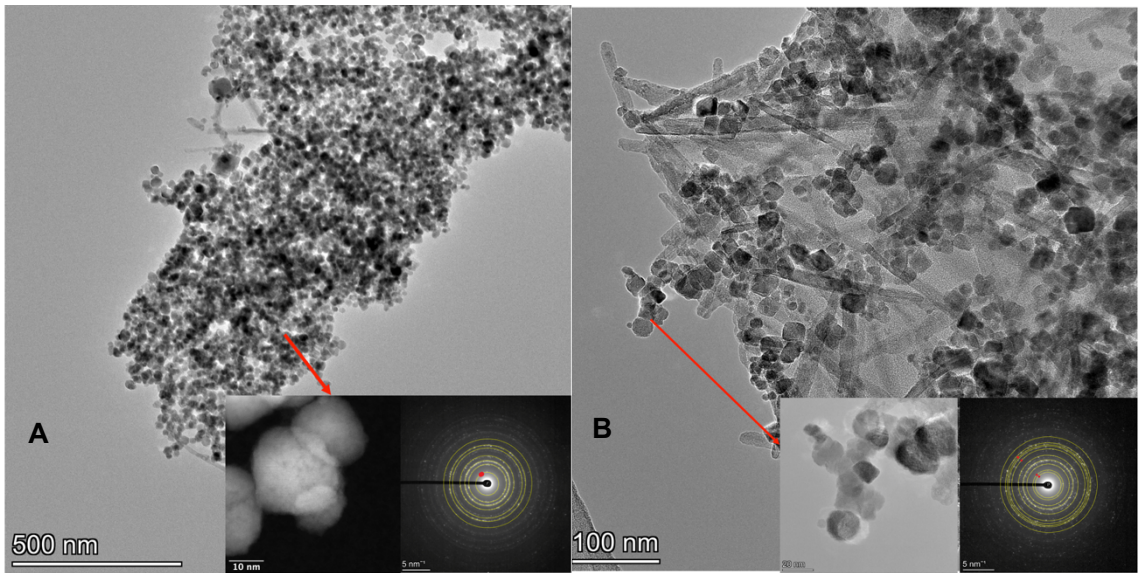

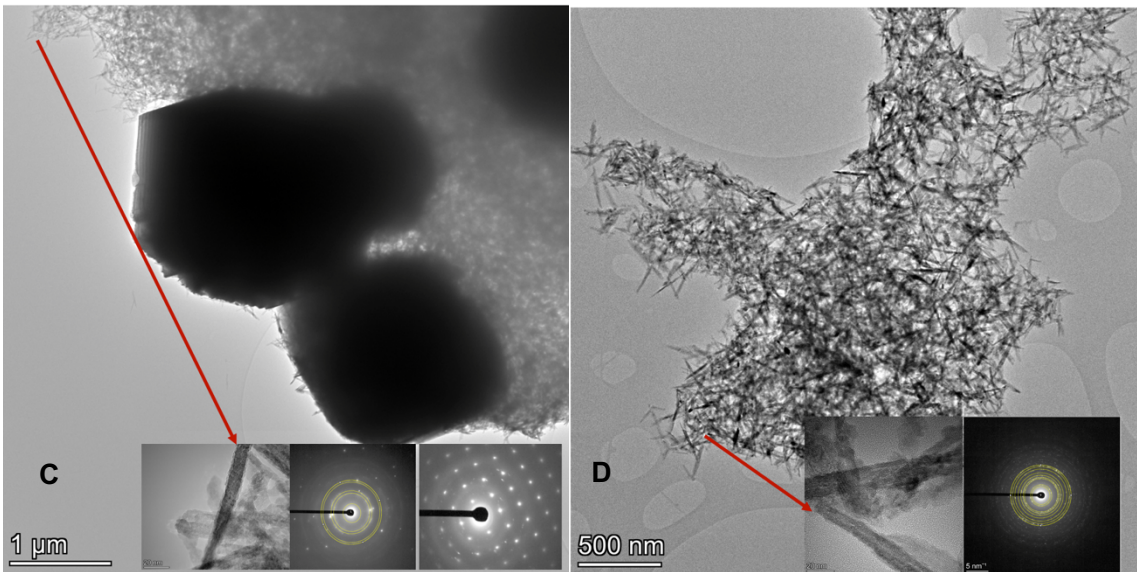

Figure 5.4 TEM images of A) 0.5% B) 1% C) 2% D) 5%Sb bearing post reduction products and their TEM diffraction results. Reflections belonging to Goethite have been marked with red dots to separate them from those of magnetite in A) 0.5% and B) 1% samples. There are two kinds of products in 2% Sb bearing sample, goethite is polycrystalline structure (concentric circles), siderite is single crystal structure (regular lattice arrangement). Their diffraction results are shown separately in picture C.

5.3.4 Immobilization and fate of Sb(V) in the post-reduction Fe minerals

The solubility of Sb during bioreduction of the Fe(III) host mineral was also monitored by ICP-MS. Although the bulk of the Sb was associated with the solid Fe(III) phase at the start of the experiment, residual soluble Sb was detected in solution phase (Figure 5.5). In all samples, this concentration of aqueous Sb(V) decreased during microbial Fe(III) reduction, and this process was more rapid in samples containing cells (OD_{600}=0.4) compared to cell-free control samples. The results of the control experiment without any Fe minerals added showed that after cells adding, the concentration of Sb in the solution was not decreased after 5 days which indicated that Sb ions were not adsorbed

by cells of *G. sulfurreducens* (Table S5.2); therefore, the continued decrease in Sb concentration was due to interactions with the Fe minerals in the system. For the 0.5%, 1% and 5% Sb-bearing samples, removal of the total Sb was very efficient at 99.5%, 99.4% and 99.4% after 186 hours of bioreduction, respectively. Incubations with the 2% Sb-bearing sample were unique, as there was a measurable increase in Sb release after 4 days, but 98.2% was still removed overall. The release of a small amount of Sb after bioreduction of the 2% sample could be linked to the altered pattern of post reduction minerals, dominated by siderite.

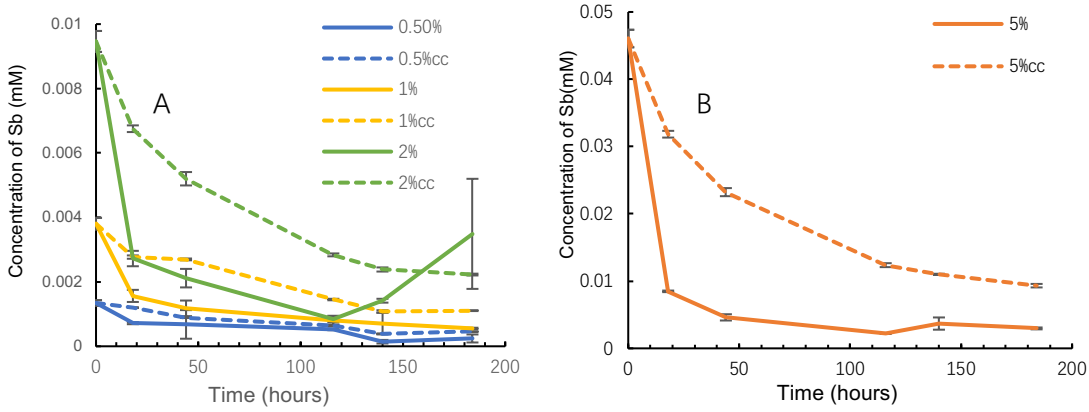

Figure 5.5 Changes in soluble antimony concentrations during bioreduction of 0.5% (solid blue line), 1% (solid yellow line) 2%(solid green line) (A) and 5% (solid orange line) (B) Ce-doped ferrihydrite samples, and the changes of soluble antimony concentrations in no cell control samples (blue dotted line for 0.5% Sb no cell sample; yellow dotted line for 1% Sb no cell sample; green dotted line for 2% Sb no cell sample; orange dotted line for 5% Sb no cell sample) cc means no cell control sample.

XPS was used to characterise Sb speciation in the initial and post-reduction materials. Figure S5.5 shows XPS spectra and associated fits of the Sb 3d and

O1s regions obtained from the pre- and post-reduction Fe minerals. According to the NIST XPS database and previous work (Caglar et al., 2018; Fan et al., 2014), Sb 3d lines can be used to identify Sb species, but the Sb 3d $_{5/2}$ peak coincides with O 1s, so the doublet separation was set to 9.5 eV between the Sb 3d $_{3/2}$ and Sb 3d $_{5/2}$ components, as the NIST database suggests, to obtain results for the Sb 3d $_{5/2}$ peak position. The resultant peaks are located at a binding energy (BE) of 529.5-530.0eV and 530.3 to ~531.8 eV, associated with Sb $3d_{5/2}$ of Sb(III) and Sb(V), respectively, and the BE of the Sb $3d_{3/2}$ for Sb(III) and Sb(V) are between 538.8–539.4 eV and 539.8–541.7 eV, respectively (Caglar et al., 2018; Fan et al., 2014).

The XPS patterns of the initial materials all fit well with two Sb 3d peaks and three O1s peaks. The binding energies of Sb $3d_{5/2}$ and Sb $3d_{3/2}$ peaks of all samples are reported in Table 5.1. The XPS results show that the binding energies of Sb $3d_{5/2}$ of 0.5%-5% Sb-bearing ferrihydrites were all around 530.2 eV to 531 eV, close to the standard value of Sb(V). Thus, the XPS results indicate that during Sb(V) adsorption from solution to ferrihydrite, Sb remains in the pentavalent state.

The binding energy of the Sb 3d peaks did not change significantly post-bioreduction, suggesting that there was no change in the redox state of the Sb during bioreduction. In the post-bioreduction 1% and 5% Sb-bearing samples,

the binding energy of Sb peaks decreases slightly (less than 0.2 eV). However, the peaks could not be accurately fitted with a mixture of both sets of peaks for the two valence states of Sb and all samples continued to fit best to just Sb(V), indicating no reduction of the Sb occurred during the experiment. It has been shown that under anaerobic conditions, Fe(II)-bearing minerals such as green rust, magnetite and mackinawite can reduce aqueous Sb(V) to Sb(III) through chemical redox reactions (Kirsch et al., 2008; Mitsunobu et al., 2008). However, in the present experiments, the Sb(V) was associated with the solid phase (rather than in solution) at the start of the experiment, and remained adsorbed or incorporated into the structure of Fe minerals (discussed below), plausibly explaining why Sb(V) was not reduced to Sb(III).

Table 5.1 The binding energies of Sb $3d_{5/2}$ and Sb $3d_{3/2}$ peaks of pre and post bioreduction Sb bearing Fe minerals

BE (eV)	Sb(III) Standards	Sb(V) Standards	0.5%Sb-bearing ferrihydrite	0.5%post reduction	1%Sb-bearing ferrihydrite	1%post reduction	2%Sb-bearing ferrihydrite	2%post reduction	5%Sb-bearing ferrihydrite	5% post reduction
Sb $3d_{5/2}$	529.5-530.0	530.3-532.1	530.4	530.7	530.3	530.3	531.0	531.0	530.9	530.7
Sb $3d_{3/2}$	538.8–539.4	539.8–541.7	539.9	540.2	539.8	539.8	540.5	540.5	540.4	540.2

The adsorption of antimony to iron oxyhydroxides is controlled by a range of factors, including mineral type, environmental pH and Sb speciation(Guo et al., 2014). The specific surface areas of ferrihydrite, goethite, akageneite and magnetite are reported to be 246, 32.1~52.1,108.6~135.7 and 95.2 m^2g^{-1}, respectively (Cutting et al., 2009; Schwertmann and Cornell, 2008; Sun et al.,

1998). With a pH of ~7, the maximum adsorption of Sb(V) by hydrous ferric oxide (ferrihydrite), akageneite and goethite can reach 544 (± 42.7), 165 (± 8.67) and 61.8 (± 2.06) μmol g^{-1}, respectively, and the molar adsorption densities (Sb(V):Fe) of ferrihydrite, akageneite and goethite are 0.058, 0.017 and 0.006, respectively (Guo et al., 2014). In the latter study, the adsorption efficiency of ferrihydrite for Sb(V) was thus around 10 times that of goethite. However, this is not consistent with our experimental results. We find that with formation of magnetite or goethite in the 0.5%-5% Sb-bearing samples, more Sb is removed from the solution compared to the initial ferrihydrite samples (figure 5.5). Guo et al. (2014) also noted that compared with Sb(V), the adsorption capacity of Fe(III) minerals for Sb(III) is higher under neutral conditions, but as our XPS data show, no Sb(III) was formed in our experiments. However, a key limitation for XPS is that detection depths are on the order of nm length scales. In order to mitigate against this limitation, sample grinding time was extended to 20 minutes, to try to ensure a homogenous mixture; however, the data still effectively reflects sample surface analyses (figure S5.5).

In addition to adsorption on the surfaces of Fe-bearing minerals, another possible reason for the decrease in antimony concentration in solution is that Sb(V) could be incorporated into the structure of the secondary Fe minerals. Mitsunobu et al. (2010) showed that compared with Sb(V) adsorbed goethite

and ferrihydrite, the peak intensities of Fe-Sb in EXAFS results of co-precipitated samples was higher, meaning that the coordination number of Fe-Sb was also larger. Therefore, during the co-precipitation of Sb(V) and goethite, Sb might be doped into the structure of the Fe minerals formed, replacing Fe(III) in the mineral structure(Mitsunobu et al., 2010). Support for the latter comes from Burton et al. (2019, 2020) and Hockmann et al. (2021), who used abiotic Fe(II) to catalyse the formation of goethite from ferrihydrite (with sorbed As(V)), and found that Sb(V) replaced some Fe(III) at octahedral positions in the goethite. The latter workers suggested that this was due to the similar ion sizes of Sb(V) and Fe(III) (around 0.06~0.065 nm) and the similar distances of the Fe-O and Sb-O bonds (around 0.2 nm) (Burton et al., 2020; Burton et al., 2019; Hockmann et al., 2021). It is plausible that the microbial transformation of Sb-adsorbed ferrihydrite to secondary Fe minerals observed here was similar to the co-precipitation process described above. With the microbial recrystallisation of the ferrihydrite, Sb(V) may be incorporated into the structure of the newly-formed minerals, resulting in additional Sb being incorporated into the solid phase and ultimately controlling the end product formed. This could also help explain why a small amount of Sb(V) was released in the 2% Sb-bearing sample; the siderite generated is an fully reduced Fe(II)-bearing mineral, and not likely incorporate the Sb(V) into the lattice structure.

5.4 Conclusion

In conclusion, this study shows that the Fe(III)-reducing bacterium, *G. sulfurreducens,* cannot directly reduce Sb(V) in solution, or associated with ferrihydrite, mirroring results obtained previously with As(V) (Islam et al., 2004) . Biogenic Fe(II) is also not able to reduce Sb(V) to the more environmentally toxic Sb(III), and the reduction of ferrihydrite laden with sorbed Sb(V) by *G. sulfurreducens* does not cause the release of Sb(V) into solution. Furthermore, Sb(V) seems to be associated with reduced Fe(II)-bearing phases, and surprisingly plays a role in controlling the type of Fe(II) mineral formed. The addition of different concentrations of Sb(V) greatly affects both the rate and end points of the bioreduction of ferrihydrite by *G. sulfurreducens*. An increase in the initial Sb(V) concentration led to the shift from magnetite production to the production of goethite (which was the intermediate product in magnetite biosynthesis), suggesting inhibition of the reduction process. Finally, the formation of a broad range of Fe minerals would seem to promote the immobilisation of Sb, offering relatively stable end products with Sb potentially incorporated into the mineral structure. This study highlights the tight coupling between Fe and Sb in environmental systems, suggesting that the microbial reduction of Fe(III)/Sb mineral assemblages may not lead to Sb release (in stark contrast to the mobilisation of As in iron rich systems).

Acknowledgments

Special thanks to Dr. Ben Spencer for helping us carry out XPS test on the samples and this work was supported by the Henry Royce Institute, funded through EPSRC grants EP/R00661X/1, EP/P025021/1 and EP/P025498/1. The authors would also like to thank Dr. John Water and Dr. Abby Ragazzon-Smith for their advice and assistance with XRD and ICP-MS analyses. The authors would also like to thank Mr Paul R. Lythgoe for his help with HPLC-ICP-MS analyses. Funding from NERC is also acknowledged (award NE/P01304X/1).

Reference

Burton, E. D., Hockmann, K. & Karimian, N. (2020). 'Antimony sorption to goethite: Effects of fe (ii)-catalyzed recrystallization' *ACS Earth and Space Chemistry*, 4 (3), pp. 476-487.

Burton, E. D., Hockmann, K., Karimian, N. & Johnston, S. G. (2019). 'Antimony mobility in reducing environments: The effect of microbial iron(iii)-reduction and associated secondary mineralization' *Geochimica et cosmochimica acta*, 245 pp. 278-289. DOI: 10.1016/j.gca.2018.11.005.

Byrne, J. M., et al. (2015). 'Scale-up of the production of highly reactive biogenic magnetite nanoparticles using *geobacter sulfurreducens*' *Journal of the royal society interface*, 12 (107), p. 20150240.

Byrne, J. M., et al. (2011). 'Control of nanoparticle size, reactivity and magnetic properties during the bioproduction of magnetite by *geobacter sulfurreducens*' *Nanotechnology*, 22 (45), p. 455709. DOI: 10.1088/0957-4484/22/45/455709.

Caglar, Y., Caglar, M. & Ilican, S. (2018). 'Xrd, sem, xps studies of sb doped zno films and electrical properties of its based schottky diodes' *Optik (Stuttgart)*, 164 pp. 424-432. DOI: 10.1016/j.ijleo.2018.03.017.

Charnock, J. M., et al. (2004). 'Role of metal-reducing bacteria in arsenic release from bengal delta sediments' *Nature*, 430 (6995), pp. 68-71. DOI: 10.1038/nature02638.

Coker, V., et al. (2006). 'Xas and xmcd evidence for species-dependent partitioning of arsenic during microbial reduction of ferrihydrite to magnetite' *Environmental science & technology*, 40 (24), pp. 7745-7750.

Coker, V. S., et al. (2008). 'Time-resolved synchrotron powder x-ray diffraction study of magnetite formation by the fe (iii)-reducing bacterium *geobacter sulfurreducens*' *American Mineralogist*, 93 (4), pp. 540-547.

Coppi, M. V., Leang, C., Sandler, S. J. & Lovley, D. R. (2001). 'Development of a genetic system for *geobacter sulfurreducens*' *Applied and environmental microbiology*, 67 (7), pp. 3180-3187.

Cornell, R. M. & Schwertmann, U. (2003). *The iron oxides : Structure, properties, reactions, occurrences, and uses*. 2nd, completely rev. and extended edn. Weinheim: Wiley-VCH.

Crosby, H. A., Johnson, C. M., Roden, E. E. & Beard, B. L. (2005). 'Coupled fe(ii)−fe(iii) electron and atom exchange as a mechanism for fe isotope fractionation during dissimilatory iron oxide reduction' *Environmental science & technology*, 39 (17), pp. 6698-6704. DOI: 10.1021/es0505346.

Cutting, R. S., et al. (2009). 'Mineralogical and morphological constraints on the reduction of fe(iii) minerals by *geobacter sulfurreducens*' *Geochimica et cosmochimica acta*, 73 (14), pp. 4004-4022. DOI: 10.1016/j.gca.2009.04.009.

Cutting, R. S., et al. (2012). 'Microbial reduction of arsenic-doped schwertmannite by *geobacter sulfurreducens*' *Environmental science & technology*, 46 (22), pp. 12591-12599.

EU (1998). 'Council directive 98/83/ec of 3 november 1998 on the quality of water intended for human consumption' *Official journal of the European communities*, 41 pp. 32-54.

Fan, J.-X., et al. (2014). 'Photo-induced oxidation of sb(iii) on goethite' *Chemosphere (Oxford)*, 95 pp. 295-300. DOI: 10.1016/j.chemosphere.2013.08.094.

Filella, M., Belzile, N. & Chen, Y.-W. (2002a). 'Antimony in the environment: A review focused on natural waters: I. Occurrence' *Earth-Science Reviews*, 57 (1-2), pp. 125-176.

Filella, M., Belzile, N. & Chen, Y.-W. (2002b). 'Antimony in the environment: A review focused on natural waters: Ii. Relevant solution chemistry' *Earth-science reviews*, 59 (1), pp. 265-285. DOI: 10.1016/S0012-8252(02)00089-2.

Filella, M., Belzile, N. & Lett, M.-C. (2007). 'Antimony in the environment: A review focused on natural waters. Iii. Microbiota relevant interactions' *Earth-science reviews*, 80 (3), pp. 195-217. DOI: 10.1016/j.earscirev.2006.09.003.

Gebel, T. (1997). 'Arsenic and antimony: Comparative approach on mechanistic toxicology' *Chemico-biological interactions*, 107 (3), pp. 131-144.

Guo, X., et al. (2014). 'Adsorption of antimony onto iron oxyhydroxides: Adsorption behavior and surface structure' *Journal of hazardous materials*, 276 pp. 339-345.

Hansel, C. M., Benner, S. G. & Fendorf, S. (2005). 'Competing fe (ii)-induced mineralization pathways of ferrihydrite' *Environmental Science & Technology*, 39 (18), pp. 7147-7153.

Hockmann, K., et al. (2021). 'Impact of antimony(v) on iron(ii)-catalyzed ferrihydrite transformation pathways: A novel mineral switch for feroxyhyte formation' *Environmental science & technology*, 55 (8), pp. 4954-4963. DOI: 10.1021/acs.est.0c08660.

Islam, F. S., et al. (2004). 'Role of metal-reducing bacteria in arsenic release from bengal delta sediments' *Nature*, 430 (6995), pp. 68-71.

Islam, F. S., et al. (2005). 'Interactions between the fe(iii)-reducing bacterium *geobacter sulfurreducens* and arsenate, and capture of the metalloid by biogenic fe(ii)' *Applied and Environmental Microbiology*, 71 (12), pp. 8642-8648. DOI: 10.1128/AEM.71.12.8642-8648.2005.

Karimian, N., Johnston, S. G. & Burton, E. D. (2017). 'Antimony and arsenic behavior during fe(ii)-induced transformation of jarosite' *Environmental science & technology*, 51 (8), pp. 4259-4268. DOI: 10.1021/acs.est.6b05335.

Kirsch, R., et al. (2008). 'Reduction of antimony by nano-particulate magnetite and mackinawite' *Mineralogical Magazine*, 72 (1), pp. 185-189.

Kulp, T. R., et al. (2014). 'Microbiological reduction of sb (v) in anoxic freshwater sediments' *Environmental science & technology*, 48 (1), pp. 218-226.

Li, J., et al. (2016). 'Microbial antimony biogeochemistry: Enzymes, regulation, and related metabolic pathways' *Applied and environmental microbiology*, 82 (18), pp. 5482-5495. DOI: 10.1128/AEM.01375-16.

Lloyd, J. R. (2003). 'Microbial reduction of metals and radionuclides' *FEMS microbiology reviews*, 27 (2-3), pp. 411-425.

Lovley, D. R., et al. (1993). '*Geobacter metallireducens* gen. Nov. Sp. Nov., a microorganism capable of coupling the complete oxidation of organic compounds to the reduction of iron and other metals' *Archives of microbiology*, 159 (4), pp. 336-344.

Lovley, D. R. & Phillips, E. J. (1986). 'Availability of ferric iron for microbial reduction in bottom sediments of the freshwater tidal potomac river' *Applied and Environmental Microbiology*, 52 (4), pp. 751-757.

Lovley, D. R. & Phillips, E. J. (1987). 'Competitive mechanisms for inhibition of sulfate reduction and methane production in the zone of ferric iron reduction in sediments' *Applied and Environmental Microbiology*, 53 (11), pp. 2636-2641.

Mitsunobu, S., Takahashi, Y. & Sakai, Y. (2008). 'Abiotic reduction of antimony(v) by green rust (fe4(ii)fe2(iii)(oh)12so4 · 3h2o)' *Chemosphere (Oxford)*, 70 (5), pp. 942-947. DOI: 10.1016/j.chemosphere.2007.07.021.

Mitsunobu, S., Takahashi, Y., Terada, Y. & Sakata, M. (2010). 'Antimony (v) incorporation into synthetic ferrihydrite, goethite, and natural iron oxyhydroxides' *Environmental Science & Technology*, 44 (10), pp. 3712-3718.

Polya, D. A., et al. (2003). 'Coupled hplc-icp-ms analysis indicates highly hazardous concentrations of dissolved arsenic species in cambodian groundwaters' *Plasma Source Mass Spectrometry: Applications and Emerging Technologies*. DOI: 10.1039/9781847551689-00127.

Schwertmann, U. & Cornell, R. M. (2008). *Iron oxides in the laboratory: Preparation and characterization*. John Wiley & Sons.

Schwertmann, U. & Murad, E. (1983). 'Effect of ph on the formation of goethite and hematite from ferrihydrite' *Clays and Clay Minerals*, 31 (4), pp. 277-284.

Sun, Z.-X., Su, F.-W., Forsling, W. & Samskog, P.-O. (1998). 'Surface characteristics of magnetite in aqueous suspension' *Journal of colloid and interface science*, 197 (1), pp. 151-159. DOI: 10.1006/jcis.1997.5239.

Telford, K., et al. (2009). 'Bioaccumulation of antimony and arsenic in a highly contaminated stream adjacent to the hillgrove mine, nsw, australia' *Environmental Chemistry*, 6 (2), pp. 133-143.

Terry, L. R., et al. (2015). 'Microbiological oxidation of antimony(iii) with oxygen or nitrate by bacteria isolated from contaminated mine sediments' *Applied and environmental microbiology*, 81 (24), pp. 8478-8488. DOI: 10.1128/AEM.01970-15.

USEPA (1999). National primary drinking water standards. United States Environmental Protection Agency Office

Wang, H., et al. (2013). 'Removal of antimony (sb(v)) from sb mine drainage: Biological sulfate reduction and sulfide oxidation–precipitation' *Bioresource technology*, 146 pp. 799-802. DOI: 10.1016/j.biortech.2013.08.002.

Wilson, S. C., Lockwood, P. V., Ashley, P. M. & Tighe, M. (2010). 'The chemistry and behaviour of antimony in the soil environment with comparisons to arsenic: A critical review' *Environmental pollution (1987)*, 158 (5), pp. 1169-1181. DOI: 10.1016/j.envpol.2009.10.045.

Yee, N., Shaw, S., Benning, L. G. & Nguyen, T. H. (2006). 'The rate of ferrihydrite transformation to goethite via the fe (ii) pathway' *American Mineralogist*, 91 (1), pp. 92-96.

Appendix S5

Table S5.1 The comparison of Sb(V) and total antimony contents in bioreduction process.(mixing 0.5mM Sb(V) with *G. sulfurreducens*)

	Sb(V) concentration(HPLC-ICP-MS)	Total Sb concentration (ICP-MS)
0.5mM Sb (day1)	0.53	0.51
0.5 mM Sb (day2)	0.52	0.50
0.5mM Sb (day5)	0.52	0.50

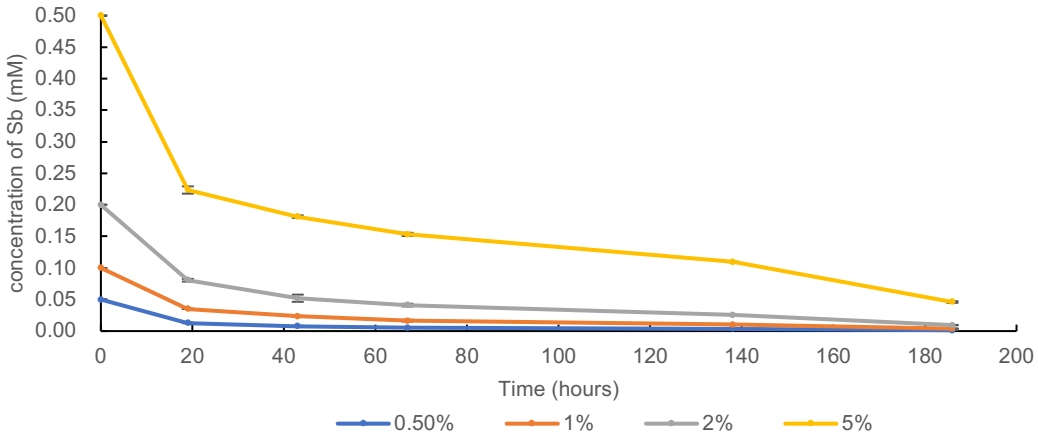

Figure S5.1 The changes of antimony concentration of 0.5%, 1%, 2% and 5% samples in the solution over the duration of the adsorption experiment. After 180 hours, the adsorption ratios of antimony reached nearly 97.3%, 96.2%, 95.3% and 90.8% for 0.5%,1%,2% and 5% Sb-bearing samples, respectively.

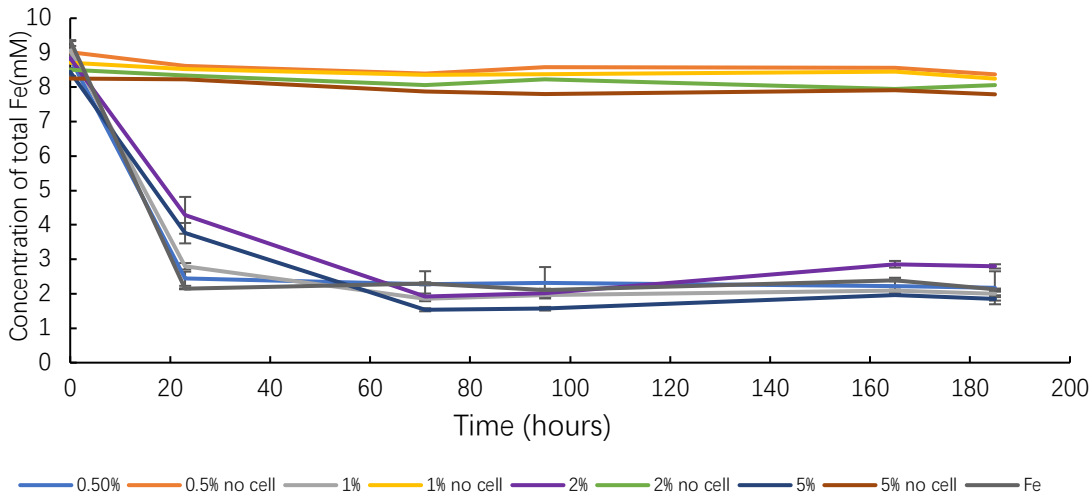

Figure S5.2 The line chart shows the change of Fe total concentration in samples with different antimony concentrations (0%,0.5%,1%,2% and 5% Sb) during the reduction process by *G. sulfurreducens* and the changes of Fe(II) concentration in no cell control samples.

Compared with the no Sb control samples, with the increase of initial antimony concentration, the total bioavailable iron concentration was predictably reduced after adsorption. 9.6 mM, 9.5 mM, 9.2 mM, 9.0 mM and 8.6 mM correspond to the total iron concentration of the no Sb sample 0.5%,1%, 2% and 5% Sb-bearing samples.

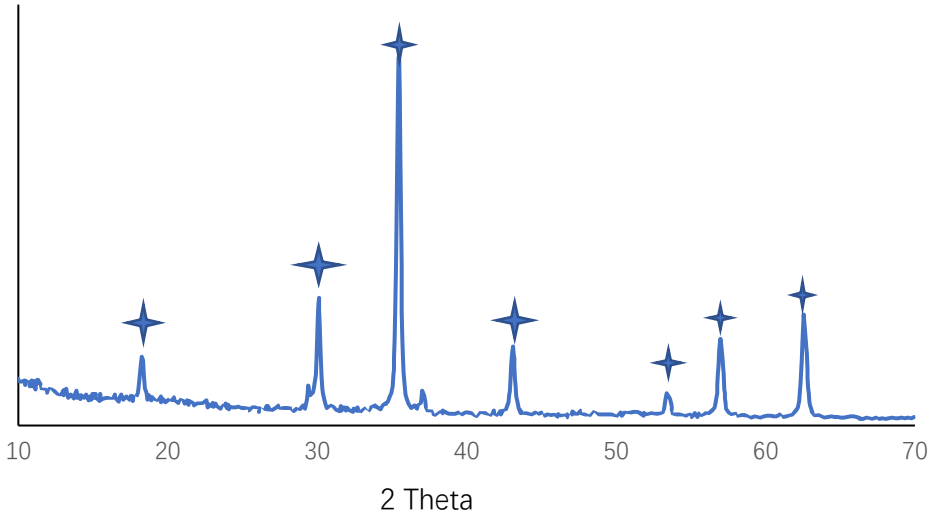

Figure S5.3 XRD results of post reduction of pure ferrihydrite and the results showed that the bioreduction product is pure magnetite ✦ =magnetite

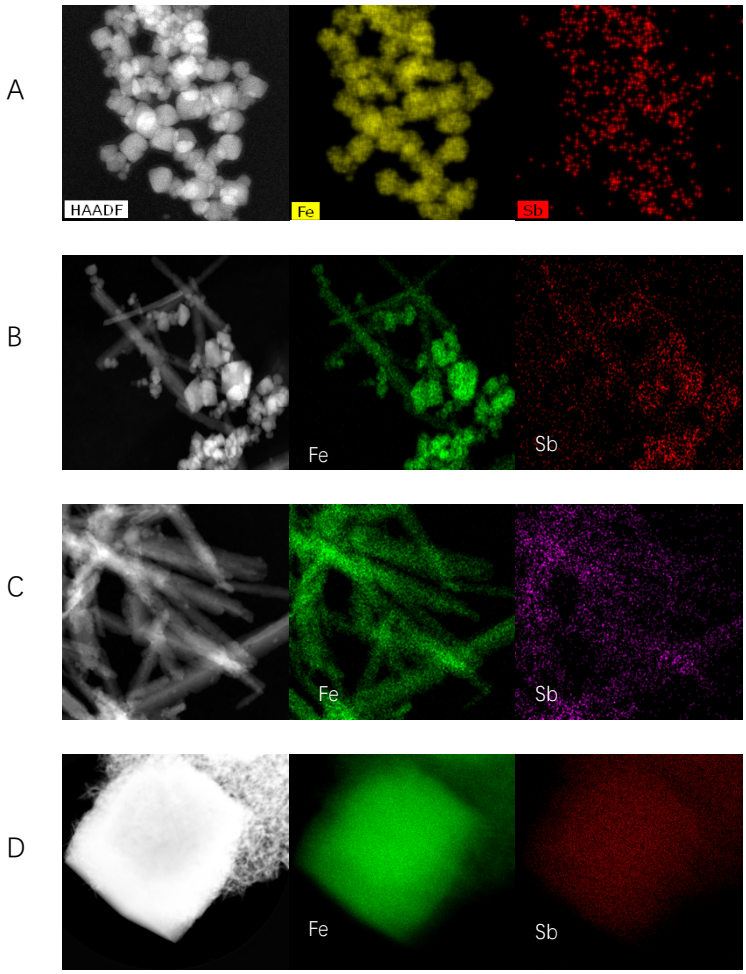

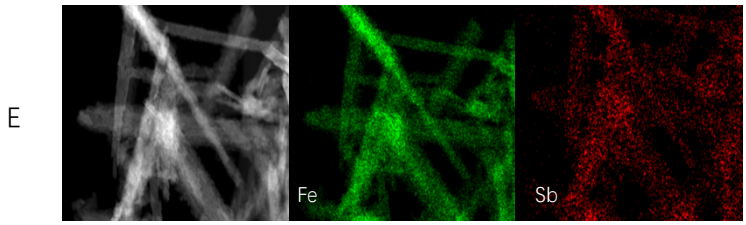

Figure S5.4 TEM HAADF and EDS images of A) 0.5% B) 1% C) and D)2% E) 5%Sb bearing post reduction products.

A: The bioreduction product of 0.5% samples was magnetite, the location of Fe has been marked as yellow and the location of Sb has been marked as red. B: The bioreduction product of 1% samples were magnetite and goethite, the location of Fe has been marked as green and the location of Sb has been marked as red. For 2% Sb bearing samples, the bioreduction products were goethite (C) and siderite (D). Because of the large size of siderite, the EDS results have been separated. C: Goethite, the location of Fe has been marked as green and the location of Sb has been marked as purple. D: Siderite, the location of Fe has been marked as green and the location of Sb has been marked as red. E: The bioreduction product of 5% samples was goethite, the location of Fe has been marked as green and the location of Sb has been marked as red.

Table S5.2 The ICP-MS results of the change of antimony concentration after mixing 0.5mM Sb(V) with *G. sulfurreducens* in the absence of ferrihydrite

	0 hour	3 hours	22 hours	46 hours	118 hours	142 hours	214 hours
Sb concentration (mM)	0.506803	0.477697	0.500704	0.506223	0.509832	0.496764	0.500486

The ICP-MS results showed after adding *G. sulfurreducens*, the concentration of antimony in the solution kept stable (around 0.5mM), which indicated that *G. sulfurreducens* cannot adsorb Sb(V) directly. So the decrease in antimony concentration shown in the experiment was due to the Fe minerals rather than bacteria.

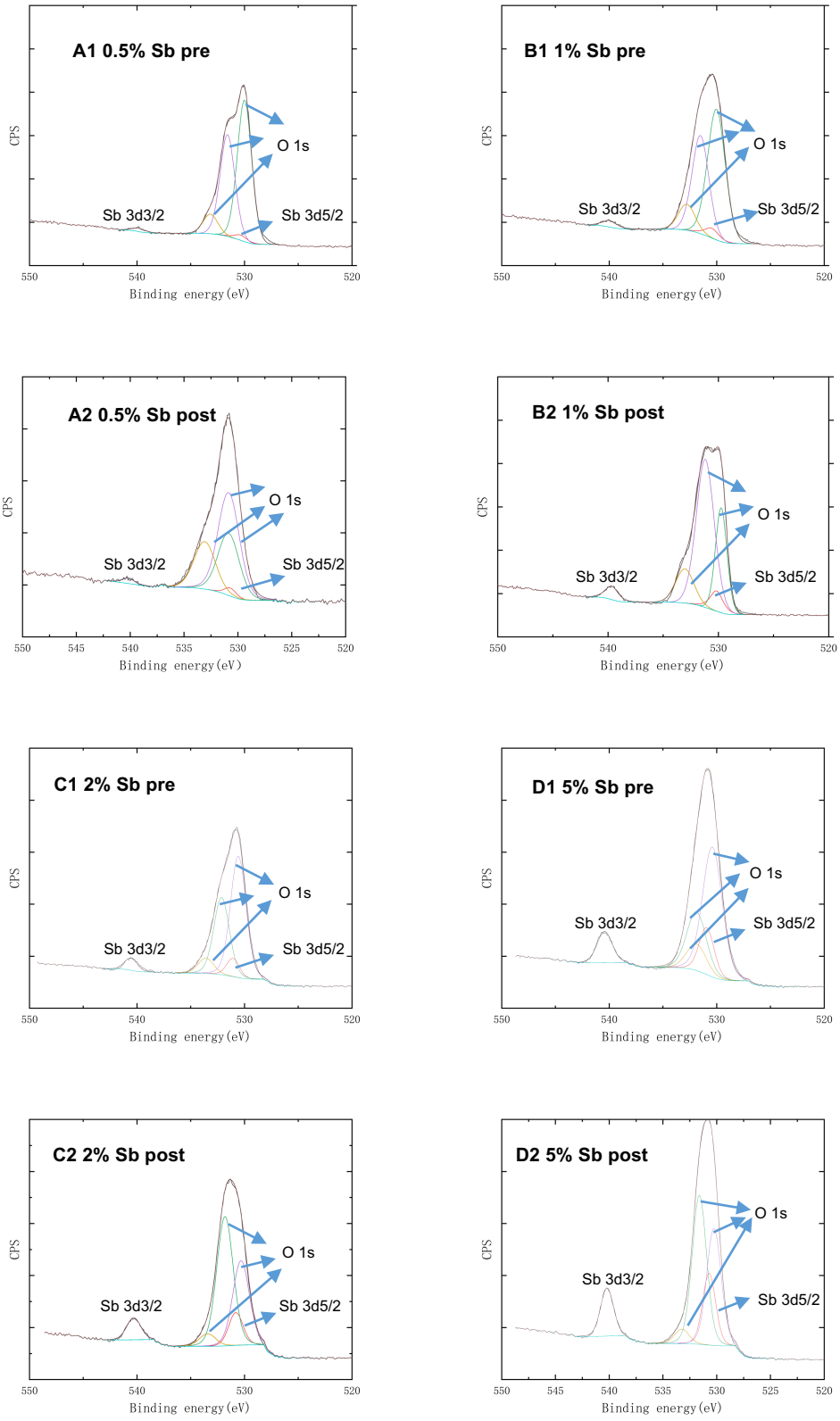

Figure S5.5 XPS spectra and fits of the Sb3d and O1s regions obtained from the pre- and post-reduction Fe minerals.

Sb 3d3/2 regions locate at around 540 eV and Sb 3d5/2 regions locate at around 530.5 eV.

The black line is the detected data, the bule line is background, and the red line is the fitted data. A1: 0.5% Sb pre reduction samples: 0.5% Sb bearing ferrihydrite; A2: 0.5% Sb post reduction samples: 0.5% Sb bearing magenetite;B1: 1% Sb pre reduction samples: 1% Sb bearing ferrihydrite;B2: 1% Sb post reduction samples: 1% Sb bearing magnetite and goethite; C1: 2% Sb pre reduction samples: 2% Sb bearing ferrihydrite; C2: 2% Sb post reduction samples: 2% Sb bearing goethite and siderite; D1: 5% Sb pre reduction samples: 5% Sb bearing ferrihydrite; D2: 5% Sb post reduction samples: 5% Sb bearing goethite.

Chapter 6 :
The formation of platinum group metal (PGM) nanoparticles by *Geobacter sulfurreducens* and application to catalysis

Jinxin Xie, Victoria S. Coker, Brian O'Driscoll, Christopher Egan Morriss, Jonathan R. Lloyd

This chapter is a manuscript in preparation for journal publication. Supporting information submitted with this manuscript is included in Appendix S6.

Chapter 6: The formation of platinum group metal (PGM) nanoparticles by *Geobacter sulfurreducens* and application to catalysis

Jinxin Xie, Victoria S. Coker, Brian O'Driscoll, Christopher Egan Morriss, Jonathan R. Lloyd

Abstract

There is much interest in the bioreduction and biorecovery of platinum group metals (PGM), and the application of biological PGM nanoparticles in high-performance catalysis. In this study, a key metal-reducing microorganism, *Geobacter sulfurreducens,* was used to bioreduce both mono PGM solutions (Palladium (Pd(II)), Platinum (Pt(IV)), Rhodium (Rh(III)) and Ruthenium (Ru(III)) and two-PGM mixed solutions (Pd+Pt, Pd+Rh and Pd+Ru) to form nanoparticles. Palladium, Platinum and Rhodium were all reduced and formed metallic nanoparticles (2.7-3.8 nm) associated with the bacterial cells. In addition, mixed PGM systems of Bio-PdPt and Bio-PdRh likely contained alloys, while compared to mono metallic PGM particles, the alloys formed were smaller in size (2.6-2.8 nm), resulted in less agglomerate formation and were more evenly dispersed over the surface of the bacteria. The nanoparticles were all found to be active as catalysts in the 4-nitrophenol reduction reaction, and the Bio-Pd and the Bio-PdPt alloys exhibited the highest catalytic abilities. This study shows that *G.sulfurreducens* has an untapped ability for the biorecovery of PGM, and the biorecovery products have high catalytic capacities, with potential applications in a range of catalytic reactions.

6.1 Introduction

The platinum group metals (PGM) include platinum (Pt), palladium (Pd), rhodium (Rh), ruthenium (Ru), iridium (Ir) and osmium (Os) and usually behave as siderophile and chalcophile elements in natural magmatic settings (O'Driscoll and González-Jiménez, 2016). The elements contained in PGE ores are often reported as '4E' (Pt+Pd+Rh+Au) or '6E' (Pt+Pd+Rh+Ru+Ir+Au) grades (Mudd, 2012; Mudd et al., 2018). The economic value of platinum group metals (PGM) is high because of their limited natural abundances (around 10^{-6}–10^{-7}% in the Earth's crust) (Barkov and Zaccarini, 2019; Sahu et al., 2021) and diversity of uses.

The PGM have long been used in jewellery, and now more recently have found wide application as chemical process catalysts, vehicle catalysts, hydrogen fuel cells, electronic components, and as investment commodities (Mudd, 2012). The Bushveld Igneous Complex in South Africa dominates the world supply of PGM as it is host to the largest reserves, including 75% of Pt, 54% of Pd and 85% of Rh resources (Mpinga et al., 2015; Naldrett et al., 2008; Sahu et al., 2021). Russia, Canada, Zimbabwe and the United States all have PGM-rich mines, such as the Norilsk–Talnakh field (Russia), Sudbury (Canada), Great Dyke (Zimbabwe) and the Stillwater Complex (USA) (Maksimainen et al., 2010; Mudd, 2012; O'Driscoll and González-Jiménez, 2016). However, since the mid-to-late 1980s no new PGM primary deposits have been discovered (Koek et al.,

2010). Therefore, in order to achieve sustainable development, it is necessary to recover and reuse the PGM. Research on recovery of the PGM from wastes can not only supplement supply of PGM, but also can reduce the potential hazards of platinum-based metals in the environment.

The PGM are found in wastes such as mining wastes (leachates and soil residues), e-wastes and spent catalysts; these can cause serious environmental contamination problems. The PGM can accumulate in soil, sediments and enter the human body via the biological food chain (Cinti et al., 2002). Previous research has shown that with an increase in the PGM in the environment, the risk of biological accumulation in the human body is also increased (Ek et al., 2004; Ravindra et al., 2004), and according to the Environmental Health Criteria from the World Health Organisation (WHO), Pt, Pd, and some Pd salts are all common allergens which can cause skin and eye irritations (Ek et al., 2004; Melber et al., 2002).

Studies on the biorecovery of the PGM have become a focus for recent research. Halophilic mixed cultures, *Desulfovibrio desulfuricans, Shewanella algae, Pseudomonas sp., Geobacter sulfurreducens* and other organisms have all shown an ability to recover Pd or/and Pt (Butu et al., 2016; Liang and Gadd, 2017; Nancharaiah et al., 2016; Tuo et al., 2013). *Desulfovibrio desulfuricans* was found to reduce a Pd(II) model solution to Pd(0) nanoparticles, with

pyruvate, formate and H_2 acting as electron donors (Lloyd et al., 1998). Other research focused on the use of metallised cells (Pd- *Escherichia coli* MC 4100 and Pd- *Desulfovibrio desulfuricans*) to recover Pd and Pt nanoparticles from the acidic solutions with H_2 as electron donor (Creamer et al., 2006; Murray et al., 2017). However, most research to date has focused on the bioreduction of Pd and/or Pt rather than the other PGM (Rh, Ru, Os and Ir). H_2 was used as electron donor in many biorecovery processes of PGM, but as a strong reducing agent, most of the PGM will be directly reduced by hydrogen in the reduction process, resulting in the size and position of the generated nanoparticles changing (Yong et al., 2002). The dissimilatory metal-reducing bacterium, *Geobacter sulfurreducens,* is well-known to reduce metal ions such as Fe(III), Co(III) and U(VI) (Byrne et al., 2013; Coker et al., 2006; Lloyd, 2003; Lloyd et al., 2000; Lovley et al., 1987) at circumneutral pH, however, there is little published research using this organism to biorecover PGM (Tuo et al., 2013; Yates et al., 2013; Zhuang et al., 2015).

The aim of this study is to test whether *Geobacter sulfurreducens* can biorecover the PGM in both single metal and mixed PGM solutions. The types of nanoparticles generated were analysed by a suite of techniques including X-ray diffraction (XRD), Transmission Electron Microscopy (TEM) and X-ray Photoelectron Spectroscopy (XPS). PGM nanoparticles were tested for catalytical ability using the model 4-nitrophenol catalytic reduction reaction. The

application of biorecovery to PGM-bearing wasteforms has wide implications, not only for improving resource supply but also for reducing the amount of associated environmental waste and PGM making their way into the food chain.

6.2 Materials and Methods

6.2.1 Preparation of PGMs stock solution

Pd(II), Pt(IV), Rh(III) and Ru((III) stock solutions (50 mM) were prepared using sodium tetrachloropalladate, sodium hexachloroplatinate, ruthenium chloride hydrate and rhodium chloride hydrate, each dissolved in DIW, in 10ml volumetric flasks. Solutions were stored in a fridge at 4 ℃, and covered by aluminum foil to protect from light.

6.2.2 *Geobacter sulfurreducens* growth

NBAF medium containing sodium acetate (20 mM) as the electron donor and fumarate (40 mM) as the electron accepter was prepared (Coppi et al., 2001). *G. sulfurreducens* was incubated at 30℃ in NBAF medium anaerobically for 2-3 days before being harvesting. All manipulations were performed under 80:20 mix of N_2:CO_2 gas lines to remove oxygen. The fresh *G.sulfurreducens* cells were harvested from the NBAF growth medium. The culture was centrifuged at 4920 *g* and 4℃ for 20 minutes and washed with 30mM $NaHCO_3$ solution of pH7 another two times. The harvested cells were then resuspended in $NaHCO_3$ solution and flushed by 80:20 mix of N_2:CO_2 before use in the bioreduction

experiments.

6.2.3 Bioreduction experiments of PGM

PGM solution (0.2 mM), sodium acetate (10 mM) and sodium bicarbonate (30 mM) were added to serum bottles. An 80:20 mix of N_2:CO_2 was used to flush each bottle for at least 0.5 hours and the pH was adjusted to 6.8-7. Harvested cells suspensions were added to each bottle to achieve a final OD_{600} of 0.4. Controls either without cells or without an electron donor were also set up. All bottles were incubated at 30 ℃ and sampled at 1 hour, 2 hours, 4 hours, 24 hours and 48 hours.

For the mixed PGM bioreduction experiments, 0.1 mM of either Pt, Rh or Ru was added to bottles containing 0.1 mM Pd. The above biological reduction process was repeated for the mixed PGM experiments.

6.2.4 Catalyst experiments

Typically, 31.25 µL of 10 mM 4-nitrophenol solution and 1 mL of 62.5 mM $NaBH_4$ were added into a quartz cuvette containing 1.97 mL of DIW. Then, 125 µL of bio-PGMs suspension was pipetted into the above solution to initiate the reaction, which was performed at room temperature (around 22 °C). The cuvette holder was placed onto an orbital shaker at 100 rpm. The reaction process was recorded using a UV-Vis spectrophotometer (Bruker), with spectra collected in the range 200-600 nm at 0, 0.75, 1.5, 3, 5, 10, 20, 40, and 60

minutes. The concentration of 4-nitrophenol was determined from the absorbance at 400 nm, for which a standard calibration curve was determined from the 4-nitrophenol stock solution.

6.2.5 Real Pd sample experiments

1 ml of a solution containing acid digested Pd wire (0.05 M HCl) was mixed with 8.9 ml 30 mM $NaHCO_3$ solution and 0.1 ml of a 1M sodium acetate stock solution in each bottle. The mixture was then flushed by an 80:20 mix of N_2:CO_2 for 30 minitues to adjust the pH to 7.0 and remove the dissolved oxygen. A washed cell suspension of *G. sulfurreducens* was prepared as above (Section 6.2.2) and an aliquot added to each bottle to achieve a final OD_{600} of 0.2.

6.2.6 Instrumental analysis

The concentrations of PGM in the solution were quantified with an Agilent 8800 Triple Quadrupole Inductively coupled plasma mass spectrometer (ICP-MS). During each monitoring point, 0.3 ml of solution was sampled and centrifuged at 14800*g* for 20 minutes. After centrifuging, 0.1 ml clear supernatant was taken and mixed with 9.9 ml 2% HNO_3 for ICP-MS analysis. The prepared samples were stored in a cold room before analysis. The pH of the samples was also measured.

X-ray diffraction (XRD) using a Bruker D2 Phaser diffractometer at Department

of Earth and Environment Science was employed to identify the mineralogy of the PGM at the end of the experiment. This XRD instrument has a Lynxeye XE-T detector, an axial 2.5º Soller slit and anti-scatter screen. It operated at 30 kV and 30 mA with a copper X-ray source which provide Cu Kα1 X-rays (λ=1.5406 Å). The scan range was set from 5-70º 2θ with a step size of 0.04 º and 0.4 s per step. EVA version 5 with the ICDD (International Centre for Diffraction Data) Database was used to process the XRD results. Approximately 3-5 ml of each PGM sample was taken and centrifuged at 14800*g* for 20 minutes to collect the precipitate, which was washed in DIW twice to remove salts. The washed precipitates were mixed with 1 ml amyl acetate and transferred to a low background Si wafer and air dried before scanning.

X-ray Photoelectron Spectroscopy (XPS) was performed using an Axis Ultra Hybrid spectrometer (Kratos Analytical, Manchester, United Kingdom) using monochromated Al Kα radiation (1486.6 eV, 10 mA emission at 150 W, spot size 300 x 700 μm) with a base vacuum pressure of ~5×10^(-9) mbar. Charge neutralisation was achieved using a filament. Binding energy scale calibration was performed using C-C in the C 1s photoelectron peak at 285 eV. Analysis and fitting was performed using Voigt-approximation peaks using CasaXPS. Around 10 ml of the PGM solution was centrifuged at 14800*g* for 20 minutes and washed by DIW twice. The washed samples were then resuspended in a small amount of DIW and dripped onto a silicon wafer for drying.

Transmission Electron Microscopy (TEM) images were collected by a Tecnai T20 with 200 kV accelerating voltage and STEM (Thermo Fisher, Titan, G2 80–200) which is equipped with Energy Dispersive X–ray Spectroscopy (EDS) detector and a high angle annular dark field (HAADF) detector operating with an inner angle of 55 mrad at 200 kV. PGM samples were collected and centrifuged at 14800 rpm at 30 minutes and then washed by DIW for 3 times. The washed PGM nanoparticles were then resuspended in DIW and diluted to nearly colourless solutions before drop-casting onto a copper grid coated with an amorphous carbon film.

6.3 Results and discussion

6.3.1 Bioreduction of monometallic PGM solutions

Single-metal PGM solutions were exposed to *Geobacter sulfurreducens* to identify and constrain bioreduction processes. Approximately 80% Pd was removed during the first two hour of the reaction, and at 24 hours nearly 89% of the Pd was removed (Figure 6.1a). As the reaction progressed, the colour of the solution changed from golden (Figure 6.2a) to black (Figure 6.2b), indicating the potential formation of Pd(0) nanoparticles. In the no cell control samples, at 24 hours, nearly all Pd was removed from the solution, but a yellow precipitate formed rather than a black one. According to previous research, Pd(II) is a hydrolysable metallic ion (Baes Jr and Mesmer, 1976; Boily et al., 2007) and

colloid particles are formed in Pd(II) salts when pH is between 5-6 (Troitskii et al., 1993). Therefore, a yellow precipitate in Pd no cell control samples could be Pd(II) hydroxocomplexes due to the pH neutral environment in this experiment.

Bioreduction of Pt and Rh were similar to Pd in that more than 95% of Pt and Rh ions were removed from solution within the first hour (Figure 6.1b&c). The colour of both samples (Pt and Rh) changed from initially colorless to black (Figure 6.2 c,d & e,f). In the no cell control samples, the concentration of aqueous Pt and Rh barely changed over the course of the reaction, indicating a microbially driven reaction in the main experiment. Unlike Pd, Pt and Rh, before adding cells, the concentration of Ru in the solution immediately decreased by more than 92% after 0.2 mM Ru was added (Figure 6.1d) and formed visible small black particles at neutral (Figure 6.2g). However, compared to the Ru no cell control sample, larger sized and agglomerated precipitates were produced after 24 hours after adding the cells and the colour of the solution changed to colourless in Ru with cell sample (Figure 6.2h). The added *G.sulfurreducens* may have an adsorption effect on the resulting Ru particles and thus facilitate the aggregation of the products to form larger particles. The formation of the aggregations could be due to the extracellular polymeric substances (EPS) from *G. sulfurreducens* because the previous research show that EPS can promote the aggregation of solid particles (Costa

et al., 2018; Stöckl et al., 2019).

The black particles formed could be a hydroxide of Ru(III), due to the low pH of Ru(III) hydrolysis (Baes Jr and Mesmer, 1976; Boily et al., 2007; Troitskii et al., 1993; Wyatt, 1966). According to previous research, when the initial concentration of Ru(III)Cl_3 is 0.1mM and 0.001mM, precipitates of ruthenium(III) hydroxide may form at pH 2.42 and 4.42, respectively (Povar and Spinu, 2016). In addition, in the experiments of Kim and Popov, $RuCl_3.xH_2O$ and $NaHCO_3$ were used to synthesis amorphous hydrous ruthenium oxide particles at pH 5 (Kim and Popov, 2002), using the same initial materials as the present experiment.

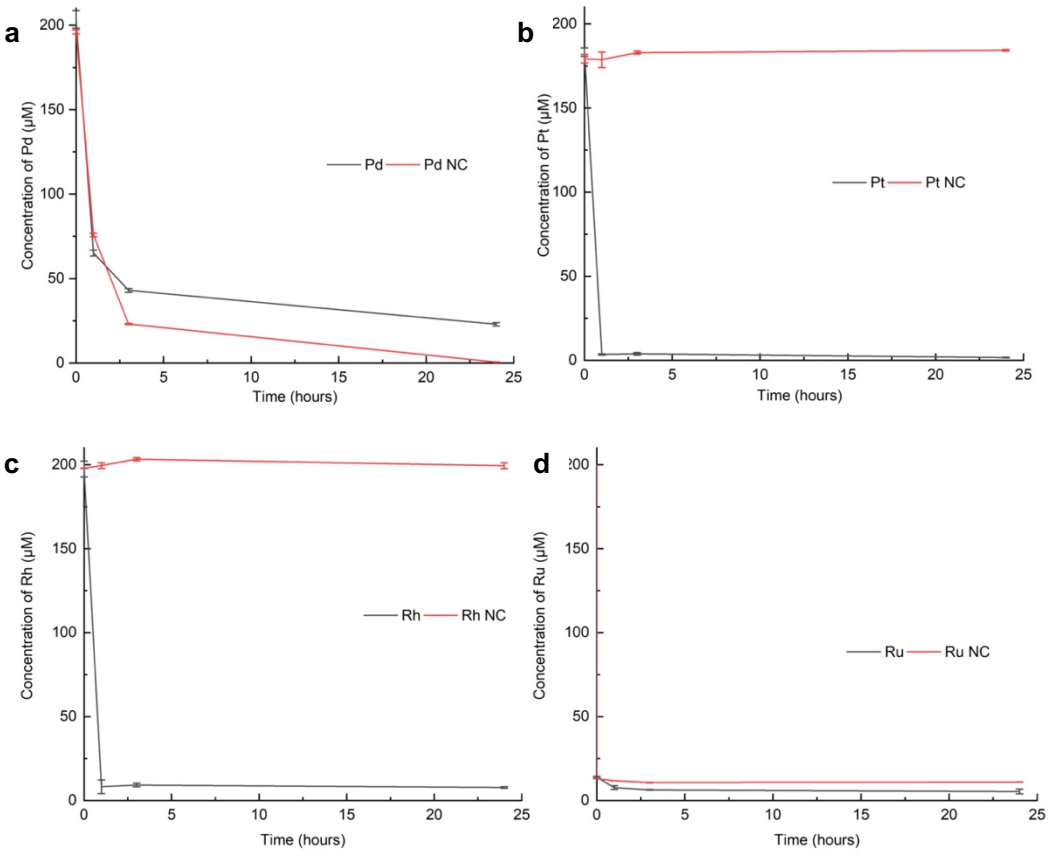

Figure 6.1 Changes of aqueous PGMs concentrations during the bioreduction processes by *G.sulfurreducens* a) Pd, b) Pt, c) Rh, d) Rh. NC represent the no cell controls

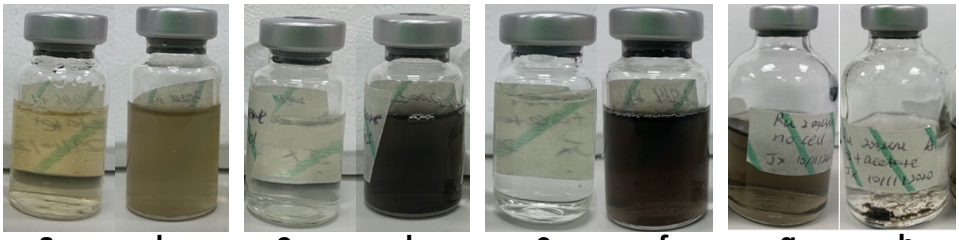

Figure 6.2 Photographs of serum bottles containing different PGM before adding cells (0 hour) and 24 hours after microbial reaction. **a** Pd(II) 0 hour. **b** Pd 24 hours after microbial reaction. **c** Pt(IV) 0 hour. **d** Pt 24 hours after microbial reaction. **e** Rh(III) 0 hour. **f** Rh 24 hours after microbial reaction. **g** Ru(III) 0 hour. **h** Ru 24 hours after microbial reaction.

The XRD patterns of post reduction precipitates of the PGM by *G.sulfurreducens* give reflections at 40.1 and 46.7(2θ), indicative of the (111) and (200) planes of Pd(0); 39.9 and 46.2 (2θ) of Pt(0); 41.1 and 47.8 (2θ) of Rh(0). The (111) and (200) planes of Pd(0) Pt(0) and Rh(0) are present in the results, while only the Pt(0) pattern contains a distinct (220) reflection (67.5 (2θ)) (Figure 6.3). These results suggest that *G.sulfurreducens* is able to reduce high valance states of aqueous Pd, Pt and Rh ions to their metallic nanoparticles. No peaks were detected in the XRD pattern of any Ru precipitates. As mentioned above, the hydrolysis products of $RuCl_3$ is ruthenium hydroxide at room temperature are disordered and no peaks can be detected by XRD (Kim and Popov, 2002; Zheng and Jow, 1995). The Scherrer formula was used to calculate the crystallite sizes of PGM metallic nanoparticles from the (111) reflections. The results showed that the crystallite sizes of Pd(0), Pt(0) and Rh(0)

nanoparticles were 3.76 nm, 3.61 nm and 2.80 nm, respectively.

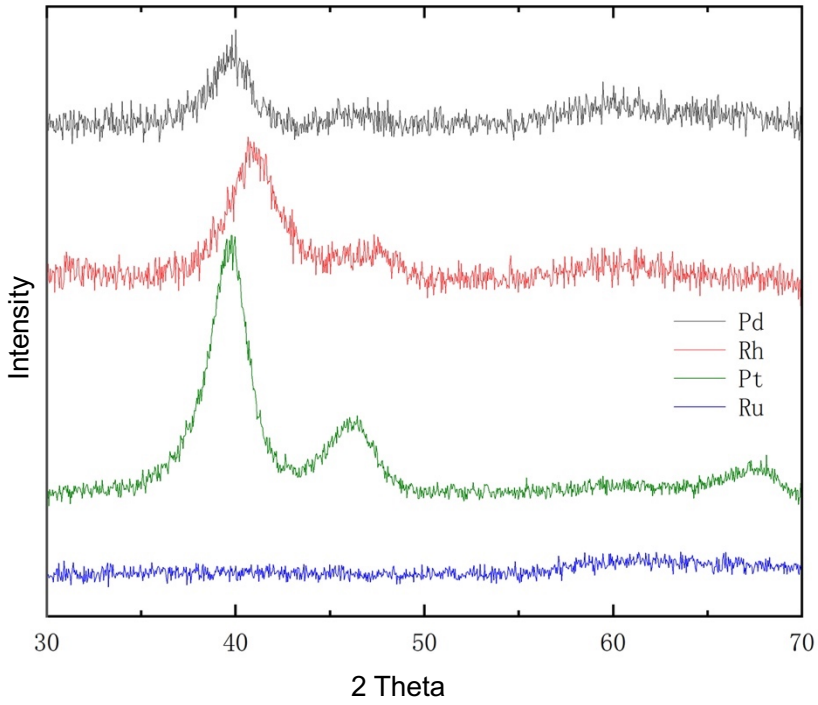

Figure 6.3 XRD patterns of post reduction products of Pd, Pt, Rh and Ru samples

The morphology, distribution and particle size of the PGM nanoparticles formed was analysed by TEM (Figure 6.4). The TEM results on size analysis and material identification of the post reduction products were generally consistent with the XRD results. Pd(0) (111), (200) and (220) reflections (marked as yellow cycles) were present in TEM selected area diffraction (SAED), suggesting the formation of metallic Pd(0) nanoparticles (Figure 6.4a). Pd(0) nanoparticles were distributed on the surface of *G.sulfurreducens* and the average size of individual particle was 3.76 nm (SD=0.49 nm) (Figure 6.4b).

For the Pt samples (Figure 6.4c,d), the TEM SAED results confirm the formation of Pt(0) nanoparticles. According to particle size analyses using ImageJ

software, the average size of Pt(0) nanoparticles was 3.28 nm (SD=0.47 nm), which was slightly smaller than the crystallite size from the XRD results (3.61 nm). Pt(0) nanoparticles clumped together and formed irregularly-shaped aggregates of different sizes (tens to hundreds of nanometers) on the surface of *G.sulfurreducens,* differing in both morphology and distribution to those observed in the Pd results (Figure 6.4a). The TEM results for the Bio-Pt(0) nanoparticles were similar to previous work showing snowflake-shape spots of Pt(0) were formed on the surface of *Shewanella oneidensis* MR-1 (Tuo et al., 2017).

TEM SAED confirmed the presence of Rh(0) from identification of the (111), (200) and (220) reflections. The average size of the particles generated was 2.73 nm (SD=0.45 nm). The morphology of the Rh(0) nanoparticles produced was similar to those of Pt, but compared to Pt(0), the size of the Rh(0) aggregates was smaller, around 50 nm. However, according to previous research, the distribution of Bio-Rh(0) can be both extracellular and intracellular (Ngwenya and Whiteley, 2006; Tamaoki et al., 2013). Rh(0) aggregates generated in the present experiment appear to be enveloped by cell membranes (Figure 6.4e), but the current results and TEM images reported here are not sufficient to fully confirm the location of the products. For the Ru samples, the SAED of precipitates gave no result, similar to the XRD, which was again thought to be due to the poor crystalline structure of ruthenium (hydro)

oxide particles described above. Compared to the TEM image of no-material coated *G.sulfurreducens* control samples (Figure 6.4i), substances without fixed form which adhered to each other, were adsorbed to the surface of *G.sulfurreducens* in Ru(III) with cell sample. Figure 6.2h suggests that, compared to the no cell control sample, the ruthenium (hydro)oxide particles formed could be resuspended with the cell samples due to adsorption by *G.sulfurreducens.*

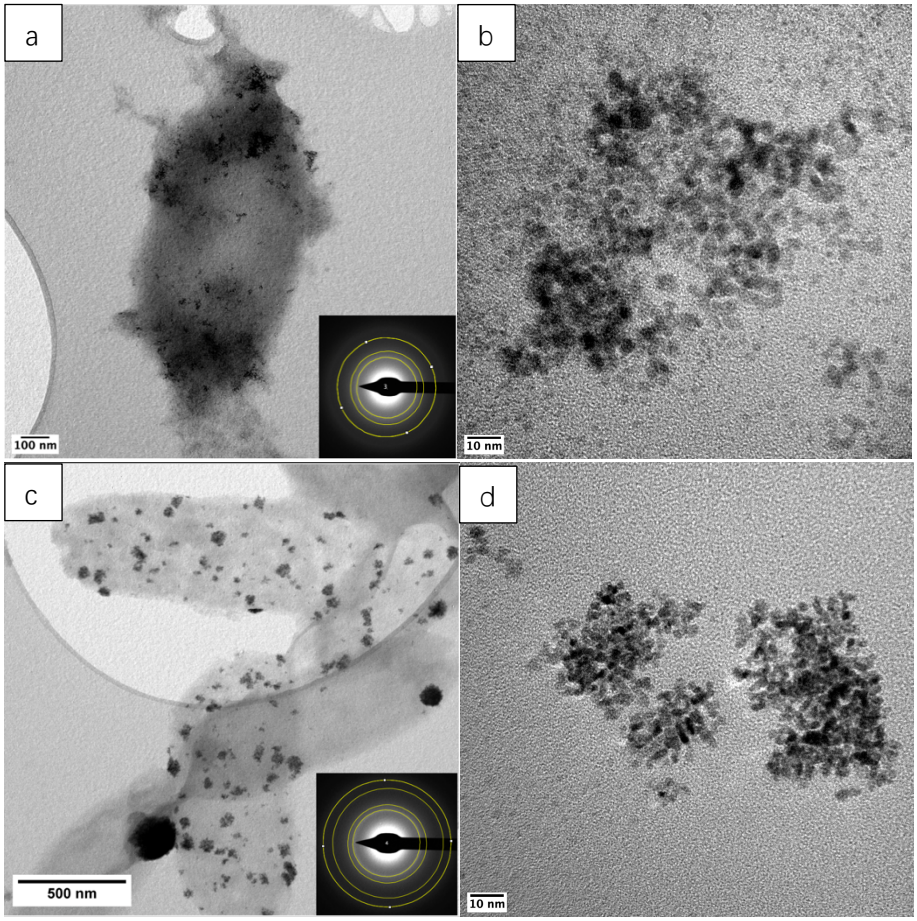

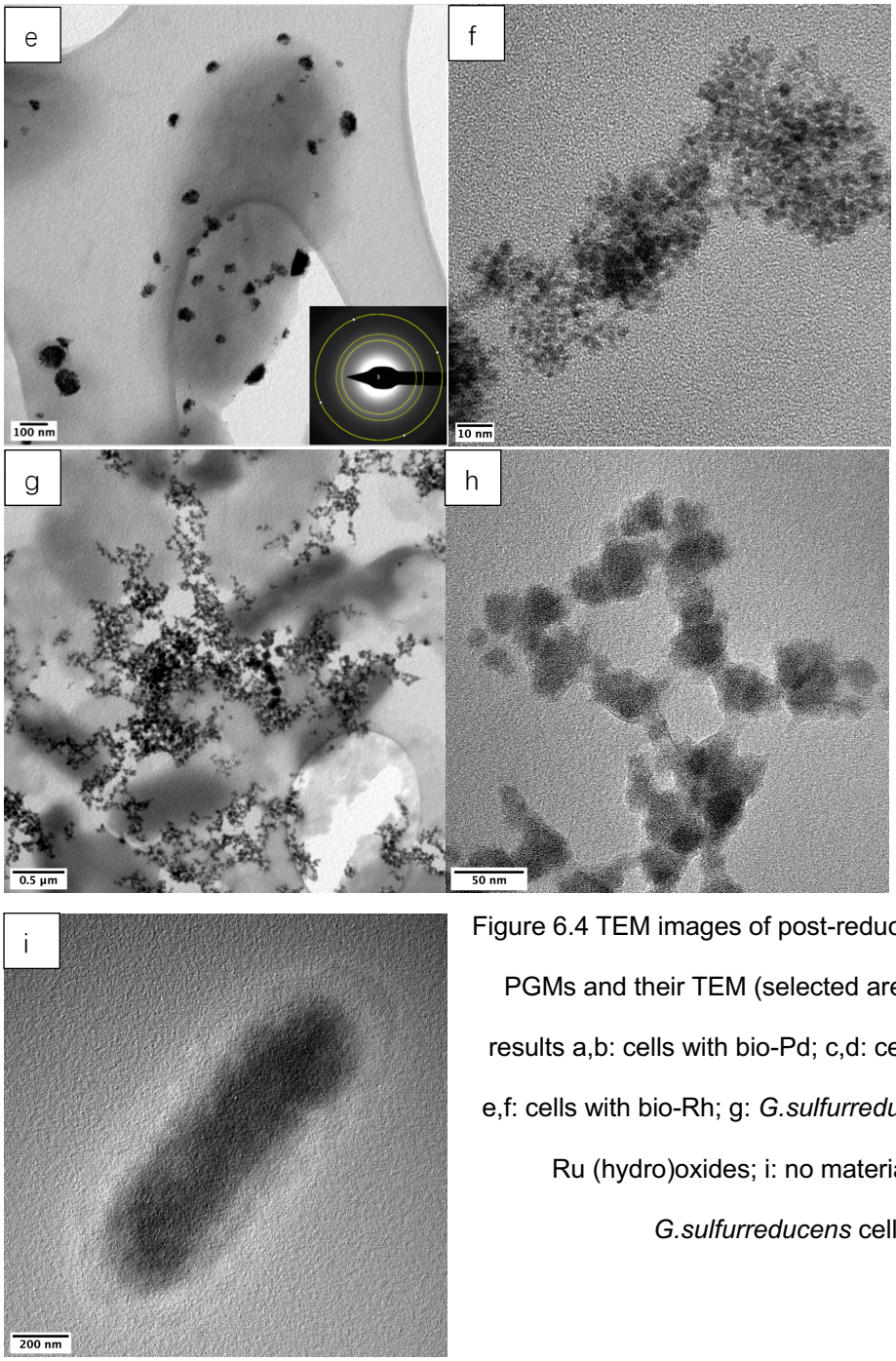

Figure 6.4 TEM images of post-reduction products of PGMs and their TEM (selected area) diffraction results a,b: cells with bio-Pd; c,d: cells with bio-Pt; e,f: cells with bio-Rh; g: *G.sulfurreducens* cells with Ru (hydro)oxides; i: no material coated *G.sulfurreducens* cell

The valence states and surface compositions of the PGM were analysed by XPS (Figure 6.5). Pd 3d and Pt 4f peaks were doublet separated for different valance states of Pd and Pt. The binding energies of Pd(II) (3d3/2=342.2-343.7eV, 3d5/2=335.2-338.2 eV), Pd(0) (3d3/2=339.3-341.1 eV, 3d5/2=335.1-335.8), Pt(IV) (4f5/2=77.8-78.9 eV, 4f7/2= 74.5-75.6eV) ,Pt(II) (4f5/2=75.9 eV,

4f7/2= 72.4-73.6eV) and Pt(0) (4f5/2= 74.2-75.0eV, 4f7/2=70.7-71.7 eV) were collected from NIST XPS data base and previous studies (Tuo et al., 2017; Xu et al., 2018). Pd XPS results confirmed the formation of Pd(0) nanoparticles and their dominance in the product (Figure 6.5a). XPS for the Pt precipitates reveal 32% Pt(II) rather than Pt(IV) in the post reduction products, indicating that all of the Pt(IV) had been reduced during the microbial activities, of which 32% was only reduced to Pt(II). No Rh and Ru peaks were observed in the XPS spectra which, in the case of Rh where precipitates were measured using XRD and TEM, might be due to the surface sensitivity of XPS (usually around 2-3 nm) and the location of formed Bio-Rh(0) potentially within the cell membrane.

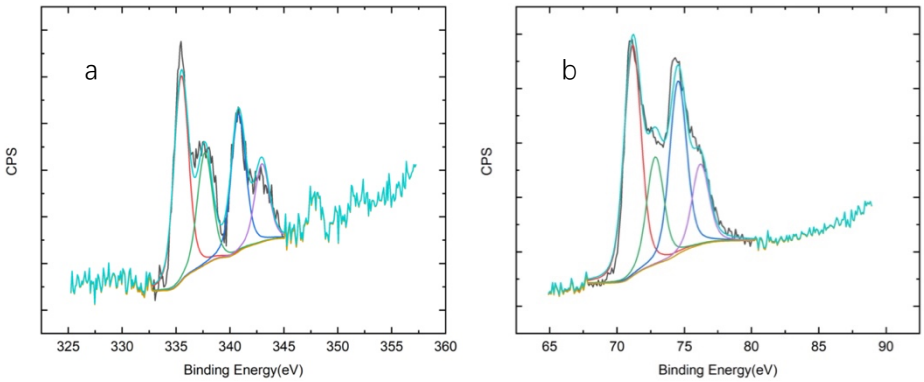

Figure 6.5 XPS spectra (black) and the fitting curves (blue) of the post reduction products; **a.** Pd; **b.** Pt.

6.3.2 The bioreduction of bimetallic PGM samples

G.sulfurreducens was used to reduce mixed Pd-X (X: Pt, Rh or Ru) samples (Figure 6.6). Compared to mono Bio-Pd or Bio-Pt results (Figure 6.1 a &b), the amount of Pd and Pt removed from solution was less in the Pd-Pt mixed sample, with only ~ 40% of Pd and 60% of Pt removed during the first hour, compared

~ 70% of Pd and 95% of Pt in the mono PGM bioreduction experiments. During the bioreduction of the Pd-Pt solution, the colour of the sample rapidly changed to black. At 24 hours, 80% Pd in the Pd-Pt mixed sample was removed from solution while the comparable value was ~90% in the mono Pd bioreduction process. Nucleation onto the surface of the bacteria and reduction potential can influence the formation of PGM nanoparticles (Tuo et al., 2015). The reduction potential of Pt(IV) is 0.92 V which is higher than 0.775 V of Pd(II) (Li et al., 2012; Qu and Dai, 2005; Tuo et al., 2017). In addition, previous research had shown that more nucleation sites are used for the formation of Bio-Pd nanoparticles than Pt(IV) while the formation of Bio-Pt nanoparticles also takes up some nucleation sites, which could cause the lower reduction precipitation efficiency of Pd in Pd-Pt mixed sample (Tuo et al., 2017). The no cell control sample results were similar to the mono Bio-Pd and Bio-Pt bioreduction results, suggesting that the formation of black material in Bio-PdPt sample is still a microbial driven process.

For the Bio-Pd-Rh samples, the colour of the mixtures changed to black rapidly after the addition of the bacterial cells. The removal of Rh from solution was similar to that for the mono Rh bioreduction results (Figure 6.1c), with more than 95% Rh removed from solution within the first hour, though the experiment continued for the next 2 days. The final concentration of aqueous Pd in the Pd-Rh system was only $18\mu\mathrm{M}$, equating to 90% removal (Figure 6.6b), similar to

the Bio-Pd reduction results. The results of the Pd-Ru bioreduction experiments show rapid precipitation of Ru in both the cell-bearing samples and the no cell control sample. In contrast to the Pd-Pt and Pd-Rh experiments, around 20% of the Pd in the Pd-Ru sample was also precipitated immediately at neutral, with the final removal value at over 95% Pd (Figure 6.6c).

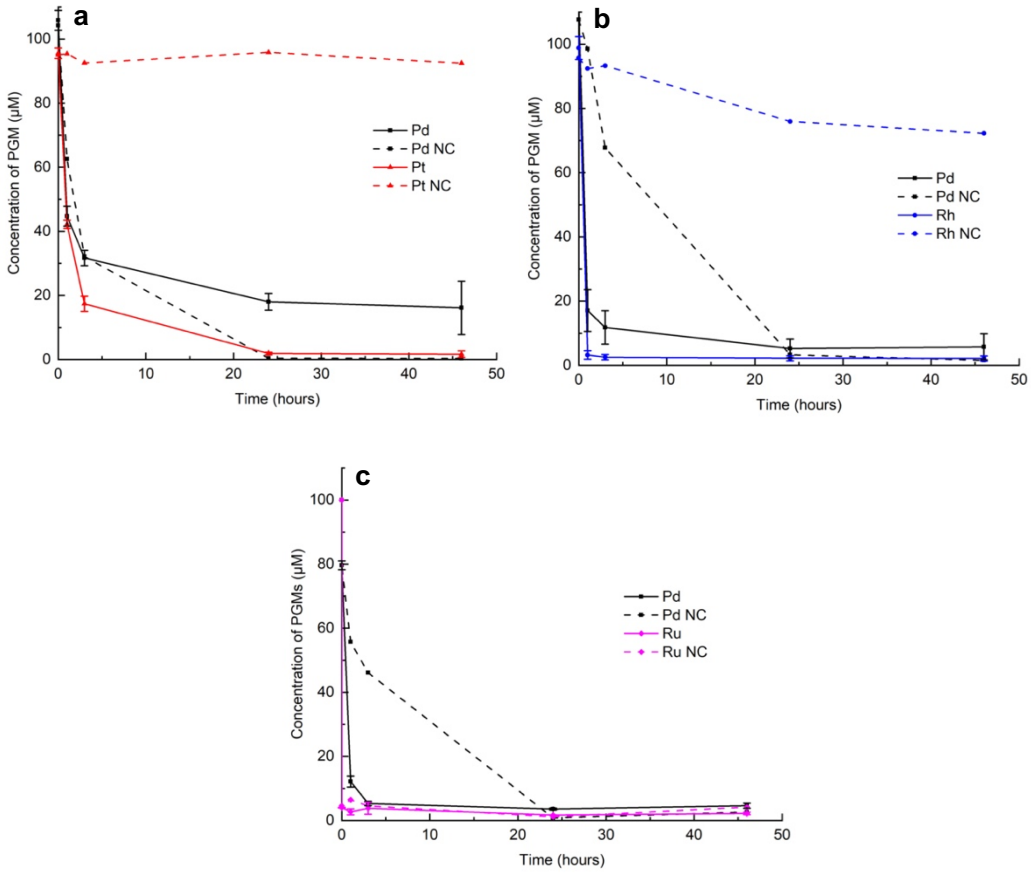

Figure 6.6 Changes of aqueous PGMs concentrations during the bioreduction processes of Pd-X mixed by *G.sulfurreducens* a) Pd-Pt, b) Pd-Rh, c) Pd-Ru; NC represent the no cell controls

Bimetallic Pd-X samples were analysed by XRD and the (111) diffraction peaks of each sample are shown in Figure 6.7. According to the ICDD database, (111) peaks of pure Pd(0), Pt (0) and Rh(0) were located at 40.2, 39.7 and 41.0 (2θ),

respectively. The position of the Bio-Pd-Pt (111) is 39.9 (2θ), sitting between the (111) values for Pd(0) and Pt (0). The shape of the (111) diffraction peak is intact, indicating no overlap of the two peaks (Figure 6.7), in turn suggesting that the bioreduction process formed a Bio-Pd-Pt alloy, rather than two discrete monometallic nanoparticles. Additionally, the XPS results for the Bio-Pd-Pt samples (Figure S6.1) suggested the formation of Pd(0) and Pt(0), although only 30% of Pd was reduced on the surface; which was much lower than the result for the mono Bio-Pd reduction result (~65%). In contrast, the Pt XPS result shows around 74% Pt was reduced to Pt(0) in the Bio-Pd-Pt samples, signifying a 10% increase in the proportion of Pt(0) compared to the mono Pt reduction. The latter observation might be explained by the formation of Pd(0) and Pt(0) nanoparticles on *G. sulfurreducens*. The initially formed Pd(0) and Pt(0) particles could have acted as catalysts for the abiotic reduction of Pd(II) and Pt(IV); previous studies had shown that the catalytic effect of Pt(IV) reduction is more effective than that of Pd(II) (Tuo et al., 2017).

From the XRD data for the Pd-Rh experiment precipitate, the (111) peak is located between the position for (111) Pd(0) and Rh(0) (40.1 and 40.3 (2θ)), indicating that Pd-Rh alloy may also have formed during the reduction process. The XPS results indicated the formation of 82% Pd(0) (Figure S6.1 B2). In contrast to the XPS result for mono Bio-Rh (which did not give a signal), 76% Rh(0) was detected by XPS in the Bio-Pd-Rh sample, suggesting the location

and morphology of the formed Rh(0) in the mixed Bio-Pd-Rh samples was different to that in the mono Bio-Rh sample (no signals). For the Pd(0)-Ru sample, there were no well-defined peaks in the XRD data. The XPS result indicated the formation of Pd(0), but the peaks for Ru were not detected by either XRD or XPS (Figure S6.1 C).

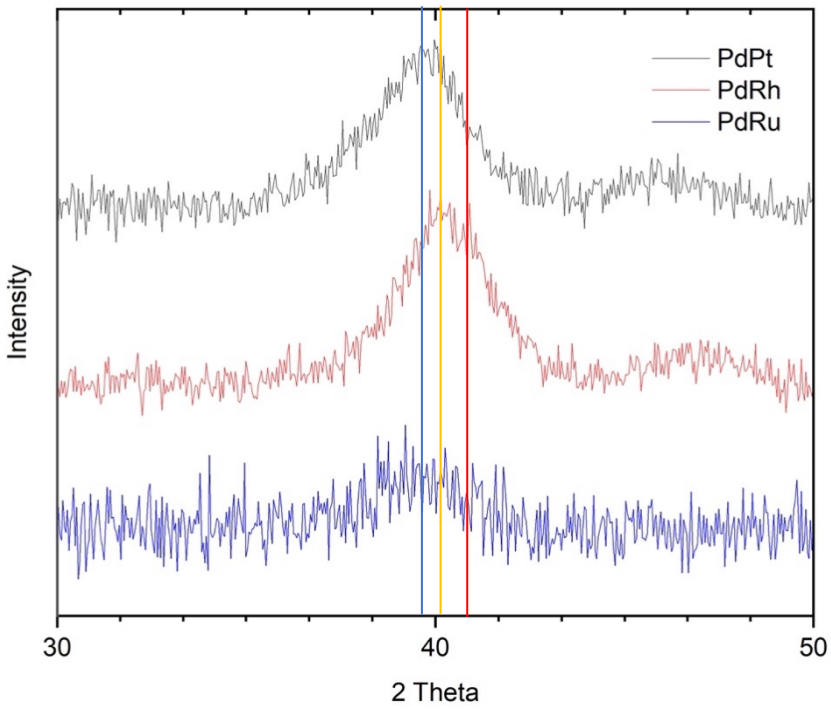

Figure 6.7 XRD patterns of (1 1 1) reflection of different samples (Pd-Pt, Pd-Rh, Pd-Ru) in 2 theta range of 30°~50 °. The standard (111) of Pd(0), Pt(0) and Rh(0) were marked by yellow, blue and red lines.

The size, morphology and location of the bioreduction products of the Pd-X samples were analysed by TEM and TEM EDS mapping (Figure 6.8). Compared with the mono PGM bioreduction products, the sizes of the nanoparticles of Bio-Pd-Pt and Bio-Pd-Rh formed were smaller, and the distribution of the nanoparticles formed on the *G.sulfurreducens* surface were

also more uniform. For the Bio-Pd-Pt nanoparticles, the average size of the nanoparticles was 2.58 nm (SD=0.74nm). For aggregates formed on the surface of *G.sulfurreducens* (Figure 6.8 a1 a2), the size was much smaller and more evenly distributed across the surface of the bacteria than in the mono Bio-Pt experiments. For Bio-Pd-Rh, the average size of nanoparticles was only 2.58 nm (SD=0.74nm). Compared to the TEM data for the Bio-Rh sample, the size of aggregates observed on the surface of G.*sulfurreducens* was around 20-35 nm, which was smaller than for the Bio-Rh samples. In addition, the small Bio-Pd-Rh nanoparticles were distributed evenly on the cell (Figure 6.8 b1). However, TEM images of bio-Pd(0) with Ru (hydro)oxides samples were different to those of Bio-PdPt and Bio-PdRh. Specifically, in addition to small Pd(0) nanoparticles (2.8 nm, SD=0.90 nm) attached to the surface of *G.sulfurreducens*, large particles also adhered to each other in the Pd-Ru sample, which was similar to the relationships observed in the TEM images of the mono Ru bioreduction products. Only a small fraction of the larger particles were observed to be attached to cell surfaces, and most were located outside the cell (Figure 6.8 c1).

Elemental mapping by the TEM of the Bio-Pd-Pt samples showed that Pd and Pt coexist in the nanoparticles (shown as yellow areas in Figure 6.8 a3), supporting the formation of Bio-Pd-Pt alloys (also indicated by both XPS and XRD as noted earlier). For the Bio-Pd-Pt sample, the Fourier transform (FT)

taken from the selected area on the cell surface showed the d-space of the particle formed was 0.225 nm, similar to the (111) crystal planes of Pd(0) and Pt(0) (Tuo et al., 2017). In addition, elemental mapping of Bio-Pd-Rh also indicates that most of the Bio-Pd-Rh nanoparticles had overlapping signals (yellow) rather than a single Pd or Pt signal (green or red), again indicative of an alloy (Figure 6.8 a3 and b3). However, elemental mapping results of Bio-Pd(0) with Ru (hydro)oxides samples showed the small nanoparticles contain only Pd, and FT results indicated the d-space of these particles is 0.227 nm. The latter is similar to the (111) crystal plane of Pd(0), suggesting that only Pd(0) nanoparticles were formed on the surface of *G.sulfurreducens* rather than mixed Bio-Pd-Ru alloy. For the large extracellular particles in the Pd-Ru sample, the elemental mapping results show both Pd and Ru, supporting the formation of extracellular Ru(III) (hydro)oxide and some Pd adsorbed on the top surface of Ru (hydro)oxides (marked by blue boxes in Figure 6.8 c5 & c6).

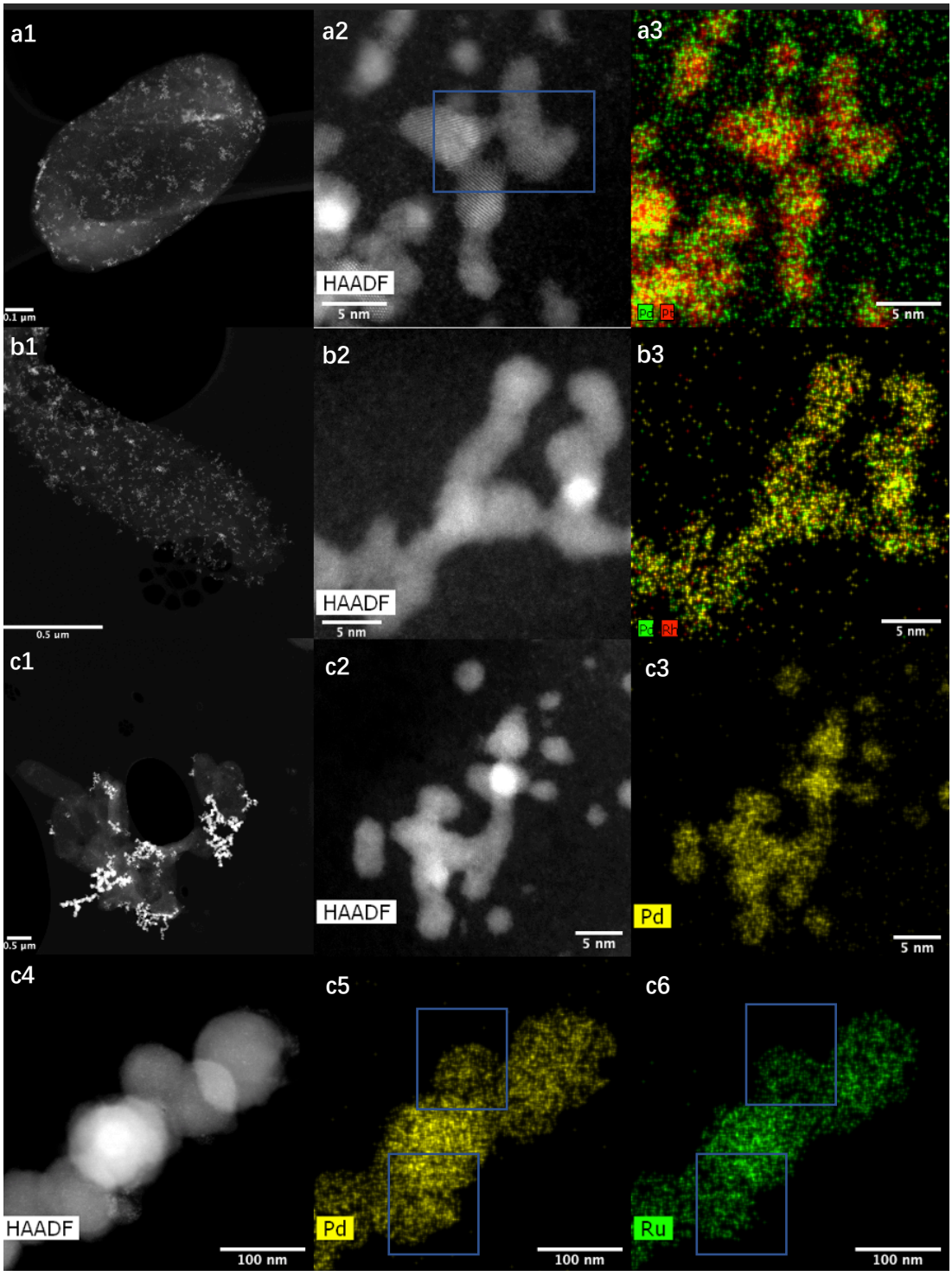

Figure 6.8 TEM images of *G.sulfurreducens* and PGM mixed nanoparticles. **a1, b1, c1**: TEM images of bio-PdPt, bio-PdRh and bio-Pd with Ru (hydro)oxides; **a2, b2, c2 & c4**: The HAADF images of the selected areas in bio-PdPt, bio-PdRh and bio-Pd with Ru (hydro)oxides; **a3, b3, c3, c5 and c6**: The EDS mapping of PGMs for bio-PdPt, bio-PdRh and bio-Pd with Ru (hydro)oxides

6.3.3 Bioreduction of low concentration Pd wire digestion solution

The *G.sulfurreducens* system was used in an experiment to test whether Pd could be recovered from an acid digestion solution of Pd wire at very low concentrations (Figure S6.2). The initial pH of the digestion solution was around 2. After adding it to bioreduction system, the pH can reach to around 7. The concentration of aqueous Pd decreased quickly in first hour from a starting point of 23 ppb to 7.3 ppb (OD_{600}=0.2) and 14.0 ppb (OD_{600}=0.1), while the concentration of Pd did not change in the no cell control sample. After 24 hours, 68% and 56% Pd had been removed from the experiments containing bacterial cells (0.2 and 0.1 OD, respectively); however, in the no cell samples only 35% Pd was removed from solution (Figure S6.2). These results indicate that *G.sulfurreducens* can also remove Pd ions from solution even at low concentrations and that a higher initial cell loading might lead to higher quantities of Pd removed. The characterization of the biological products still needs future analysis.

6.3.4 The application of biological PGM nanoparticles in the catalytic reduction of 4- nitrophenol

The reduction reaction of 4-NP to 4-aminophenol by $NaBH_4$, was chosen to test the catalytic abilities of the different biological PGM nanoparticles (Figure 6.9). According to thermodynamic calculations, this reduction process cannot be carried out without a catalyst (Ghosh et al., 2004). The pseudo-first-order

kinetics for catalytic reaction can be used to calculate the kinetic reaction rate.

$$\ln\left(\frac{C_t}{C_0}\right) = -K \times t$$

Where C_0 is the initial concentration of 4-NP and C_t is the concentration of 4-NP at t minutes. K is the kinetic rate constant which is used to evaluate the catalytic abilities.

Mono PGM nanoparticles formed by *G.sulfurreducens* could act as a catalyst for the reduction of 4-NP as shown by the removal of 4-NP (Figure 6.9A). After 10 minutes, the removal of 4-NP by mono Bio-Pd was 83% while the removal by the other PGM nanoparticles was between 20% to 35%, indicating that the Bio-Pd was the most effective catalyst. The k value of Bio-Pd was also 0.32 min^{-1}, which is 10-30 time better than all the other nanoparticles (Figure 6.9B). Previous results showed the morphology, particle size and composition can all affect the catalytic ability (Tuo et al., 2017; Zhang et al., 2014). According to the TEM images, although the single particle sizes of biological Pd(0), Pt(0) and Rh(0) were similar, the formation of aggregates on the bacterial surfaces in the Pd(0) samples are minimal, leading to the potential for a greater surface area over which to contact the 4-NP solution. The latter observation may be one of the reasons for the high catalytic activity of this material.

Bimetallic Bio-PGM samples containing 0.1 mM Pd with 0.1 mM Rh or Pt or Ru, exhibited improved catalytic abilities (K values) compared to the equivalent Bio-

monometallic nanoparticles (Figure 6.9). Pd is the exception to this general observation as the mono Bio-Pd catalyst performed best. In addition, the K value of Bio-Pd-Pt was 0.32 min^{-1}, which was similar to the best performing mono Bio-Pd catalyst.

The final removal value of 4-NP by Bio-Pd-Pt, Bio-Pd-Rh alloys and Pd(0)-Ru (hydro)oxides samples were greater than 95% in all cases, while for other mono PGM (except Bio-Pd), the final removal rates of 4-NP were only about 75%-90%. The reason for the improvement of the catalytic abilities of Bio-PdPt and Bio-PdRh could be that after incorporation of Pd in the initial solution, the Pd-Pt and Pd-Rh alloys formed, and alloys can improve the catalytic abilities (Hosseinkhani et al., 2012; Tuo et al., 2017; Zhang et al., 2014). Additionally, according to TEM images, the size of the Bio-Pd-Pt and Bio-Pd-Rh agglomerates were both smaller than both Bio-Pt and Bio-Rh agglomerates, and the distributions were more uniform on the surface of bacteria than those of the mono Bio-Pt and Bio-Rh. For Pd(0)-Ru samples, the k value was 0.068 min^{-1}, higher than that of pure Ru (hydro)oxides (0.019 min^{-1}), in turn likely due to the discrete formation of Pd(0) nanoparticles.

In addition, cells of *G. sulfurreducens* without added metal were also tested as a control for the catalyst experiment, but the results (not shown here) indicate that *G. sulfurreducens* cannot act as catalyst for the reduction of 4-NP,

confirming the primary role of PGM nanoparticles in the catalyst experiments, rather than the bacteria.

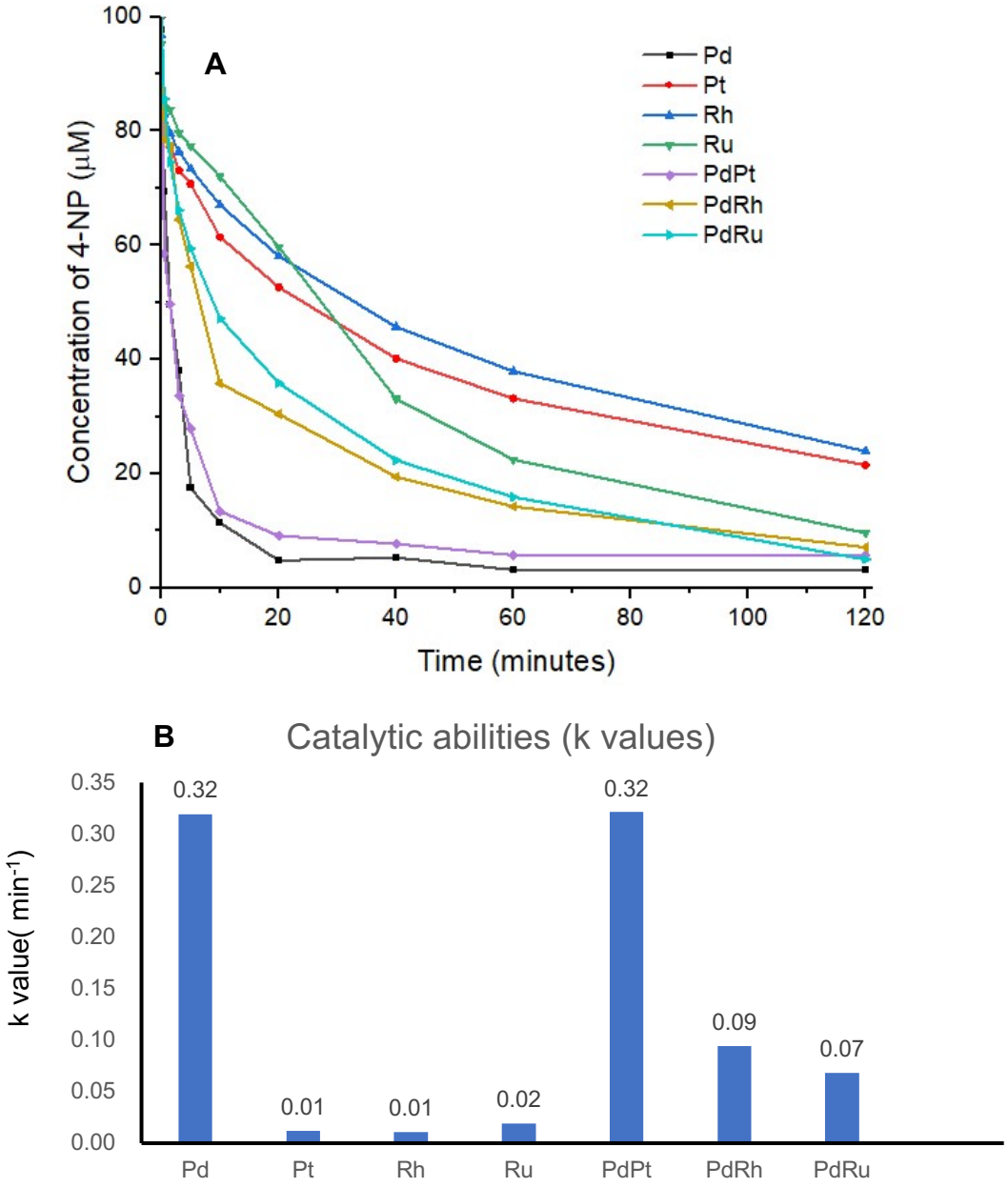

Figure 6.9. The removal of 4-NP during the reduction processes with different PGM nanoparticles as catalysts (A). The comparison of catalytic efficiency of each PGMs catalyst (B).

6.4 Conclusion

In this study, *G.sulfurreducens* produced Pd(0), Pt(0), Rh(0) nanoparticles and

biometallic Pd-Pt and Pd-Rh alloys. However, in contrast to Pd, Pt and Rh, Ru(III) cannot be reduced by this system, either on its own or in a mixed system with Pd. The results of the bioreduction of low concentration Pd wire digestion solution suggest that the *G.sulfurreducens* system may also have a relatively efficient recovery effect for a high acidity low concentration Pd solution. All of the Bio-PGM nanoparticles studied here may be used as catalysts; however, among the monometallic products, the catalytic ability of Bio-Pd gave the best results. For the biological products of Pd-X mixed samples, due to the smaller size, lower degree of agglomeration and more uniform distribution on the bacterial surface of the Pd-Pt and Pd-Rh alloys, the catalytic efficiency was improved compared with that of the corresponding monometallic products. The experiments reported here indicate that the bioreduction of the PGM could contribute to the generation of efficient biocatalysts and have potential applications in the field of resource recovery.

Acknowledgments

We would like to thank Dr. Ben Spencer for helping us carry out XPS test on the samples and this work was supported by the Henry Royce Institute, funded through EPSRC grants EP/R00661X/1, EP/P025021/1 and EP/P025498/1. The authors would also like to thank Dr. John Water and Dr. Abby Ragazzon-Smith for XRD and ICP-MS analyses. Funding from NERC is also acknowledged (award NE/P01304X/1).

Reference:

Baes Jr, C. & Mesmer, R. (1976). 'The hydrolysis of cations: Wiley interscience' *New York*.

Barkov, A. Y. & Zaccarini, F. (2019). Editorial for the special issue "platinum-group minerals: New results and advances in pge mineralogy in various ni-cu-cr-pge ore systems". Multidisciplinary Digital Publishing Institute.

Boily, J.-F., Seward, T. M. & Charnock, J. M. (2007). 'The hydrolysis and precipitation of pd (ii) in 0.6 mol kg− 1 nacl: A potentiometric, spectrophotometric, and exafs study' *Geochimica et Cosmochimica Acta*, 71 (20), pp. 4834-4845.

Butu, A., Rodino, S., Dobre, A. & Butu, M. (2016). 'Potential of microbial functional communities for high-tech critical metals recovery' *Studia Universitatis Vasile Goldis Seria Stiintele Vietii (Life Sciences Series)*, 26 (2).

Byrne, J., et al. (2013). 'Controlled cobalt doping in biogenic magnetite nanoparticles' *Journal of The Royal Society Interface*, 10 (83), p. 20130134.

Cinti, D., Angelone, M., Masi, U. & Cremisini, C. (2002). 'Platinum levels in natural and urban soils from rome and latium (italy): Significance for pollution by automobile catalytic converter' *Science of the Total Environment*, 293 (1-3), pp. 47-57.

Coker, V., et al. (2006). 'Xas and xmcd evidence for species-dependent partitioning of arsenic during microbial reduction of ferrihydrite to magnetite' *Environmental science & technology*, 40 (24), pp. 7745-7750.

Coppi, M. V., Leang, C., Sandler, S. J. & Lovley, D. R. (2001). 'Development of a genetic system for *geobacter sulfurreducens*' *Applied and environmental microbiology*, 67 (7), pp. 3180-3187.

Costa, O. Y., Raaijmakers, J. M. & Kuramae, E. E. (2018). 'Microbial extracellular polymeric substances: Ecological function and impact on soil aggregation' *Frontiers in microbiology*, 9 p. 1636.

Creamer, N. J., et al. (2006). 'Palladium and gold removal and recovery from precious metal solutions and electronic scrap leachates by *desulfovibrio desulfuricans*' *Biotechnology letters*, 28 (18), pp. 1475-1484.

Ek, K. H., Morrison, G. M. & Rauch, S. (2004). 'Environmental routes for platinum group elements to biological materials—a review' *Science of the Total Environment*, 334 pp. 21-38.

Ghosh, S. K., et al. (2004). 'Bimetallic pt–ni nanoparticles can catalyze reduction of aromatic nitro compounds by sodium borohydride in aqueous solution' *Applied Catalysis A: General*, 268 (1-2), pp. 61-66.

Hosseinkhani, B., et al. (2012). 'Microbially supported synthesis of catalytically active bimetallic pd-au nanoparticles' *Biotechnology and Bioengineering*, 109 (1), pp. 45-52.

Kim, H. & Popov, B. N. (2002). 'Characterization of hydrous ruthenium oxide/carbon nanocomposite supercapacitors prepared by a colloidal method' *Journal of Power Sources*, 104 (1), pp. 52-61.

Koek, M., et al. (2010). 'A review of the pgm industry, deposit models and exploration practices: Implications for australia's pgm potential' *Resources Policy*, 35 (1), pp. 20-35.

Li, C., et al. (2012). 'Enhanced ethanol electrooxidation of hollow pd nanospheres prepared by galvanic exchange reactions' *Materials Letters*, 69 pp. 92-95.

Liang, X. & Gadd, G. M. (2017). 'Metal and metalloid biorecovery using fungi' *Microbial biotechnology*, 10 (5), pp. 1199-1205.

Lloyd, J. R. (2003). 'Microbial reduction of metals and radionuclides' *FEMS microbiology reviews*, 27 (2-3), pp. 411-425.

Lloyd, J. R., Sole, V. A., Van Praagh, C. V. G. & Lovley, D. R. (2000). 'Direct and fe(ii)-mediated reduction of technetium by fe(iii)-reducing bacteria' *Applied and Environmental Microbiology*, 66 (9), pp. 3743-3749. DOI: 10.1128/AEM.66.9.3743-3749.2000.

Lloyd, J. R., Yong, P. & Macaskie, L. E. (1998). 'Enzymatic recovery of elemental palladium by using sulfate-reducing bacteria' *Applied and Environmental Microbiology*, 64 (11), pp. 4607-4609.

Lovley, D. R., Stolz, J. F., Nord, G. L. & Phillips, E. J. (1987). 'Anaerobic production of magnetite by a dissimilatory iron-reducing microorganism' *Nature*, 330 (6145), pp. 252-254.

Maksimainen, T., Luukkanen, S., Mörsky, P. & Kalapudas, R. (2010). 'The effect of grinding environment on flotation of sulphide poor pge ores' *Minerals Engineering*, 23 (11-13), pp. 908-914.

Melber, C., Keller, D. & Mangelsdorf, I. (2002). 'Palladium: Environmental health criteria' *World Health Organization, Geneva*, 222.

Mpinga, C., Eksteen, J., Aldrich, C. & Dyer, L. (2015). 'Direct leach approaches to platinum group metal (pgm) ores and concentrates: A review' *Minerals Engineering*, 78 pp. 93-113.

Mudd, G. M. (2012). 'Key trends in the resource sustainability of platinum group elements' *Ore Geology Reviews*, 46 pp. 106-117.

Mudd, G. M., Jowitt, S. M. & Werner, T. T. (2018). 'Global platinum group element resources, reserves and mining–a critical assessment' *Science of the Total Environment*, 622 pp. 614-625.

Murray, A., Zhu, J., Wood, J. & Macaskie, L. (2017). 'A novel biorefinery: Biorecovery of precious metals from spent automotive catalyst leachates into new catalysts effective in metal reduction and in the hydrogenation of 2-pentyne' *Minerals Engineering*, 113 pp. 102-108.

Naldrett, T., Kinnaird, J., Wilson, A. & Chunnett, G. (2008). 'Concentration of pge in the earth's crust with special reference to the bushveld complex' *Earth Science Frontiers*, 15 (5), pp. 264-297.

Nancharaiah, Y., Mohan, S. V. & Lens, P. (2016). 'Biological and bioelectrochemical recovery of critical and scarce metals' *Trends in biotechnology*, 34 (2), pp. 137-155.

Ngwenya, N. & Whiteley, C. G. (2006). 'Recovery of rhodium (iii) from solutions and industrial wastewaters by a sulfate-reducing bacteria consortium' *Biotechnology progress*, 22 (6), pp. 1604-1611.

O'Driscoll, B. & González-Jiménez, J. M. (2016). 'Petrogenesis of the platinum-group minerals' *Reviews in Mineralogy and Geochemistry*, 81 (1), pp. 489-578.

Povar, I. & Spinu, O. (2016). 'Ruthenium redox equilibria 1. Thermodynamic stability of ru (iii) and ru (iv) hydroxides' *Journal of Electrochemical Science and Engineering*, 6 (1), pp. 123-133.

Qu, L. & Dai, L. (2005). 'Substrate-enhanced electroless deposition of metal nanoparticles on carbon nanotubes' *Journal of the American Chemical Society*, 127 (31), pp. 10806-10807.

Ravindra, K., Bencs, L. & Van Grieken, R. (2004). 'Platinum group elements in the environment and their health risk' *Science of the total environment*, 318 (1-3), pp. 1-43.

Sahu, P., Jena, M., Mandre, N. R. & Venugopal, R. (2021). 'Platinum group elements mineralogy, beneficiation, and extraction practices–an overview' *Mineral Processing and Extractive Metallurgy Review*, 42 (8), pp. 521-534.

Stöckl, M., et al. (2019). 'Extracellular polymeric substances from *geobacter sulfurreducens* biofilms in microbial fuel cells' *ACS applied materials & interfaces*, 11 (9), pp. 8961-8968.

Tamaoki, K., Saito, N., Nomura, T. & Konishi, Y. (2013). 'Microbial recovery of rhodium from dilute solutions by the metal ion–reducing bacterium *shewanella algae*' *Hydrometallurgy*, 139 pp. 26-29.

Troitskii, S. Y., Fedotov, M. & Likholobov, V. (1993). 'Studies of the compositions of pd (ii) hydrolysis products' *Russian chemical bulletin*, 42 (4), pp. 634-639.

Tuo, Y., et al. (2017). 'Microbial synthesis of bimetallic pdpt nanoparticles for catalytic reduction of 4-nitrophenol' *Environmental Science and Pollution Research*, 24 (6), pp. 5249-5258.

Tuo, Y., et al. (2015). 'Microbial synthesis of pd/fe3o4, au/fe3o4 and pdau/fe3o4 nanocomposites for catalytic reduction of nitroaromatic compounds' *Scientific reports*, 5 (1), pp. 1-12.

Tuo, Y., et al. (2013). 'Microbial formation of palladium nanoparticles by *geobacter sulfurreducens* for chromate reduction' *Bioresource technology*, 133 pp. 606-611.

Wyatt, I. R. (1966). 'Hydrolyse van palladium (ii) chloride' *Chemish Weekblad*, 62 pp. 310-314.

Xu, H., et al. (2018). ‘Microbial synthesis of pd–pt alloy nanoparticles using *shewanella oneidensis* mr-1 with enhanced catalytic activity for nitrophenol and azo dyes reduction’ *Nanotechnology*, 30 (6), p. 065607.

Yates, M. D., Cusick, R. D. & Logan, B. E. (2013). ‘Extracellular palladium nanoparticle production using *geobacter sulfurreducens*’ *ACS Sustainable Chemistry & Engineering*, 1 (9), pp. 1165-1171.

Yong, P., et al. (2002). ‘Bioreduction and biocrystallization of palladium by *desulfovibrio desulfuricans* ncimb 8307’ *Biotechnology and bioengineering*, 80 (4), pp. 369-379.

Zhang, P., Li, R., Huang, Y. & Chen, Q. (2014). ‘A novel approach for the in situ synthesis of pt–pd nanoalloys supported on fe3o4 c core–shell nanoparticles with enhanced catalytic activity for reduction reactions’ *ACS applied materials & interfaces*, 6 (4), pp. 2671-2678.

Zheng, J. & Jow, T. (1995). ‘A new charge storage mechanism for electrochemical capacitors’ *Journal of the Electrochemical Society*, 142 (1), p. L6.

Zhuang, W.-Q., et al. (2015). ‘Recovery of critical metals using biometallurgy’ *Current opinion in biotechnology*, 33 pp. 327-335.

Appendix S6

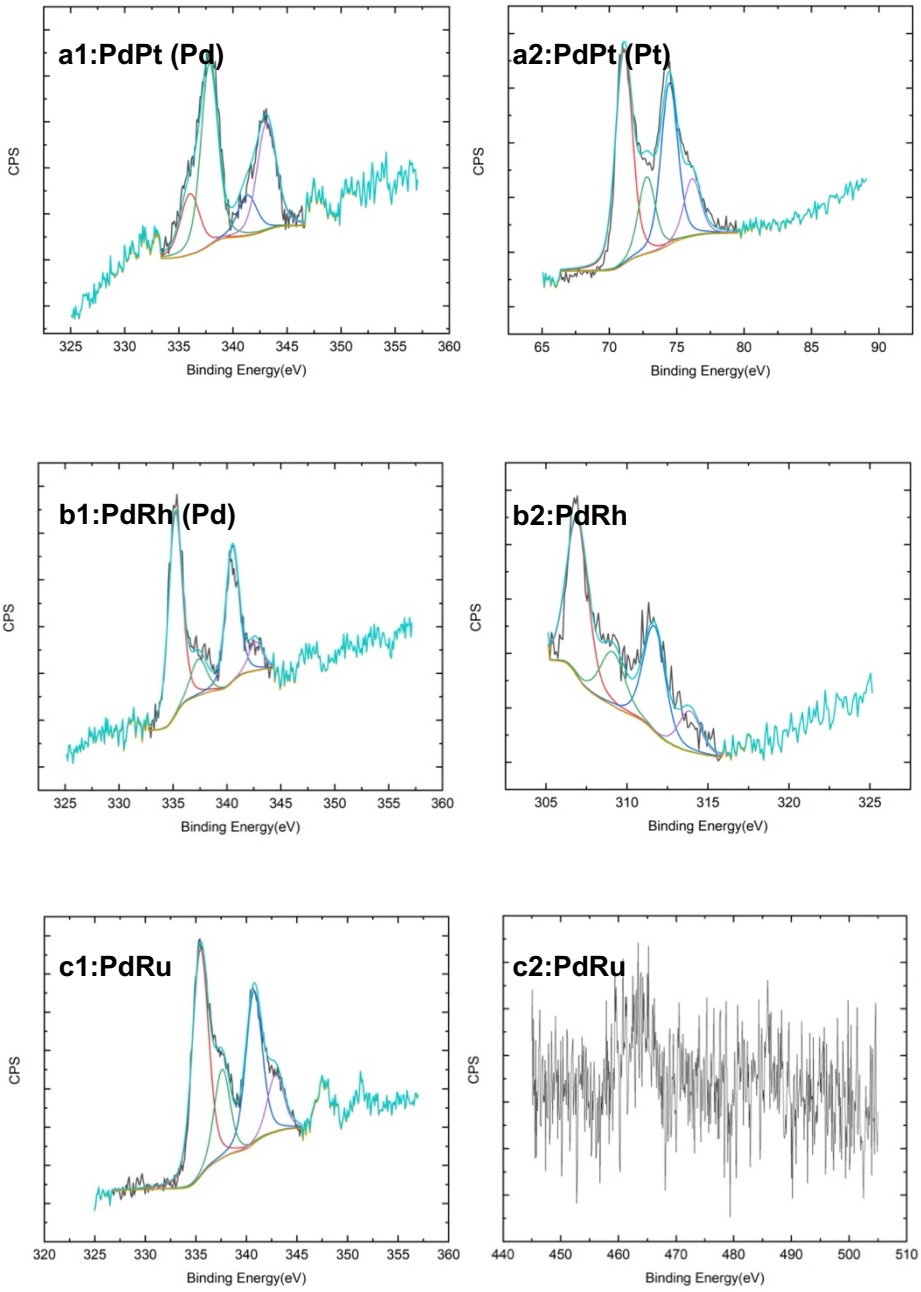

Figure S6.1 XPS spectra (black) and the fitting curves (blue) of the post reduction products; **a1:** Pd spectra of PdPt sample. **a2:.** Pt spectra of PdPt sample; **b1**: Pd spectra of PdRh sample; **b2**: Rh spectra of PdRh sample; **c1**: Pd spectra of PdRu sample; **c2**: Ru spectra of PdRu sample;

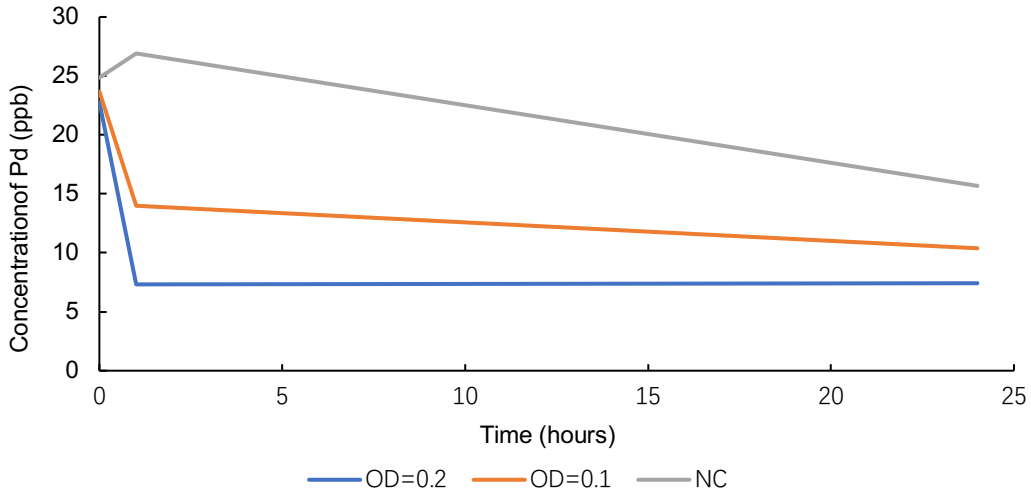

Figure S6.2 The concentration changes of Pd in the bioreduction processes. OD means OD_{600} which states for the concentration of bacterial. NC means no cell control treatments.

Chapter 7: Conclusion and future work

7.1 Conclusion

Environmental pollution of metal and metalloid elements and the shortage of critical materials are becoming hot topics of concern in the world. There is a connection between these two challenges, as some hazardous elements have also been identified as critical materials. As a result, the immobility and recovery of critical and/or environmentally hazardous elements can solve both problems. Bioremediation and biorecovery methods have also been considered as cost-saving and environmental friendly, compared with physical and chemical treatment methods (Kuppusamy et al., 2016; Lloyd et al., 2019; Rajput et al., 2021) emphasising the importance of this emerging research area.

In **Chapter 2**, the current annual output, main producing areas, supply situation and possible environmental pollution of rare earth elements, antimony, gold and PGMs were reviewed to cover the current pollution level and resource utilization of these critical metals and metalloids. The reviews of these critical materials indicate that the mineral distribution of elements are uneven and very dependent on supply from a few sources. For gold and PGMs, in addition to the characteristics of uneven distribution and dependence, there is also a supply risk due to the increase in demand. Moreover, the exploitation of these critical metals and metalloids can directly or indirectly cause environmental pollution problems which thus affect human health. Antimony has been considered as

an environmental contaminant in some countries and exposure to high Sb concentration can cause damage to organs (Li et al., 2016). PGMs can also accumulate in the human body through the food chain (Ek et al., 2004; Melber et al., 2002). In contrast, although some elements such as rare earth elements and gold, are not considered hazardous elements and do not directly harm the environment, the mining processes associated with their extraction can cause environment damage, leading to water acidification and also the release of heavy metals and radioactive of nuclear elements, and heavy metal enrichment (Abdul-Wahab and Marikar, 2012; Liu, 2016).

In **Chapter 4**, a research chapter focuses on the tight coupling between the redox cycling of Fe, and the fate of the rare earth element Ce, also exploring a role of biologically synthesised magnetite/Ce as a fuel cell catalyst. In this work, Ce-bearing ferrihydrite was reduced by *G. sulfurreducens* using acetate as electron donor. The addition of different amounts of cerium had contrasting effects on biological processes. Ce at the lowest concentration (0.5% mol%) had a negligible impact on the bioreduction of ferrihydrite to biomagnetite. However, through comparisons to stoichiometric magnetite, XMCD results indicated that Ce was potentially incorporated into the Fe(III) sites of the magnetite, because the Fe(II)/Fe(III) ratios of Ce bearing magnetite were all below to that of biomagnetite. When the initial content of Ce in ferrihydrite was increased to 2%, bioreduction was blocked, and the dominant Fe mineral

endpoint detected was goethite. However, although the end products changed with increases in Ce content, Ce ions were not released from the Fe minerals, suggesting the close binding of cerium with Fe minerals under natural conditions. Previous research indicated that in addition to Pt, cerium materials and magnetite could be used as catalysts for fuel cell electrodes (Liu et al., 2018; Takahashi et al., 2007). Pure biomagnetite and 0.5% Ce-bearing bioirmagnetite were added to carbon black supported Pt catalysts to evaluate their catalytic abilities. The results showed that by adding 0.5% Ce-bearing magnetite, it was possible to not only reduce Pt dosage by approximately 17%, but also prolong the durability of the catalysts.

In **Chapter 5**, the adsorption of a range of concentrations of Sb(V) by ferrihydrite again emphasised the strong link between Fe and trace elements, indicating that Fe(III) minerals can immobilise Sb in subsurface anaerobic environments. In order to research the influence of Sb(V) on the bioreduction process of ferrihydrite by dissimilatory metal reducing bacteria, the Sb(V)-adsorbed ferrihydrite was exposed to *G. sulfurreducens* in the presence of acetate as the electron donor. The bioreduction results indicated that Sb in ferrihydrite inhibited the bioreduction of Fe(III) minerals, because with increasing amounts of adsorbed Sb(V), the main types of Fe biominerals formed changed from magnetite to goethite. In addition, siderite was present with goethite at intermediate (2% mol%) Sb samples after 7days of bioreduction.

This suggests that antimony in the product obstructs the binding of microbial generated Fe(II) to the intermediate (goethite), resulting in the combination of Fe(II) and bicarbonate in the buffer, which reacted to give siderite. Magnetite was only formed in the 0.5% and 1% Sb adsorbed ferrihydrite, and the size of magnetite particles formed was inversely proportional to the content of antimony.

The fate of Sb during the bioreduction processes was also studied in this project. Bioreduction experiments showed that *G. sulfurreducens* cannot reduce soluble Sb(V) ions directly under anaerobic conditions. Additionally, during the bioreduction of Sb-adsorbed ferrihydrite, XPS shown that no Sb(V) was reduced to Sb(III). This finding indicated that Sb(V) in Fe oxides cannot be reduced by either *G. sulfurreducens* or biogenic Fe(II). According to ICP-MS data from long-term monitoring, no Sb was mobilized during the bioreduction of ferrihydrite, highlighting a potentially key role for Fe minerals in the treatment of antimony pollution.

Chapter 6 explored the bioreduction and biorecovery of critical metals in the absence of Fe(III), focusing the platinum group metals. An effective and fast bioreduction/biorecovery method was developed using *G. sulfurreducens* for Pd, Pt and Rh. Monometallic Pd(0), Pt(0) and Rh(0) nanoparticles were formed, and associated with the bacterial cell during the bioreduction process. After 24

hours, the precipitation efficiencies of Pd, Pt and Rh all reached more than 90%. However, for monometallic Bio-Pt(0) and Bio-Rh(0) nanoparticles, small nanoparticles (3.28nm for Bio-Pt and 2.73nm for Bio-Rh) combined together to form larger agglomerates (tens to hundreds of nanometers) on *G. sulfurreducens*. In contrast to Pd(II), Pt(IV) and Rh(III), *G. sulfurreducens* was not able to reduce Ru(III) with acetate as the electron donor. Instead, Ru (hydro)oxides formed at the neutral pH in this system, and adsorbed to the surface of *t*he cells. TEM, XPS and XRD analyses of products from the PGM mix (Pd-X) experiments by *G. sulfurreducens* highlighted formation of PdPt and PdRh alloys. Compared to monometallic PGM nanoparticles (Pd(0), Pt(0) and Rh(0)), the resulting alloy particles had smaller diameters, and were more uniform in distribution on the bacterial surface (with less agglomeration).

Experiments were also conducted at environmentally-relevant concentrations of Pd(II), and *G. sulfurreducens* was still able to show good removal and recovery of the PGM at very low concentrations (23ppb). Finally, the catalytic performances of the PGM nanoparticles formed at the higher metal loadings were assayed by the reduction of 4-NP by $NaBH_4$. The catalytic abilities of the monometallic Pd(0) and PdPt alloys were 3-30 times better than the other PGMs nanoparticles for the assay used. These findings showed that *G. sulfurreducens* has the capacity to bioreduce PGMs and produce PGMs nanoparticles at a range of concentrations, presented in mixed and single

metal solutions, supporting the view that microbial reduction of PGMs can plan an important role in the biorecovery of PGMs from wastes or contaminated areas.

7.2 Future research

This research investigated the abilities of *G. sulfurreducens* for the bioreduction and biorecovery of critical elements such as REE, Sb and PGMs which can help us understand the interactions between metal-reducing bacteria and various metal and metalloids in anaerobic subsurface environments, and engineered bioreactors. This research also explored catalytic applications of the bioreduction products. These studies open up the way for future research areas including:

i) Characterize the fate of Sb and Ce during bioreduction

Characterization of the fate of Sb and Ce can provide us information on the circulation, valence change and structural form of both antimony and cerium during microbial reduction of Fe(III)-rich systems to help us further understand their biogeochemical behaviors. In this research, XPS and TEM was used to detect the chemical valance and locations of Ce and Sb in Fe minerals. Since the binding energy of Ce is quite similar to Fe and the content of Ce is much smaller than Fe, XPS cannot be used to detect Ce. In addition, because of the detection limits of XPS, only surface analysis was conducted. XAS could prove

better to investigate the fate of Ce and Sb. However, XAS could not be used in this work, due to the COVID lockdown. This approach could be used in future studies to detect the fate of both Sb and Ce to obtain valence state and structure information in both internal and surface layers.

ii) Optimize existing catalytic experiments and research more suitable catalytic applications of bioreduction products; Scale up the existing experiments

In this research, some bioreduction products have been applied to catalytic experiments, such as 0.5% Ce bearing magnetite and PGMs nanoparticles. On the one hand, the existing catalytic experiments can be further optimized. Although the experimental results showed that the incorporation of 0.5% Ce bearing magnetite can reduce the amount of Pt by 17% in Pt/CB catalyst and improve the duration of the catalyst, the incorporation amount can be changed in the following experiments to determine whether a more economic and longer service life of the Pt/CB catalyst can be obtained. On the other hand, for PGM nanoparticles, in addition to the existing catalytic reduction of 4-NP reaction, we can try more catalytic experiments to test whether the PGM bionanoparticles can also be effective catalysts for other reactions. For example, some research shows that Pt, Pd and Rh can all be used as catalysts for the oxidation of hydrocarbons and CO in the waste gases (Balcerzak, 1997; Nzaba et al., 2019). The previous research showed that Rh is considered as the best elements to

reduce nitrogen oxides to nitrogen (Acres and Harrison, 2004; Twigg, 1999). In addition, PGMs also proved good catalysts for the water contamination treatment (Tuo et al., 2017; Tuo et al., 2013). Bimetallic PdPt alloy was also reported as a high performance catalyst for the reduction of azo dyes (Xu et al., 2018). Some PGM catalysts, such as Pd-based catalysis and mixed PGMs catalyst can also be used in the reduction of some oxyanions (Chaplin et al., 2012; Chen et al., 2017). The monometallic PGMs, bimetallic PdRh and PdPt alloy nanoparticles synthesized during this study could be used for a wide range of applications, which requires further investigation..

The experiments described in this thesis are very small-scale, so scaling up these processes for future industrial applications also warrants further attention.

iii) Expand the application field of bioreduction and biorecovery by *G. sulfurreducens* and study the application of other microorganism in biological recovery and bioremediation

The bioreduction and biorecovery of Ce or Sb bearing ferrihydrite and PGMs by *G. sulfurreducens* were investigated in this study. However, there are many other critical elements could be involved in the future research. For example, similar to PGMs, gold is also a high value metal with high performance of catalytic abilities in many areas (Sathishkumar et al., 2010). In addition, Au is often contained in E-wastes, so the biorecovery of Au from e-wastes could also

help us build global circular economy. Ce belongs to rare earth elements and used widely as catalysts. There are still some other rare earth elements which could also be research in the future such as lanthanum and praseodymium. The crustal abundance of REEs are not low but the distributions are not evenly worldwide and REE play important positions in the field of catalysts (Haque et al., 2014). So similar to this research of Bio-Ce-magnetite, the investigation of biorecovery of other REEs to form new biological catalysts could be practical application potential. In addition, the critical elements contained in real wastes (such as e-wastes and mining wastes) can also be the object of our future study, so as to maximise the recovery of these critical elements and reduce environmental pollution.

In addition to *G. sulfurreducens,* other metal-reducing bacteria can also be introduced into our study in the future such as *Shewanella* species. *Shewanella* species have been reported to reduce a range of metals under lab conditions and in the natural environment, such as Cu(II), Fe(III), U(VI), Se(VI)/(IV), Pd(II), Au(III) and Ag(I) (Kimber et al., 2018; Lloyd et al., 2011; Marshall et al., 2006; Pearce et al., 2009; Suresh et al., 2011). Therefore, in our future study, we could introduce new metal-reducing bacteria into our experiments and compare them with existing experimental data so as to select bacteria with higher recovery or reduction rates for different metal ions.

Reference:

Abdul-Wahab, S. & Marikar, F. (2012). 'The environmental impact of gold mines: Pollution by heavy metals' *Open engineering*, 2 (2), pp. 304-313.

Acres, G. & Harrison, B. (2004). 'The development of catalysts for emission control from motor vehicles: Early research at johnson matthey' *Topics in Catalysis*, 28 (1), pp. 3-11.

Balcerzak, M. (1997). 'Analytical methods for the determination of platinum in biological and environmental materialsa review' *Analyst*, 122 (5), pp. 67R-74R.

Chaplin, B. P., et al. (2012). 'Critical review of pd-based catalytic treatment of priority contaminants in water' *Environmental science & technology*, 46 (7), pp. 3655-3670.

Chen, X., et al. (2017). 'Exploring beyond palladium: Catalytic reduction of aqueous oxyanion pollutants with alternative platinum group metals and new mechanistic implications' *Chemical Engineering Journal*, 313 pp. 745-752.

Ek, K. H., Morrison, G. M. & Rauch, S. (2004). 'Environmental routes for platinum group elements to biological materials—a review' *Science of the Total Environment*, 334 pp. 21-38.

Haque, N., Hughes, A., Lim, S. & Vernon, C. (2014). 'Rare earth elements: Overview of mining, mineralogy, uses, sustainability and environmental impact' *Resources*, 3 (4), pp. 614-635.

Kimber, R. L., et al. (2018). 'Biosynthesis and characterization of copper nanoparticles using *shewanella oneidensis*: Application for click chemistry' *Small*, 14 (10), p. 1703145.

Kuppusamy, S., et al. (2016). 'In-situ remediation approaches for the management of contaminated sites: A comprehensive overview' *Reviews of Environmental Contamination and Toxicology Volume 236*, pp. 1-115.

Li, J., et al. (2016). 'Microbial antimony biogeochemistry: Enzymes, regulation, and related metabolic pathways' *Applied and environmental microbiology*, 82 (18), pp. 5482-5495. DOI: 10.1128/AEM.01375-16.

Liu, H. (2016). 'Rare earths: Shades of grey: Can china continue to fuel our global clean & smart future' *China Water Risk*.

Liu, P., et al. (2018). 'Stimulated electron transfer inside electroactive biofilm by magnetite for increased performance microbial fuel cell' *Applied energy*, 216 pp. 382-388.

Lloyd, J., et al. (2019). 'New frontiers in metallic bio-nanoparticle catalysis and green products from remediation processes', *Resource recovery from wastes*, pp. 244-265.

Lloyd, J. R., Byrne, J. M. & Coker, V. S. (2011). 'Biotechnological synthesis of functional nanomaterials' *Current opinion in biotechnology*, 22 (4), pp. 509-515.

Marshall, M. J., et al. (2006). ‘C-type cytochrome-dependent formation of u (iv) nanoparticles by *shewanella oneidensis*’ *PLoS biology*, 4 (8), p. e268.

Melber, C., Keller, D. & Mangelsdorf, I. (2002). ‘Palladium: Environmental health criteria’ *World Health Organization, Geneva*, 222.

Nzaba, S. M., Mamba, B. B. & Kuvarega, A. T. (2019). ‘Platinum group metal based nanocatalysts for environmental decontamination’ *Nanocatalysts*.

Pearce, C. I., et al. (2009). ‘Investigating different mechanisms for biogenic selenite transformations: *Geobacter sulfurreducens*, *shewanella oneidensis* and *veillonella atypica*’ *Environmental technology*, 30 (12), pp. 1313-1326.

Rajput, V. D., et al. (2021). ‘Insights into the biosynthesis of nanoparticles by the genus *shewanella*’ *Applied and Environmental Microbiology*, 87 (22), pp. e01390-21.

Sathishkumar, M., et al. (2010). ‘Green recovery of gold through biosorption, biocrystallization, and pyro-crystallization’ *Industrial & Engineering Chemistry Research*, 49 (16), pp. 7129-7135.

Suresh, A. K., et al. (2011). ‘Biofabrication of discrete spherical gold nanoparticles using the metal-reducing bacterium *shewanella oneidensis*’ *Acta Biomaterialia*, 7 (5), pp. 2148-2152.

Takahashi, M., et al. (2007). ‘Design of high-quality pt–ceo2 composite anodes supported by carbon black for direct methanol fuel cell application’ *Journal of the American Ceramic Society*, 90 (4), pp. 1291-1294.

Tuo, Y., et al. (2017). ‘Microbial synthesis of bimetallic pdpt nanoparticles for catalytic reduction of 4-nitrophenol’ *Environmental Science and Pollution Research*, 24 (6), pp. 5249-5258.

Tuo, Y., et al. (2013). ‘Microbial formation of palladium nanoparticles by *geobacter sulfurreducens* for chromate reduction’ *Bioresource technology*, 133 pp. 606-611.

Twigg, M. V. (1999). ‘Twenty-five years of autocatalysts’ *Platinum Metals Review*, 43 (4), pp. 168-171.

Xu, H., et al. (2018). ‘Microbial synthesis of pd–pt alloy nanoparticles using *shewanella oneidensis* mr-1 with enhanced catalytic activity for nitrophenol and azo dyes reduction’ *Nanotechnology*, 30 (6), p. 065607.